Air Force Institute of Technology
AFIT Scholar

Theses and Dissertations | Student Graduate Works

9-2005

A Prediction Code for the Thrust Performance of Two-Dimensional, Non-Axisynnetric, Converging Diverging Nozzles

Angela M. Geatz

Follow this and additional works at: https://scholar.afit.edu/etd

 Part of the Propulsion and Power Commons

Recommended Citation

Geatz, Angela M., "A Prediction Code for the Thrust Performance of Two-Dimensional, Non-Axisynnetric, Converging Diverging Nozzles" (2005). *Theses and Dissertations*. 3537.
https://scholar.afit.edu/etd/3537

This Thesis is brought to you for free and open access by the Student Graduate Works at AFIT Scholar. It has been accepted for inclusion in Theses and Dissertations by an authorized administrator of AFIT Scholar. For more information, please contact richard.mansfield@afit.edu.

A PREDICTION CODE FOR THE THRUST PERFORMANCE OF TWO-DIMENSIONAL, NON-AXISYNNETRIC, CONVERGING DIVERGING NOZZLES

THESIS

Angela M. Geatz

AFIT/GAE/ENY/06-03

DEPARTMENT OF THE AIR FORCE
AIR UNIVERSITY

AIR FORCE INSTITUTE OF TECHNOLOGY

Wright-Patterson Air Force Base, Ohio

APPROVED FOR PUBLIC RELEASE; DISTRIBUTION UNLIMITED

The views expressed in this thesis are those of the author and do not reflect the official policy or position of the United States Air Force, Department of Defense, or the United States Government.

AFIT/GAE/ENY/06-03

A PREDICTION CODE FOR THE THRUST PERFORMANCE OF TWO DIMENSIONAL, NON-AXISYMMETRIC, CONVERGING-DIVERGING NOZZLES

THESIS

Presented to the Faculty

Department of Aeronautics and Astronautics

Graduate School of Engineering and Management

Air Force Institute of Technology

Air University

Air Education and Training Command

In Partial Fulfillment of the Requirements for the

Degree of Master of Science in Aeronautical Engineering

Angela M. Geatz, BS

September 2005

APPROVED FOR PUBLIC RELEASE; DISTRIBUTION UNLIMITED.

AFIT/GAE/ENY/06-03

A PREDICTION CODE FOR THE THRUST PERFORMANCE OF TWO DIMENSIONAL, NON-AXISYMMETRIC, CONVERGING-DIVERGING NOZZLES

Angela M. Geatz, BS

Approved:

_____/signed/_____	_____
Paul King (Chairman)	date
_____/signed/_____	_____
Milton Franke (Member)	date
_____/signed/_____	_____
Richard McMullan (Member)	date

Abstract

The objective of this research is to develop a prediction code for the Air Force Research Laboratory Propulsion Directorate that can accurately determine the gross thrust coefficient for a user defined non-axisymmetric two-dimensional converging diverging nozzle. The code includes the effects of friction, angularity, and expansion losses on nozzle efficiency. To demonstrate the prediction method, the generated computational results were compared to experimental data, as well as computational results from other existing nozzle performance codes, for a number of different nozzle geometries. The nozzle internal performance prediction code showed excellent agreement with experimental data in predicting the gross thrust performance for all nozzle geometries considered. It was shown, however, that when the experimental data showed evidence of flow separation, a flow phenomenon this code is unable to predict, the code results underpredicted the experimental by up to 10%.

For My Family
Thanks for all your Encouragement and Support

Acknowledgments

I would like to express my sincere gratitude to my faculty advisor, Dr. Paul King, for his guidance and support throughout the course of this thesis effort. The insight and experience was, without doubt, appreciated. I would also like to convey my thankfulness to my sponsor, Alex Giese, from the Air Force Research Laboratory Propulsion Directorate for the support provided to me in this endeavor.

Angela M. Geatz

Table of Contents

List of Figures

Appendix C Figure Page

List of Tables

List of Symbols

Symbol	
2D	Two-Dimensional
CD	Converging Diverging
NPR	Nozzle Pressure Ratio
a	Speed of sound
A	Area
A^*	Area at nozzle throat
C_A	Angularity coefficient
C_d	Discharge coefficient
C_f	Skin friction coefficient
C_{fg}	Gross thrust coefficient
C_p	Specific heat at constant pressure
C_V	Velocity coefficient
d, D	Diameter
$\frac{dp}{dx}$	Pressure gradient
F_g	Gross thrust
g_c	Coefficient of gravity
H	Shape parameter
h	Height
L	Length
M	Mach number
$\dot{m}$	Mass flow rate
$\dot{m}_{ideal}$	Ideal mass flow rate
P	Pressure
P	Perimeter
Pr	Prandtl number

Q	Volume flow rate
R	Specific gas constant
R_c	Radius of curvature
Re	Reynolds number
$\overline{\mathrm{Re}_D^*}$	Modified Reynolds number
r	Radius
T	Temperature
V	Velocity
α	Local flow angle
α	Secondary nozzle half angle
β	Pressure gradient parameter
γ	Specific heat ratio
δ	Boundary layer thickness
δ^*	Displacement thickness
ε	Secondary nozzle half angle
θ	Momentum thickness
θ	Primary nozzle half angle
λ	Thwaites parameter
λ	Darcy friction factor
μ	Dynamic viscosity
μ	Mach angle
ρ	Density
τ	Shear stress
ν	Kinematic viscosity
Ω	Radius ratio

Subscripts

0	Stagnation
7	Nozzle entrance station
8	Nozzle throat station
9	Nozzle exit station
e, eff	Effective
h	Hydraulic
i	Ideal
inv	Inviscid
s	isentropic
t	Throat
vis	Viscous
w	wall

Superscripts

*	Conditions at throat assuming one dimensional flow

A PREDICTION CODE FOR THE THRUST PERFORMANCE OF TWO-DIMENSIONAL, NON-AXISYMMETRIC, CONVERGING-DIVERGING NOZZLES

1. Introduction

The exhaust nozzle is a very important component of the overall engine propulsion system. The amount of thrust delivered by the engine is more sensitive to nozzle performance than to the performance of any other engine component. For this reason, it is highly important to be able to predict the gross thrust efficiency for a given nozzle geometry.

The efficiency of an engine nozzle, usually represented by the nozzle gross thrust coefficient (C_{fg}), is defined as the ratio of the actual nozzle gross thrust to the ideal available gross thrust. Knowledge of the gross thrust coefficient provides a manner in which one can calculate the actual gross thrust produced by an engine at operating conditions of interest. Losses occurring in the nozzle reduce the amount of actual nozzle gross thrust available, thus causing a reduction in nozzle efficiency. Some causes of nozzle performance losses are

(1) Friction – Momentum loss due to wall friction in the nozzle,

(2) Angularity – Momentum loss due to nonaxial flow at the exit plane of the nozzle,

(3) Expansion – Loss due to the mismatch of the nozzle exit pressure with the ambient pressure,

(4) Leakage – losses caused by gas leakage out of the nozzle (inherent with variable area nozzles), and

(5) Cooling air throttling loss[1] – loss that occurs when the cooling flow is removed from the tailpipe liner, experiences a pressure drop due to the difference in pressure between the liner flow and the nozzle cavity pressure (the liner flow pressure level is considerably higher than the nozzle cavity pressure), and is put back into the nozzle at a lower total pressure and thus lower available thrust.

The objective of this research is to develop a prediction code for the Air Force Research Laboratory Propulsion Directorate that can accurately determine the gross thrust coefficient for a user defined non-axisymmetric two-dimensional converging diverging nozzle. The Propulsion Directorate is concerned primarily with the results for aircraft exhaust nozzles, so it is very important that the program can provide valid predictions for low to mid-range nozzle pressure ratios.

For this study, only losses due to friction, angularity, and expansion are considered. A comparison of the program results with published experimental data as well as computational results from other existing nozzle performance codes is presented for several cases and gives insight into the nozzle performance characteristics discussed herein.

[1] Some converging diverging nozzles feature a cooling slot at the nozzle throat in order to supply extra film cooling air for the secondary nozzle during reheat. The cooling air is normally extracted from the tailpipe liner cooling flow (located upstream of, or at, the the primary nozzle hinge).

1.1 Chapter Summaries

Chapter 2 of this document provides brief background descriptions of the one dimensional mass flow relations as well as the nozzle coefficients of efficiency including the gross thrust coefficient, discharge coefficient, velocity coefficient, and angularity coefficient.

Chapter 3 defines the methodology of the nozzle performance prediction code. This chapter includes a section devoted to nozzle geometry definition, the ideal mass model, determination of the inviscid and viscous discharge coefficients, determination of the velocity coefficient, determination of the angularity coefficient, and determination of the nozzle gross thrust coefficient.

Chapter 4 provides a comparison of the program results with published experimental data as well as computational results from other existing nozzle performance codes for several nozzle geometries.

Chapter 5 lists important conclusions and recommendations for future work.

2. Background

One dimensional isentropic flow relations are considered as a starting point for the analysis of the internal flow within a given nozzle. Many actual processes, such as flows in nozzles and diffusers, are ideally isentropic making the study of the isentropic flow of a perfect gas in the absence of work and body forces worthwhile. The results obtained through the assumption of constant specific heat are useful even for large temperature changes as long as one uses appropriate average values of C_p and γ.

2.1 One-Dimensional Compressible Mass Flow Relations [1]

For constant specific heat, the stagnation state energy equation can be written as

$$\frac{T_0}{T} = 1 + \frac{V^2}{2C_pT} \tag{2.1}$$

or, with the definition of Mach number, as

$$\frac{T_0}{T} = 1 + \frac{\gamma - 1}{2} M^2 \tag{2.2}$$

since $C_p = \frac{\gamma R}{\gamma - 1}$. For a perfect gas with constant specific heats, the stagnation temperature can be related to the stagnation pressure through the relation

$$\frac{P_0}{P} = \left(\frac{T_0}{T} \right)^{\frac{\gamma}{\gamma - 1}}. \tag{2.3}$$

The substitution of Equation (2.2) into Equation (2.3), gives

$$\frac{P_0}{P} = \left(1 + \frac{\gamma - 1}{2} M^2 \right)^{\frac{\gamma}{\gamma - 1}}. \tag{2.4}$$

From the perfect gas law and Equations (2.2) and (2.4),

$$\frac{\rho_0}{\rho} = \left(1 + \frac{\gamma - 1}{2} M^2\right)^{\frac{1}{\gamma - 1}}. \tag{2.5}$$

For low speed flow, $M^2 << 1$, one can see from Equation (2.5) that $\rho \approx \rho_0$. Thus, though the flow is not strictly "incompressible", it is of essentially constant density.

The mass flow per unit area is represented by the equation

$$\frac{\dot{m}}{A} = \rho V. \tag{2.8}$$

Using the identities $M = \frac{V}{A}$ and $a = \sqrt{\gamma RT}$ along with Equation (2.2), one may express the velocity as

$$V = M \sqrt{\frac{\gamma R T_0}{1 + \frac{\gamma - 1}{2} M^2}}. \tag{2.9}$$

Equation (2.9), along with equation (2.5), allows for the mass flow rate to be written as

$$\frac{\dot{m}}{A} = \frac{P_0 \sqrt{\gamma}\, M}{\sqrt{RT_0}} \left(\frac{1}{1 + \frac{\gamma - 1}{2} M^2}\right)^{\frac{\gamma + 1}{2(\gamma - 1)}} \tag{2.10}$$

For a given fluid (γ, R) and inlet state (P_0, T_0), one can rationalize that the mass flow per unit area is a maximum at M=1. Labeling the properties of the flow at M=1 with an asterisk[2] results in the maximum flow per unit area being defined as

$$\frac{\dot{m}}{A^*} = \frac{P_0}{\sqrt{RT_0}} \sqrt{\gamma} \left(\frac{2}{\gamma + 1}\right)^{\frac{\gamma + 1}{2(\gamma - 1)}}. \tag{2.11}$$

[2] A^* is the flow area corresponding to a Mach number equal to one. In a CD nozzle, this condition occurs at the nozzle throat.

Through the combination of Equation (2.10) with Equation (2.11), one ends with a very useful relation defining the ratio of the actual flow area, A, to the throat area, A^*, as depicted in Equation (2.12).

$$\frac{A}{A^*} = \frac{1}{M}\left[\frac{2}{\gamma+1}\left(1+\frac{\gamma-1}{2}M^2\right)\right]^{\frac{\gamma+1}{2(\gamma-1)}} \tag{2.12}$$

For the present work, the mass flow model presented in Equation (2.11) will be referred to as the ideal mass flow, $\dot{m}_{ideal}$. This model provides a first order estimate of the actual mass flow through the nozzle. Deviation from the ideal occurs when non-ideal flow mechanisms, such as viscous effects, are considered. The deviation of actual or measured nozzle parameters from those determined using one dimensional ideal gas flow relations is expressed through the coefficients of efficiency.

2.2 Coefficients of Efficiency – C_{fg}, C_d, C_V, and C_A

Two dimensionless parameters, typically used to measure the performance of exhaust nozzles, are the gross thrust coefficient, C_{fg}, and the flow coefficient, C_d. The gross thrust coefficient represents nozzle efficiency and is defined as the ratio of the actual gross thrust to the ideal available gross thrust. It is a parameter that includes losses due to friction, angularity, and expansion. What follows is a brief description of the gross thrust coefficient and the loss coefficients contributing to it.

2.2.1 Nozzle Efficiency - The Gross Thrust Coefficient

The gross thrust coefficient is a measure of nozzle efficiency defined as the ratio of actual nozzle gross thrust to ideal available gross thrust as shown in Equation (2.13) [1].

$$C_{fg} = \frac{F_{g,actual}}{F_{g,ideal}} \tag{2.13}$$

where the uninstalled gross thrust for a one-dimensional flow, $F_{g,actual}$, and the ideal gross thrust, $F_{g,ideal}$, are represented by Equations (2.14) and (2.15), respectively [1].

$$F_{g,actual} = \dot{m}_{8,actual}\left(\frac{V_9}{g_c}\right) + \left(P_9 - P_0\right) \tag{2.14}$$

$$F_{g,ideal} = \dot{m}_{8,ideal}\left(\frac{V_S}{g_c}\right) \tag{2.15}$$

where $\dot{m}_{8,actual}$ is the actual mass flow rate through the nozzle throat, V_9 is the nozzle exit velocity, P_9 is the pressure at the nozzle exit, P_0 is the ambient pressure, $\dot{m}_{8,ideal}$ is the ideal mass flow through the nozzle throat, V_S is the isentropic or fully expanded exit velocity, and g_c is the coefficient of gravity. Thus, with knowledge of the gross thrust coefficient, one can determine the actual gross thrust produced by an engine using the expression

$$F_{g,actual} = C_{fg} * F_{g,ideal}. \tag{2.16}$$

Employment of Equations (2.14) and (2.15) allows for the gross thrust coefficient to be written as [1]

$$C_{fg} = \frac{F_{g,actual}}{F_{g,ideal}} = \frac{\dot{m}_{8,actual}\left(\frac{V_9}{g_c}\right) + \left(P_9 - P_0\right)A_9}{\left(\frac{\dot{m}_{8,ideal}V_s}{g_c}\right)}. \tag{2.17}$$

The quantity $\left(P_9 - P_0\right)A_9$, shown in Equation (2.17), represents the loss of nozzle efficiency through expansion effects. Nozzle efficiency can also be reduced by other types of nozzle losses including losses caused by friction - momentum loss due to wall

friction in the nozzle and those caused by angularity effects - momentum loss due to nonaxial flow at the exit plane of the nozzle. Expansion losses, frictional losses, and losses due to angularity establish a baseline nozzle thrust coefficient curve as shown in Figure 2.1 for a typical converging diverging nozzle.

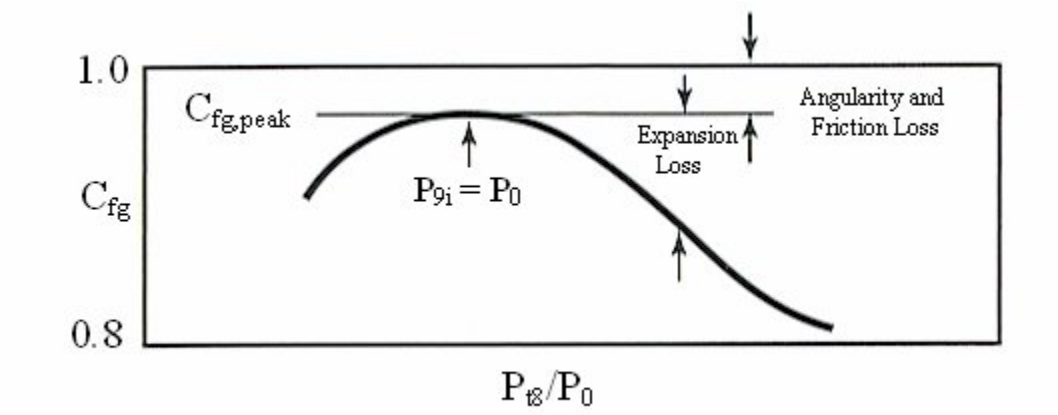

Figure 2.1 Baseline gross thrust coefficient for a converging diverging nozzle [2].

Equation (2.17) can be modified to include the effects friction and angularity by redefining the gross thrust coefficient, in the manner of Oates [2], as shown in Equation (2.18).

$$C_{fg} = \frac{C_V C_A \dot{m}_{8,actual}\left(\frac{V_{9,ideal}}{g_c}\right) + \left(P_{9i} - P_0\right)A_9}{\left(\frac{\dot{m}_{8,actual}V_s}{g_c}\right)} \tag{2.18}$$

where C_V is the velocity coefficient, C_A is the angularity coefficient, $\dot{m}_{8,actual}$ is the actual mass flow rate supplied to the nozzle or $\dot{m}_{8,actual} = C_{d8} * \dot{m}_{8,ideal}$, $V_{9,ideal}$ is the ideal velocity at the nozzle exit represented by Equation (2.19)[3]

$$V_{9,ideal} = \sqrt{Rg_c T_{t8}} \sqrt{\frac{2\gamma}{\gamma - 1}\left\{1 - \left(\frac{P_{9i}}{P_{t9i}}\right)^{(\gamma-1)/\gamma}\right\}}, \tag{2.19}$$

P_{9i} is the ideal static pressure at the nozzle exit and can be obtained using the isentropic flow relations[4], A_9 is the nozzle physical exit area, and V_s is the isentropic or fully expanded exit velocity defined as shown in Equation (2.20)

$$V_s = \sqrt{Rg_c T_{t8}} \sqrt{\frac{2\gamma}{\gamma - 1}\left\{1 - \left(\frac{P_0}{P_{t8}}\right)^{(\gamma-1)/\gamma}\right\}}. \tag{2.20}$$

When the thrust coefficient is at its peak, as shown in Figure 2.1, ideal expansion occurs where the ideal static exit pressure, P_{9i}, is equal to the ambient pressure, P_0, thus resulting in $V_{9,ideal} = V_s$. At this peak condition, the equation for the gross thrust coefficient reduces to

$$C_{fg,peak} = C_V C_A \tag{2.21}$$

At any other pressure ratio, the difference between $C_{fg,peak}$ and C_{fg} is a result of expansion losses which are attributable to "off design" operation (underexpansion - $P_9 > P_0$ and overexpansion - $P_9 < P_0$).

[3] In this equation, $P_{t,9i}$ is the ideal stagnation pressure at the nozzle exit. The ideal stagnation pressure at the nozzle exit, $P_{t,9i}$, is equal to the stagnation pressure at the nozzle throat, P_{t8}.

[4] P_{9i}/P_{t9i} is obtained by determining the ratio of A_9 (the physical exit area of the nozzle) to $A_{8,actual}$ (the nozzle throat physical area less the boundary layer thickness) and then using the isentropic flow relations to determine P_{9i}/P_{t9i}. $P_{t,9i}$, is known to be equal to the stagnation pressure at the nozzle throat, P_{t8}.

In reference to Equation (2.18), the velocity coefficient (C_V) provides a means for expressing the effects of friction through the nozzle while the angularity coefficient (C_A) quantifies the angularity losses. In addition to these two loss coefficients, the quantity $\left(P_{9i} - P_0\right)A_9$ represents the loss of nozzle efficiency through expansion effects. Due to the importance of each of these quantities to this analysis, a brief summary of each is provided.

2.2.2 The Discharge Coefficient

The discharge coefficient, C_d, (or flow coefficient, as it is sometimes called) is not a measure of efficiency but rather a parameter that sizes the nozzle to an engine. It is defined as the ratio of the actual mass flow rate to the ideal mass flow rate as is shown in Equation (2.22) [3].

$$C_{d\,8} = \frac{\dot{m}_{8,actual}}{\dot{m}_{8,ideal}} \tag{2.22}$$

In this relation, the ideal mass flow through the nozzle throat is predicted using the one-dimensional inviscid flow theory of Equation (2.11).

It can be shown that the discharge coefficient is also exactly equal to the ratio of the actual one-dimensional flow area required to pass the total nozzle flow to the ideal nozzle throat area as follows [3]:

$$C_{d\,8} = \frac{\dot{m}_{8,actual}}{\dot{m}_{8,ideal}} = \frac{\rho_8 V_8 A_{8,actual}}{\rho_8 V_8 A_{8,ideal}} = \frac{A_{8,actual}}{A_{8,ideal}} \tag{2.23}$$

where ρ_8 is the density at the nozzle throat, V_8 is the velocity of the flow through the nozzle throat, $A_{8,actual}$ is the physical nozzle throat area less the boundary layer thickness, and $A_{8,ideal}$ is the physical nozzle throat area.

Figure 2.2 depicts the variation of the discharge coefficient with nozzle pressure ratio for a converging diverging nozzle. Note the behavior of the discharge coefficient as the nozzle pressure ratio drops below choking (for a specific heat ratio of 1.4, choking occurs near a NPR of 2). This is a result of the venturi behavior[5] of the convergent-divergent nozzle.

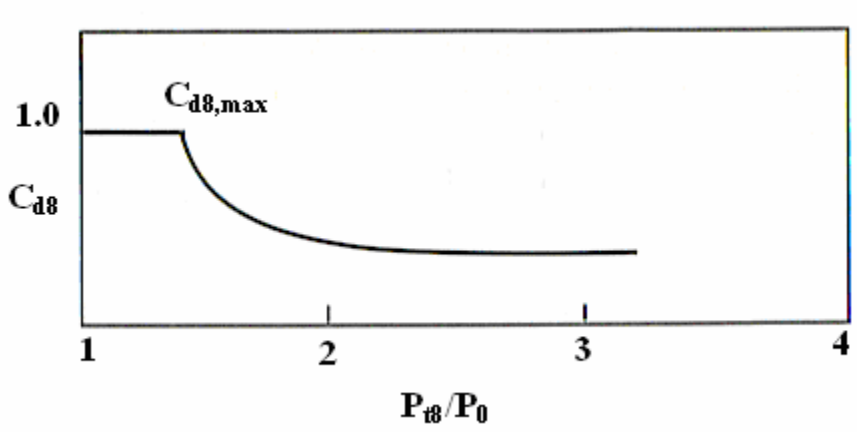

Figure 2.2 Nozzle discharge coefficient versus pressure ratio for a C-D nozzle [2].

2.2.3 The Velocity Coefficient

The velocity coefficient, C_V, is a representation of the effect of frictional loss in the boundary layer of the nozzle. Due to the fact that this coefficient is related to friction, it is essentially a function of the length of the diverging section of the nozzle, which

[5] As a fluid passes through a pipe that narrows or widens, the velocity and pressure of the fluid vary. As the pipe narrows, the velocity increases and the pressure decreases. As the pipe widens, the velocity decreases and the pressure increases. For the case of the CD nozzle, as A/A^* increases, P_{t8}/P_0 also increases. This causes a decrease in the discharge coefficient, C_{d8}.

depends on the nozzle area ratio, A_9/A_8, and the secondary nozzle half angle, α. It is defined as the ratio of the actual exit velocity to the ideal exit velocity as shown in Equation (2.24) [3].

$$C_V = \frac{V_{9,actual}}{V_{9,ideal}} \tag{2.24}$$

where $V_{9,actual}$ is the actual velocity at the nozzle exit as shown in Equation (2.25) [3] and $V_{9,ideal}$ is the ideal velocity at the nozzle exit as shown in Equation (2.26) [3].

$$V_{9,actual} = \sqrt{Rg_c T_{t8}} \sqrt{\frac{2\gamma}{\gamma - 1}\left\{1 - \left(\frac{P_9}{P_{t9}}\right)^{(\gamma-1)/\gamma}\right\}} \tag{2.25}$$

$$V_{9,ideal} = \sqrt{Rg_c T_{t8}} \sqrt{\frac{2\gamma}{\gamma - 1}\left\{1 - \left(\frac{P_{9i}}{P_{t9i}}\right)^{(\gamma-1)/\gamma}\right\}} \tag{2.26}$$

In each of these expressions R is the specific gas constant, g_c is the coefficient of gravity, T_{t8} is the stagnation temperature at the nozzle throat, γ is the specific heat ratio, P_9 is the measured or physical pressure at the nozzle exit, $P_{9,i}$ is the ideal pressure at the nozzle exit based on $\frac{A_9}{A_{8,actual}}$, P_{t9} is the physical or measured stagnation pressure at the nozzle exit, and $P_{t9,i}$ is the ideal stagnation pressure at the nozzle exit ($P_{t9,i} = P_{t8}$). For each of the relations shown in Equation (2.25) and Equation (2.26), the ratios $\frac{P_{9i}}{P_{t9i}}$ and $\frac{P_9}{P_{t9}}$ can be determined by employing the isentropic flow relations[6].

[6] P_{9i}/P_{t9i} is obtained by determining the ratio of A_9 (the physical exit area of the nozzle) to $A_{8,actual}$ (the nozzle throat physical area less the boundary layer thickness) and then using the isentropic flow relations to determine P_{9i}/P_{t9i}. P_9/P_{t9} is obtained by determining the ratio of A_9 (the physical exit area of the nozzle) to $A_{8,ideal}$ (the nozzle throat physical area) and then using the isentropic flow relations to determine P_9/P_{t9}.

Figure 2.3 presents the velocity coefficient as a function of the nozzle area ratio, $A_9/A_{8,ideal}$, and the secondary nozzle half angle, α, for a converging diverging nozzle. One can see from Figure 2.3 that, for each nozzle secondary half angle, α, the velocity coefficient decreases as $A_9/A_{8,ideal}$ increases. This is due to the fact that as α increases, the length of diverging portion of the nozzle decreases. This causes an decrease in frictional effects and hence, an increase in the velocity coefficient, $C_V = \frac{V_{9,actual}}{V_{9,ideal}}$.

A typical range for velocity coefficients is 0.992 to 0.997.

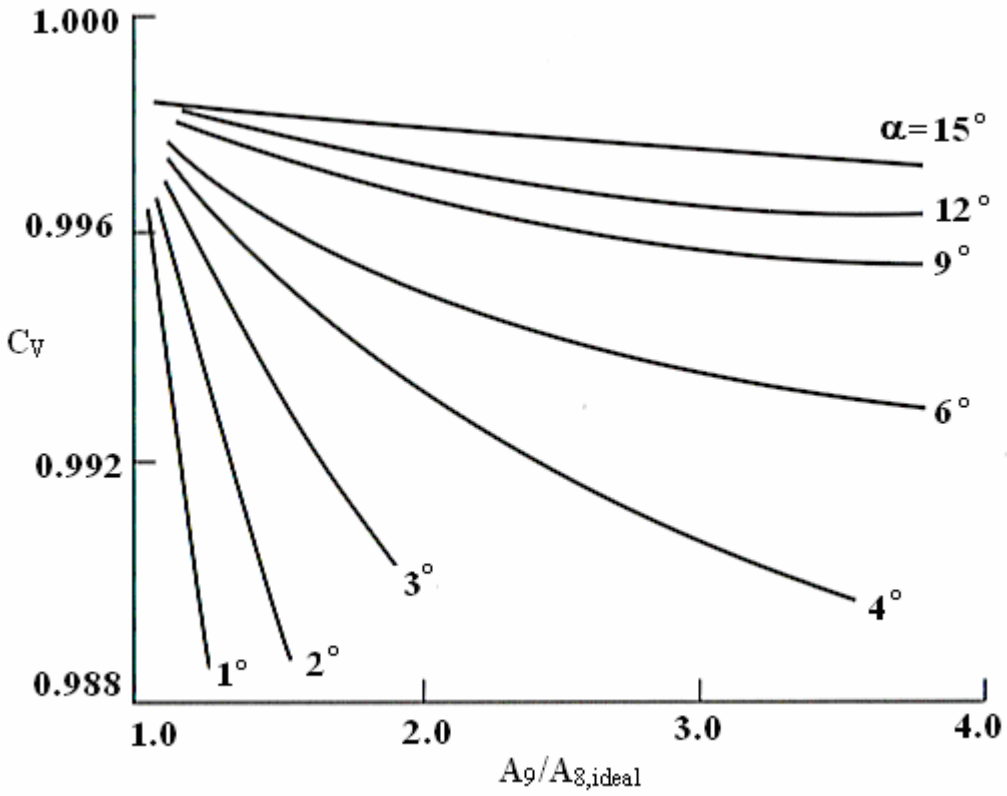

Figure 2.3 Velocity coefficient for a converging diverging nozzle [2].

2.2.4 The Angularity Coefficient

The angularity coefficient, C_A, represents the thrust loss resulting from the nonaxial exit of the exhaust gases from the nozzle as shown pictorially in Figure 2.4.

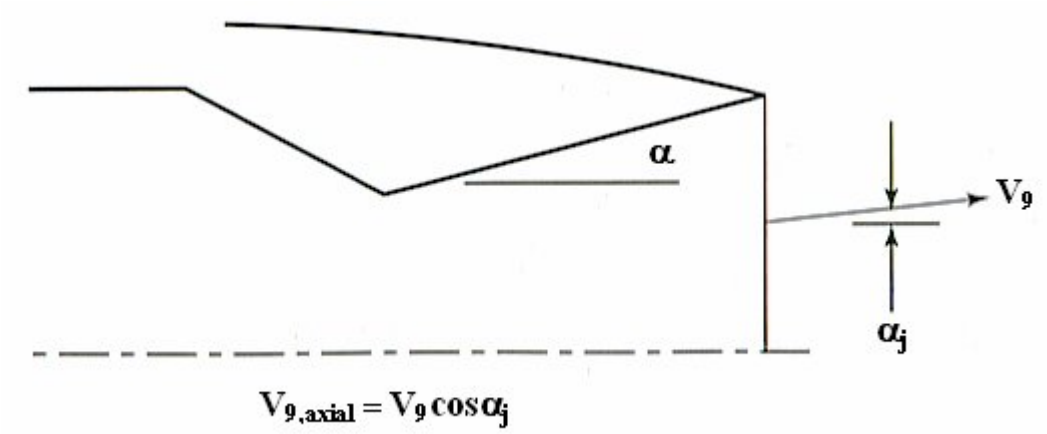

Figure 2.4 Local angularity coefficient for a 2D CD nozzle [2].

For a small element of flow, this coefficient simply becomes the cosine of the local flow exit angle, α_j, as shown in Equation (2.27) [2].

$$C_{A,j} = \frac{V_{9,axial}}{V_9} = \cos\alpha_j \tag{2.27}$$

The local flow angle, α_j, is not a constant across the nozzle exit, however, but varies, ideally, from zero at the nozzle center line to α at the outer radius. Thus, the overall nozzle angularity coefficient is the integral of cos α_j across the nozzle exit as shown in Equation (2.28) [2]. It must be noted that this equation for the angularity coefficient is based on the assumption of constant mass flow per unit area.

$$C_A = \frac{1}{A_9} \int_{r=0}^{r=R_9} \cos\alpha_j \, 2\pi r_j \, dr \tag{2.28}$$

In real nozzle geometries, there is a slight loss in efficiency because the exit static pressure is not equal to ambient pressure across the entire nozzle exit area. Thus, the angularity coefficient is adjusted to include this loss and results in the expression provided in Equation (2.29) [2].

$$C_A = \frac{1}{A_9} \int_{r=0}^{r=R_9} \cos\alpha_j \, 2\pi r_j \, dr \tag{2.29}$$

$$+ \frac{1}{\left(\dot{m}_{8,actual} V_{9i} / g \right)} \left[\int_{r=0}^{r=R_9} (P_{9j} - P_{9i}) 2\pi r_j \, dr + \int_{r=0}^{r=R_9} (V_{9j} - V_{9i}) \rho_{9j} V_{9j} \, 2\pi r_j \, dr \right]$$

Note that the second term in this equation is the static pressure variation loss while the third term is the velocity variation loss. Both of these losses are functions of nozzle geometry only. The trends depicted in Figure 2.5 represent an angularity coefficient given by Equation (2.29).

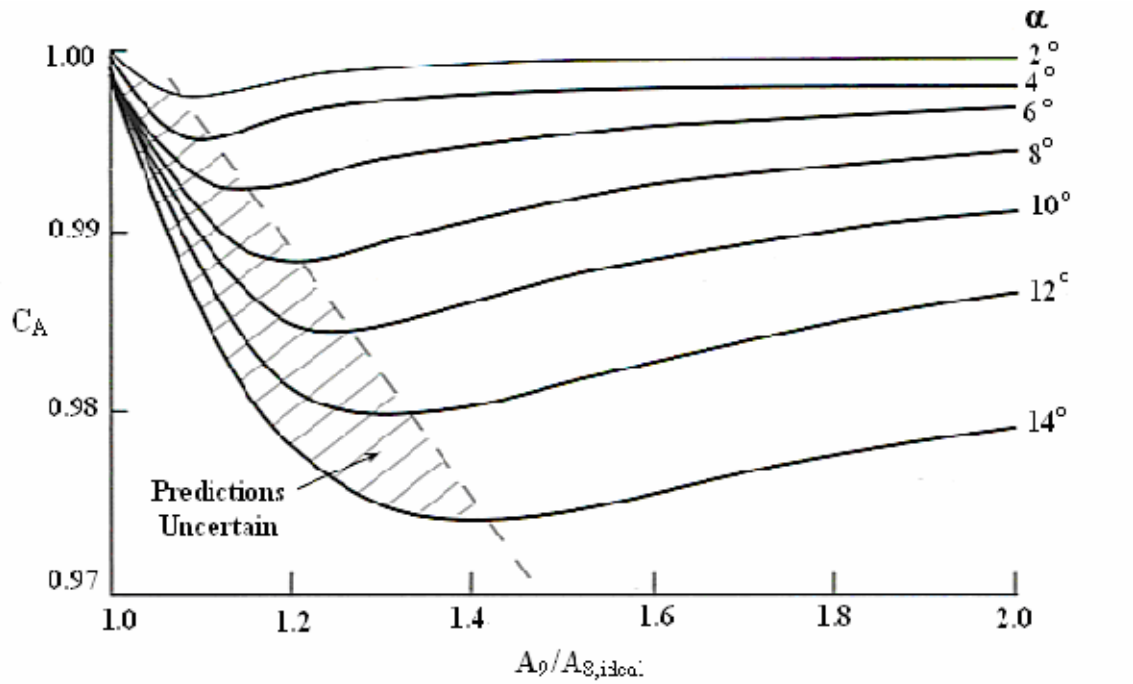

Figure 2.5 Convergent divergent nozzle angularity coefficient [2].

The dashed line region shown in Figure 2.5 represents nozzle geometries that are very short and most likely separated causing the analytical prediction to be invalid.

For nozzles with an area ratio below 1.1, the angularity coefficient usually falls within a range of 0.995 to 0.997 or higher. However, for higher area ratio nozzles, the loss can be up to 2% such that C_A is within the range 0.98 to 0.99.

3. Methodology – Nozzle Performance Prediction Code

A nozzle performance prediction code was developed to predict the thrust performance of a user defined non-axisymmetric two-dimensional converging diverging exhaust nozzle. What follows is a brief description of the code methodology.

3.1 Nozzle Geometry

Before the performance analysis can begin, the user must define the nozzle geometry. This program was designed to analyze nozzles characterized by smooth contoured throats, but it will be shown that this program may also be used to analyze nozzles characterized by sharp cornered throats. Figure 3.1 depicts the nozzle geometry for which this analysis is valid.

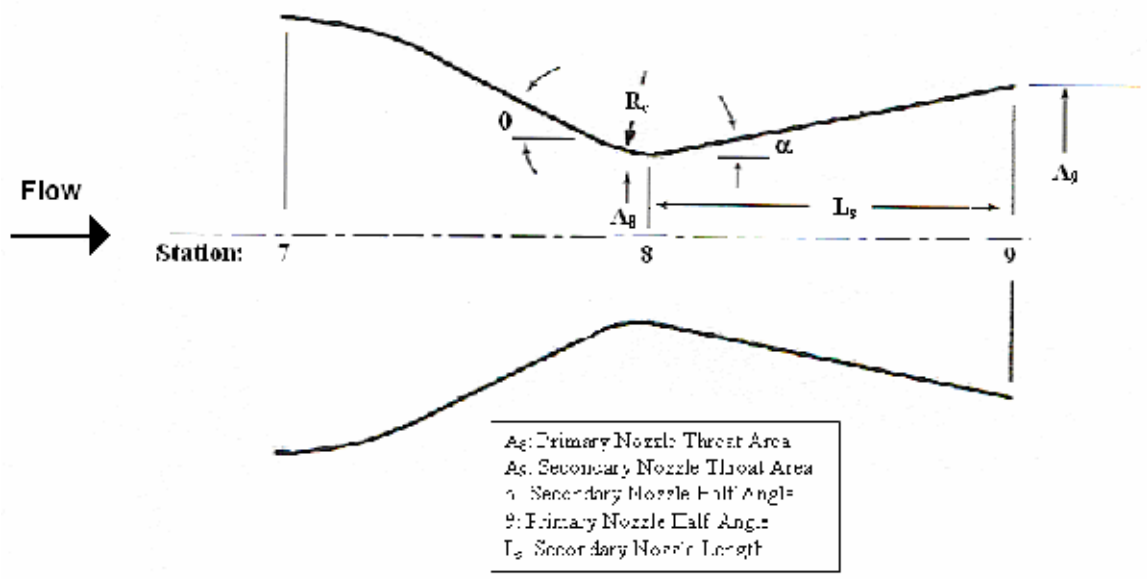

Figure 3.1 Non-axisymmetric two-dimensional converging diverging nozzle geometry

In this illustration, station 7 represents the nozzle entrance, station 8 the nozzle throat, and station 9 the nozzle exit. If the user chooses to analyze a nozzle with a sharp cornered throat, the radius of curvature is simply defined to be equal to zero. Once the nozzle geometry has been defined, the program begins the performance analysis.

3.2 Ideal Mass Model

After the nozzle geometry has been defined, the program user is asked to describe the gas at various locations throughout the nozzle. Specifically, the user is asked for the molecular weight of the gas as well as the atmospheric temperature and pressure. A file that includes a temperature range, corresponding specific heat ratios (gammas), and corresponding dynamic viscosities has been set up for the gas in question. The current file is set up for air. The user can modify this file if the gas of interest is not air.

The ideal mass flow through the nozzle throat is then calculated using the one dimensional isentropic flow relation provided in Equation (2.11). That relation is reproduced here corresponding to the conditions at the throat.

$$\frac{\dot{m}_8}{A^*} = \frac{P_{08}}{\sqrt{RT_{08}}}\sqrt{\gamma_8}\left(\frac{2}{\gamma_8+1}\right)^{\frac{\gamma_8+1}{2(\gamma_8-1)}} \tag{3.1}$$

As stated before, boundary layer development causes a mass flow deviation from the ideal by decreasing the area through which the mass can flow. The ratio of this decreased area to the ideal area, known as the discharge coefficient, is provided in Equation (3.2).

$$C_{d8} = \frac{\dot{m}_{8,actual}}{\dot{m}_{8,ideal}} = \frac{\rho_8 V_8 A_{8,actual}}{\rho_8 V_8 A_{8,ideal}} = \frac{A_{8,actual}}{A_{8,ideal}} \tag{3.2}$$

Thus, the actual mass flow through the nozzle throat can be determined using the expressions provided in Equations (3.3) and (3.4).

$$\dot{m}_{8,actual} = C_{d8} * \dot{m}_{8,ideal} \tag{3.3}$$

$$\dot{m}_{8,actual} = \left(\frac{A_{8,actual}}{A_{8,ideal}} \right) * \dot{m}_{8,ideal} \tag{3.4}$$

3.3 Discharge Coefficient, C_{d8}

As stated earlier, the discharge coefficient is defined as the ratio of the actual mass flow at the nozzle throat, $\dot{m}_8$, to the ideal mass flow at the nozzle throat, $\dot{m}_{8i}$. The ideal mass flow model given by Equation (3.1) provides a convenient first order estimate of the mass flow through the nozzle. The ideal mass flow model can be used as a baseline $\left(C_{d8} = \frac{\dot{m}_{8,actual}}{\dot{m}_{8,ideal}} = 1 \right)$ from which to subtract non-ideal effects such as multi-dimensional effects and viscous effects. Consequently, the discharge coefficient can be expressed as

$$C_d = 1 - \Delta C_{d,inv} - \Delta C_{d,vis} \tag{3.5}$$

where $\Delta C_{d,inv}$ is the reduction in C_d due to multi-dimensional[7] effects and $\Delta C_{d,vis}$ is the reduction in C_d due to viscous effects. The change in C_d due to each non-ideal effect is represented mathematically by the following expressions:

$$\Delta C_{d,vis} = 1 - C_{d,vis} \tag{3.6}$$

$$\Delta C_{d,inv} = 1 - C_{d,inv}. \tag{3.7}$$

Substitution of these relations into Equation (3.5) yields Equation (3.8).

$$C_d = 1 - (1 - C_{d,inv}) - (1 - C_{d,vis}) \tag{3.8}$$

[7] In this case, two-dimensional inviscid discharge effects are considered.

As can be seen in Equation (3.8), the analytic characterization of C_d becomes an exercise in determining a discharge coefficient for each non-ideal effect relative to the baseline estimation of C_d=1.

Knowledge of the discharge coefficient and ideal mass flow through the nozzle throat, $\dot{m}_{8,ideal}$, allow for the direct determination of the actual mass flow through the nozzle throat, $\dot{m}_{8,actual} = C_{d8} * \dot{m}_{8,ideal}$. The actual mass flow through the nozzle throat, $\dot{m}_{8,actual}$, is necessary for the solution of the gross thrust coefficient equation as depicted in Equation (2.18).

The remainder of this section is devoted to the presentation of previously developed methods for determining $C_{d,inv}$ and $C_{d,vis}$.

3.3.1 Hall's [4] Analytical Model for Determining the Inviscid Discharge Coefficient

Closed form analytical expressions for the inviscid discharge coefficient, $C_{d,inv}$, have been developed by several researchers – Stratford [4], Masure [5], and Hall [6]. Among several works that have been published, the most widely used solution is credited to Hall [6] who solved the equation in axisymmetric coordinates by employing a series solution of four terms. Hall's [6] expression for the inviscid discharge coefficient is expressed as

$$C_{d,inv} = 1 - (\gamma + 1)\Omega^2 \left(\frac{1}{96} + \frac{8\gamma + 21}{4608}\Omega + \frac{754\gamma^2 + 1971\gamma + 2307}{552960}\Omega^2 \right) \qquad (3.9)$$

where $\Omega = \frac{R_t}{R_c}$, R_t is the throat radius, and R_c is the radius of curvature at the nozzle throat. It should be mentioned that this series diverges for Ω greater than unity so that

solutions may be less accurate for Ω slightly greater than unity and invalid for values of Ω considerably greater than unity.

Preliminary tests on a number of nozzles showed that the analytical expression developed by Hall [6] for the inviscid discharge coefficient, $C_{d,inv}$, diverged for many of the nozzle geometries considered for analysis because the nozzle radius ratio, $\Omega = \frac{R_t}{R_c}$, was greater than unity. Table 3.1 provides a list of the radius ratios for each nozzle configuration considered in this study. As can be seen in Table 3.1, the radius ratio varies from values less than one to values much greater than one.

Table 3.1 Radius ratio data for each nozzle configuration.

Nozzle Configuration	Radius Ratio R_t/R_c
A1	2.831
A2	0.7026
B1	2.831
B2	0.7026
B3	0.7026
Hunter Case 2	1.2158
Hunter Case 3	1.216
Hunter Case 4	14680

To solve the problem of inviscid discharge coefficient divergence, two possible solutions were considered - the first being based on omitting the inviscid discharge coefficient from the overall discharge coefficient relation and relying solely on the discharge coefficient method of Tang and Fenn [7] (introduced in section 3.3.2) and the second being based on the inclusion of an inviscid discharge coefficient that would be a constant for every nozzle geometry considered.

For the second solution method, inviscid discharge coefficient data was generated for nozzle radius ratios of 0.05 to 0.95. The median value, over this radius ratio range, of 0.9915 was selected for the inviscid discharge coefficient and inserted into the nozzle performance code as a constant for any radius ratio value considered.

Preliminary computational results were generated for these two methods and compared to experimental results for each nozzle geometry considered in this analysis. These results are provided in the Appendix. From this study, one can see that the plots provided in Appendix A provide evidence that omitting the inviscid discharge coefficient from the overall discharge coefficient relation provides computational results that continuously overpredict the experimental data. The inclusion of a constant inviscid discharge coefficient of 0.9915, however, provides an excellent comparison to the experimental data for a wide range of nozzle radius ratios. For this reason, it was decided that the inviscid discharge coefficient would be included in the nozzle performance code as a constant of 0.9915 for any radius ratio value considered.

3.3.2 Tang's [7] Analytical Model for Determining the Viscous Discharge Coefficient

A number of researchers – Stratford [4], Tang and Fenn [7], and Geropp [8] - have also examined the manner in with viscous effects influence the nozzle mass flow. As mentioned before, viscous effects retard the flow near the wall creating a boundary layer with a corresponding displacement thickness, δ^*. The displacement thickness decreases the actual area through which the mass can flow thus creating a decrease in mass flow. Using the relation $C_{d8} = \frac{\dot{m}_{8,actual}}{\dot{m}_{8,ideal}} = \frac{\rho_8 V_8 A_{8,actual}}{\rho_8 V_8 A_{8,ideal}} = \frac{A_{8,actual}}{A_{8,ideal}}$, one can express the viscous discharge coefficient, as done by Johnson [9], as

$$C_{d,vis} = \left(1 - 2\frac{\delta^*}{d}\right)^2 \tag{3.10}$$

where δ^* is the displacement thickness and d is the nozzle throat diameter.

An assortment of boundary layer methods has been developed to estimate the throat displacement thickness for nozzle flows. The method considered here, is one developed separately by both Geropp [8] and Tang and Fenn [7]. Geropp [8] and Tang and Fenn[8] [7] independently developed similarity solutions to predict the displacement thickness by utilizing the following assumptions:

(1) perfect gas with a constant specific heat,

(2) external to the boundary layer the flow is one-dimensional and inviscid,

(3) Prandtl number equal to unity,

(4) adiabatic nozzle wall,

(5) molecular viscosity has a linear dependence on temperature,

(6) nozzle wall radius of curvature much larger than the boundary layer thickness, and

(7) pressure gradient parameter, β, equal to infinity.

The insertion of Tang's and Fenn's [7] expression for the displacement thickness into Equation (3.10) supplies the following expression for the viscous discharge coefficient.

[8] The expression of Tang and Fenn, for the viscous discharge coefficient, is identical to Geropp's with the exception that it includes an additional term that is inversely proportional to the Reynolds number.

$$C_{d,vis} = 1 - \left(\frac{\gamma+1}{2}\right)^{1/4}\left[\frac{8\left(9-4\sqrt{6}\right)}{3\left(\gamma+1\right)} + \frac{4\sqrt{6}}{3}\right]\left(\overline{\mathrm{Re}}_D^*\right)^{-1/2} + \frac{2\sqrt{2}}{3}\frac{\left(\gamma-1\right)\left(\gamma+2\right)}{\sqrt{\gamma+1}}\left(\overline{\mathrm{Re}}_D^*\right)^{-1} \tag{3.11}$$

where γ is the specific heat ratio, $\overline{\mathrm{Re}}_D^*$ is a modified Reynolds number defined as $\overline{\mathrm{Re}}_D^* = \Omega^{1/2}\left(\frac{\rho_e u_e D}{\mu_e}\right)_*$ where D is the diameter of the nozzle at the throat, $\Omega = \frac{R_t}{R_c}$, ρ is the density, u is the velocity, and μ is the viscosity. The subscript e indicates freestream values while the asterisk indicates conditions at the nozzle throat.

For Reynolds numbers less than 1000, Tang's and Fenn's [7] computational viscous discharge coefficient underpredicts their experimental discharge coefficient[9]. Tang and Fenn [7] attempted to correct for this underprediction by modifying his expression to include the effects of non-unity Prandtl numbers. This modification is represented through the modified Reynolds number as $\overline{\mathrm{Re}}_D^* = \left(\frac{R_c\,\mathrm{Pr}}{R_t}\right)^{-1/2}\left(\frac{\rho_e u_e D}{\mu_e}\right)_*$. Even after the correction for Prandtl number, there remains a consistent excess in the measured values of C_d for Reynolds numbers less than 1000.

Due to the overprediction of the discharge coefficient by the method of Tang and Fenn [7] for Reynolds numbers less than 1000, the method of Kuluva and Hosack [10] was considered for this low Reynolds number range.

[9] Tang and Fenn [7] experimentally determined discharge coefficients for various gases (hydrogen, helium, nitrogen, and argon) over a Reynolds number range of 10^2 to 10^4.

3.3.3 Kuluva's Analytical Model for Determining the Viscous Discharge Coefficient

The following analytical model for discharge coefficient determination is courtesy of Kuluva and Hosack [10] who presented a simple formula for the calculation of the discharge coefficient in the throat Reynolds number range of 50 to 1000 for a wide range of nozzle geometries.

In their approach, Kuluva and Hosack [10] write the discharge coefficient for flow through a nozzle as

$$C_{d,vis} = \frac{\left(R_t^2 - 2R_t\delta_t^*\right)}{R_t^2} \tag{3.12}$$

where R_t is the throat radius and δ_t^* is the displacement thickness at the throat. Thus, in order to determine the discharge coefficient at the nozzle throat, it is only necessary to calculate the displacement thickness at this location.

Kuluva and Hosack [10] theorized that because of the flow acceleration in a nozzle, the boundary layer and momentum thickness reach their minimum values at, or quite near, the nozzle throat and that this observation coupled with the knowledge of the axial change of Mach number would provide a simple means for calculating the displacement thickness. Thus, in order to determine the discharge coefficient, the boundary layer equations would only need to be solved algebraically at the nozzle throat.

The formulation of Kuluva's and Hosack's [10] boundary layer equations is based on the following assumptions:

(1) the displacement thickness is a minimum at the nozzle throat,

(2) curvature effects can be neglected ($\delta/r<<1$),

(3) velocity slip effects at the wall can be neglected, and

(4) the flow is adiabatic.

These assumptions result in relations between the momentum thickness, boundary layer thickness, and boundary layer displacement thickness through which the following expression for the viscous discharge coefficient is determined.

$$C_{d,vis} = \left(\frac{R_c + 0.05R_t}{R_c + 0.75R_t} \right)^{0.019} \left[1 - \left(\frac{R_c + 0.10R_t}{R_t} \right)^{0.21} \left(\frac{1}{\mathrm{Re}} \right)^{1/2} f(\gamma) \right] \tag{3.13}$$

where R_c is the throat radius of curvature, R_t is the nozzle throat radius, Re is the throat Reynolds number represented by $\mathrm{Re} = \left(\frac{4\dot{m}_{ideal}}{\pi d_t \mu_0} \right)$, and f(γ) is represented by Equation (3.14).

$$f(\gamma) = 2A(\gamma) \left\{ \frac{\pi A(\gamma)}{\left(\frac{\gamma+1}{2} \right)^{1/2} \left[A(\gamma) + B(\gamma) - 1 + \frac{2}{\pi} \left(\frac{2}{\gamma+1} \right)^{1/2} B(\gamma) \right]} \right\}^{1/2} \tag{3.14}$$

where

$$A(\gamma) = 1 - \frac{2}{\pi} \left(\frac{2}{\gamma-1} \right)^{1/2} \tan^{-1} \left(\frac{\gamma-1}{2} \right) \tag{3.15}$$

and

$$B(\gamma) = \frac{\left(\frac{\gamma+1}{2} \right)^{1/2} - 1}{\left(\frac{\gamma-1}{2} \right)}. \tag{3.16}$$

Kuluva's and Hosack's [10] theory was shown to correlate well with their experimental data[10] for Reynolds numbers less than 1000.

The method discussed in sections 3.3.1 is used to determine the inviscid discharge coefficient while the methods of sections 3.3.2 and 3.3.3 are used to determine the viscous discharge coefficient. Due to the error resulting from Tang's and Fenn's [7] expression for Reynolds numbers less than 1000, it was decided that Tang's and Fenn's [7] analytical model would be used to determine the viscous discharge coefficient for Reynolds numbers greater than 1000, and Kuluva's and Hosack's [10] would be used for Reynolds numbers less than 1000.

It is necessary to mention here that the methods of Hall [6], Tang and Fenn [7], and Kuluva and Hosack [10] are used for the analysis of nozzles with circular cross sections. Thus, these methods were modified so that they could be used to analyze nozzles with cross-sectional shapes other than circular. The idea behind the modification is the definition of a geometrical parameter that will take the place of the nozzle throat radius in Equations (3.9, 3.11, and 3.13) as well as in all Reynolds number representations.

For the purpose of this analysis, this parameter will be defined as an effective diameter shown in Equation (3.17).

$$D_{eff} = D_h \frac{16}{\left(C_f \, \mathrm{Re}_{Dh}\right)_{la\,\min ar}} \tag{3.17}$$

[10] Kuluva and Hosack [10] conducted an experiment to determine the validity of their theory for discharge coefficient determination. Measurements were taken, at throat Reynolds numbers less than 1000, for argon and nitrogen gases.

where $D_h = \frac{4A}{P}$ is the hydraulic diameter, C_f is the skin friction coefficient or Fanning friction factor, and $\mathrm{Re}_{Dh} = \frac{\rho \bar{u} D_h}{\mu}$ is the Reynolds number based on the hydraulic diameter. The concept of an effective diameter was proposed and proven experimentally by O.C. Jones in tests on rectangular [11] and concentric angular ducts [12] and should work well for any squatty or blocky cross section.

The hydraulic diameter concept is one that arose due to the failure of the Darcy friction factor definition for a noncircular duct. The proposed definition of the Darcy friction factor, $\lambda = \frac{8\tau_w}{\rho \bar{u}^2}$, does not work for a non-circular duct because the wall shear stress, τ_w, varies around the perimeter. A partial remedy is to define a mean wall shear stress, as done in White [13], as

$$\bar{\tau}_w = \frac{1}{P}\int_0^P \tau_w ds \tag{3.18}$$

where ds is an element of arc length and P is the perimeter of the shape in question.
If a slug of fluid passing through a duct is isolated and one assumes that there is no net momentum flux due to the fully developed flow, the net pressure and the wall shear force on the fluid can be equated as follows:

$$dx\int_0^P \tau_w ds = -A d\hat{p} \tag{3.19}$$

Or, from the definition of mean shear,

$$\bar{\tau}_w = \frac{A}{P}\left(-\frac{d\hat{p}}{dx}\right) \tag{3.20}$$

This relation for mean shear stress is exactly analogous to the equation of shear stress for circular duct flow. This analysis provides a definition for the hydraulic diameter of a non-circular duct, shown in Equation (3.21), as well as a redefined Darcy friction factor given in Equation (3.22).

$$D_h = \frac{4A}{P} = \frac{4 * Area}{Wetted\ Perimeter} \tag{3.21}$$

$$\lambda = \frac{8\bar{\tau}_w}{\rho \bar{u}^2} \tag{3.22}$$

In order to determine the mean shear stress given by Equation (3.20), one must have a method for evaluating the pressure gradient, $\frac{-dP}{dx}$. Fortunately, there exists an enormous number of exact solutions for noncircular shapes as reviewed by Berker [14]. The shapes of interest considered in this study are rectangular, square, and circular cross sections. The velocity distribution and volume flow rate results for each are provided in Equations (3.23-3.28).

Rectangular Section: $-a \le y \le a$, $-b \le z \le b$:

$$u(y,z) = \frac{16a^2}{\mu\pi^3}\left(\frac{-d\hat{p}}{dx}\right)\sum_{i=1,3,5,\ldots}^{\infty}(-1)^{\frac{i-1}{2}}\left[1-\frac{\cosh\left(\frac{i\pi z}{2a}\right)}{\cosh\left(\frac{i\pi b}{2a}\right)}\right]\left(\frac{\cos\left(\frac{i\pi y}{2a}\right)}{i^3}\right) \tag{3.23}$$

$$Q = \frac{4ba^3}{3\mu}\left(\frac{-d\hat{p}}{dx}\right)\left[1-\frac{192a}{\pi^5 b}\sum_{i=1,3,5,\ldots}^{\infty}\frac{\tanh\left(\frac{i\pi b}{2a}\right)}{i^5}\right] \tag{3.24}$$

Circular Section[11]:

$$u(r) = \frac{\left(-\frac{d\hat{p}}{dx}\right)}{4\mu}\left(R_0^2 - R^2\right) \tag{3.25}$$

$$Q = \frac{\pi R_0^4}{8\mu}\left(-\frac{d\hat{p}}{dx}\right) \tag{3.26}$$

Square Section: $-a \le y \le a$, $-b \le z \le b$, $a = b$

$$u(y,z) = \frac{16a^2}{\mu\pi^3}\left(-\frac{d\hat{p}}{dx}\right)\sum_{i=1,3,5,\ldots}^{\infty}(-1)^{\frac{i-1}{2}}\left[1-\frac{\cosh\left(\frac{i\pi z}{2a}\right)}{\cosh\left(\frac{i\pi b}{2a}\right)}\right]\left(\frac{\cos\left(\frac{i\pi y}{2a}\right)}{i^3}\right) \tag{3.27}$$

$$Q = \frac{4ba^3}{3\mu}\left(-\frac{d\hat{p}}{dx}\right)\left[1-\frac{192a}{\pi^5 b}\sum_{i=1,3,5,\ldots}^{\infty}\frac{\tanh\left(\frac{i\pi b}{2a}\right)}{i^5}\right] \tag{3.28}$$

For each of these equations, the knowledge of the flow rate through the nozzle throat allows for computation of the pressure gradient. The mean shear stress can then be determined using Equation (3.20) followed by calculation of the Darcy friction factor

[11] It should be mentioned here that if the above analysis is done for a circular cross section, both the hydraulic diameter and the effective diameter will end up being exactly equal to the diameter of the circle as would be expected. The equations for a circular cross section are provided here for completeness.

through Equation (3.22), the skin friction coefficient $C_f = \frac{\lambda}{4}$, and lastly the effective diameter through Equation (3.17). Insertion of the effective radius (1/2 the effective diameter) into Equations (3.9), (3.11), and (3.13) allows for the direct determination of nozzle discharge coefficient for any specified cross sectional shape.

3.4 Velocity Coefficient, C_V

To determine the velocity coefficient, the program uses the nozzle throat area and exit area, input by the user, to calculate an ideal area ratio, $\frac{A}{A^*}|_{9i} = \left(\frac{A_9}{C_d A_8} \right)$, and actual area ratio, $\frac{A}{A^*}|_9 = \left(\frac{P_{t9}}{P_{t8}} \right)\left(\frac{A_9}{C_d A_8} \right)$. Once the area ratios for both the actual and ideal cases have been determined, the corresponding Mach numbers and pressure ratios are found using the isentropic flow relations given in Equations (2.4) and (2.12). From this, the program solves Equation (2.26) for the ideal exit velocity and Equation (2.25) for the actual exit velocity.

$$V_{9,ideal} = \sqrt{Rg_c T_{t8}} \sqrt{\frac{2\gamma}{\gamma - 1}\left\{ 1 - \left(\frac{P_{9i}}{P_{t9i}} \right)^{(\gamma-1)/\gamma} \right\}} \tag{2.26}$$

$$V_{9,actual} = \sqrt{Rg_c T_{t8}} \sqrt{\frac{2\gamma}{\gamma - 1}\left\{ 1 - \left(\frac{P_9}{P_{t9}} \right)^{(\gamma-1)/\gamma} \right\}} \tag{2.25}$$

In each of these expressions R is the specific gas constant, g_c is the coefficient of gravity, T_{t8} is the stagnation temperature at the nozzle throat, γ is the specific heat ratio, P_9 is the measured or physical pressure at the nozzle exit, $P_{9,i}$ is the ideal pressure at the nozzle

exit based on $\frac{A_9}{A_{8,actual}}$, P_{t9} is the physical or measured stagnation pressure at the nozzle exit, and $P_{t9,i}$ is the ideal stagnation pressure at the nozzle exit ($P_{t9,i} = P_{t8}$). For each of these relations, the ratios $\frac{P_{9i}}{P_{t9i}}$ and $\frac{P_9}{P_{t9}}$ can be determined by employing the isentropic flow relations.

The velocity coefficient, C_V, is then determined by inserting the ideal and actual exit velocity results into Equation (3.29).

$$C_V = \frac{V_{9,actual}}{V_{9,ideal}} \tag{3.29}$$

3.5 Angularity Coefficient, C_A

In order to determine the nozzle angularity coefficient, the program first has to determine the local flow angle of the exhaust gas leaving the nozzle. As stated before, the local flow angle, α_j, is not a constant across the nozzle exit, but actually varies from zero at the nozzle center line to α at the outer radius. The method of characteristics was included in the program for the purpose of determining the variance of the local flow angle at the nozzle exit.

The method of characteristics is a classical technique used for the solution of inviscid supersonic and hypersonic flows, both internal and external. For this analysis, an assumption of a two-dimensional, supersonic steady flow of a perfect gas with constant specific heats is made and satisfied by using an average specific heat ratio, $\gamma_{average} = \left(\frac{\gamma_8 + \gamma_9}{2} \right)$, throughout the nozzle.

The analysis begins at the nozzle throat (station one), where the flow properties are known, and continues outward. The flow geometry examined by the program is assumed symmetric across the nozzle centerline making it necessary to consider only half of the flow above or below the centerline. The half of the flow under consideration is divided into a user defined number of equally spaced nodes, i, such that θ_1 is 0° at the centerline and θ_i is the secondary nozzle half angle, α. At each node, there exist two characteristic lines, C_1 and C_2, defined as lines across which there exists a discontinuity in the velocity gradient. The slopes of these lines are expressed in polar coordinates, as shown by John [15], as

$$\left(\frac{dy}{dx}\right)_1 = \tan(\theta - \mu) \tag{3.30}$$

$$\left(\frac{dy}{dx}\right)_2 = \tan(\theta + \mu) \tag{3.31}$$

where θ defines the flow direction and μ is the Mach angle, $\mu = \sin^{-1}\left(\frac{1}{M}\right)$.

The intersection of two characteristic lines defines a new station of nodes at which new flow properties (Mach number, flow angle, etc.) are determined. This process is continued until the end of the secondary nozzle has been reached. The properties calculated at this point are the nozzle exit properties and thus provide the exit flow angle variation.

Appendix B presents a comparison of the output provided by the method of characteristics subroutine to an example method of characteristics problem depicted in the textbook *Gas Dynamics* [15]. One can see, from a comparison of Table B1 with

Table B2 that the method of characteristics subroutine results compare extremely well with those results provided in *Gas Dynamics* [15].

Once the nozzle exit angle variation is known, the program calculates the angularity coefficient using Equation (2.28).

$$C_A = \frac{1}{A_9} \int_{r=0}^{r=R_9} \cos\alpha_j \, 2\pi r_j \, dr \tag{2.28}$$

Note that this equation is for a nozzle with a circular cross section. If the user specifies a nozzle of square or rectangular cross section, an equivalent relation corresponding to the defined shape is used.

It should be noted that this MOC model is applicable to two-dimensional nozzle geometries only. However, this model could easily be expanded to include other nozzle geometries, particularly axisymmetric converging diverging nozzles. Expansion of this prediction model to include axisymmetric converging diverging nozzles would only require modification to the current method of characteristics subroutine (from two dimensions to three dimensions).

4.7 Gross Thrust Coefficient, C_{fg}

When the nozzle loss coefficients have been determined, the program calculates the gross thrust coefficient, for the user specified operating conditions, using Equation (2.18).

$$C_{fg} = \frac{C_V C_A \dot{m}_{8,actual} \left(\frac{V_{9i}}{g_c} \right) + \left(P_{9i} - P_0 \right) A_9}{\left(\frac{\dot{m}_{8,actual} V_s}{g_c} \right)} \tag{2.18}$$

This program was used to generate gross thrust coefficient data for a number of different nozzle geometries. A brief program user's guide is provided Appendix C.

4. Results and Analysis

A number of researchers – Mason, Putnam, and Re [16], Berrier and Re [17], Hunter [18], and Cappone and Berrier [19] - have conducted experiments on a variety of nozzle geometries to understand the effect of various parameters on nozzle gross thrust coefficient. In order to emphasize its capability, the results generated by the nozzle performance prediction code are compared to the experimental results of these researchers as well as to the computational results produced by existing codes developed by Hunter [20] and Cline [21].

4.1 The Experiment of Mason, Putnam, and Re [16]

Mason, Putnam, and Re [16] conducted an experiment to determine the effect of throat contouring on nozzle internal performance. They tested five non-axisymmetric converging-diverging nozzles in the static test facility of the Langley 16 foot transonic tunnel and recorded internal performance data at nozzle pressure ratios up to 9.0.

For their experiment, two CD nozzles, A1 and B1, were used as baseline nozzle geometries. These baseline geometries were modified by increasing the throat radius of curvature while holding all other geometric parameters constant except for the primary nozzle half angle, θ, and the secondary nozzle half angle, α. The modified nozzle geometries are labeled as A2, B2, and B3. There are two main differences between the category A and B nozzles – (1) the expansion ratio of the category B nozzles is larger

than those of category A (1.8 compared to 1.09) and (2) the secondary nozzle half angle, α, of the category B nozzles is larger than those of category A (10.85° and 11.24° compared to 1.21°). The two baseline geometries as well as the modified geometries were tested and the data from each recorded.

4.1.1 Configuration A1 and A2

The nozzle geometry of A1 and A2 is shown in Figure 4.1. A table listing the design parameters for each configuration is provided in Table 4.1 as well. Note that these two geometries differ through their radii of curvature and primary nozzle half angles.

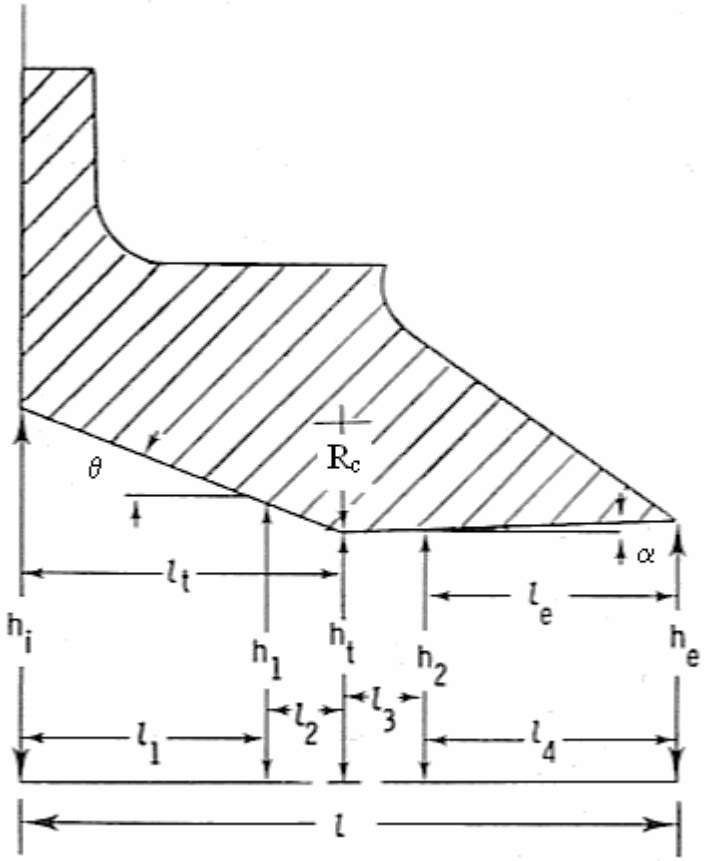

Figure 4.1 Nozzle geometry for configurations A1 and A2 [16].

Table 4.1 Nozzle design parameters for configurations A1 and A2 [16].

Parameter	A1	A2	Parameter	A1	A2
A_e, cm^2	30.29	30.29	l_t, cm	5.78	5.78
A_t, cm^2	27.81	27.81	l_1, cm	5.54	4.74
A_e/A_t	1.09	1.09	l_2, cm	0.24	1.04
h_e, cm	1.49	1.49	l_3, cm	0.01	0.06
h_i, cm	3.52	3.52	l_4, cm	5.76	5.72
h_t, cm	1.37	1.37	M_d	1.35	1.35
h_1, cm	1.41	1.57	NPR_d	2.97	2.97
h_2, cm	1.37	1.37	R_c, cm	0.68	2.74
l, cm	11.56	11.56	θ, degrees	20.84	22.33
l_e, cm	5.78	5.78	α, degrees	1.21	1.21

The nozzle performance code was used to generate computational results for both configuration A1 and A2. Figures 4.2 and 4.3 provide a comparison of the computational code results and the experimental results of Mason, Putnam, and Re [16] for configuration A1 and A2, respectively.

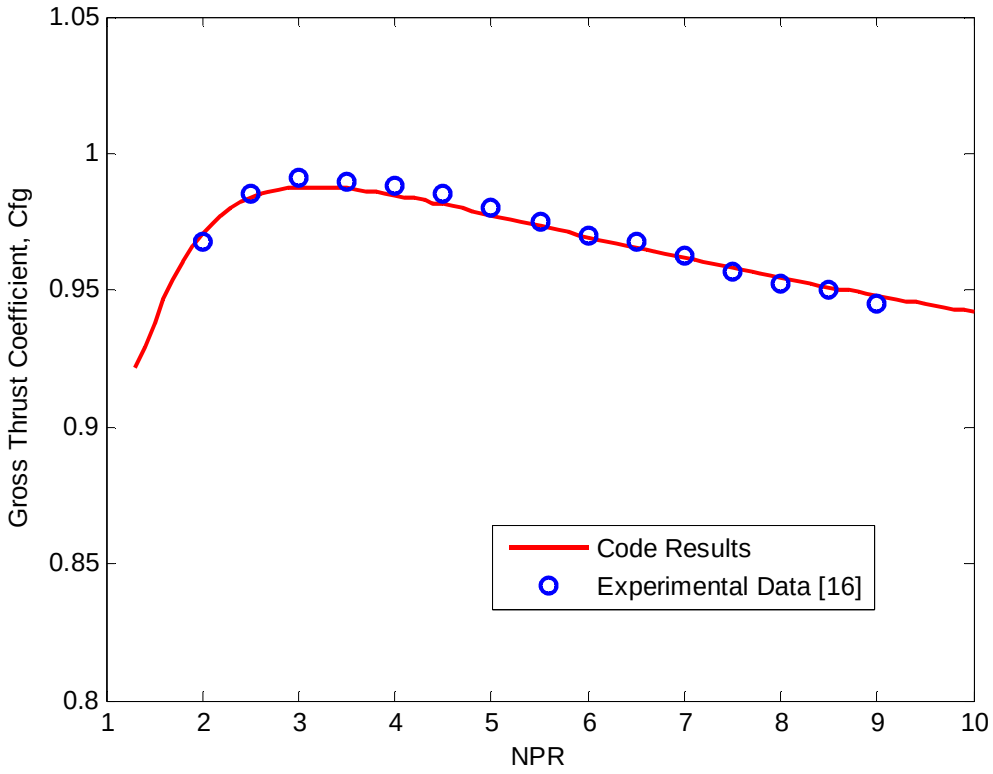

Figure 4.2 Experimental and computational gross thrust coefficient results for nozzle configuration A1.

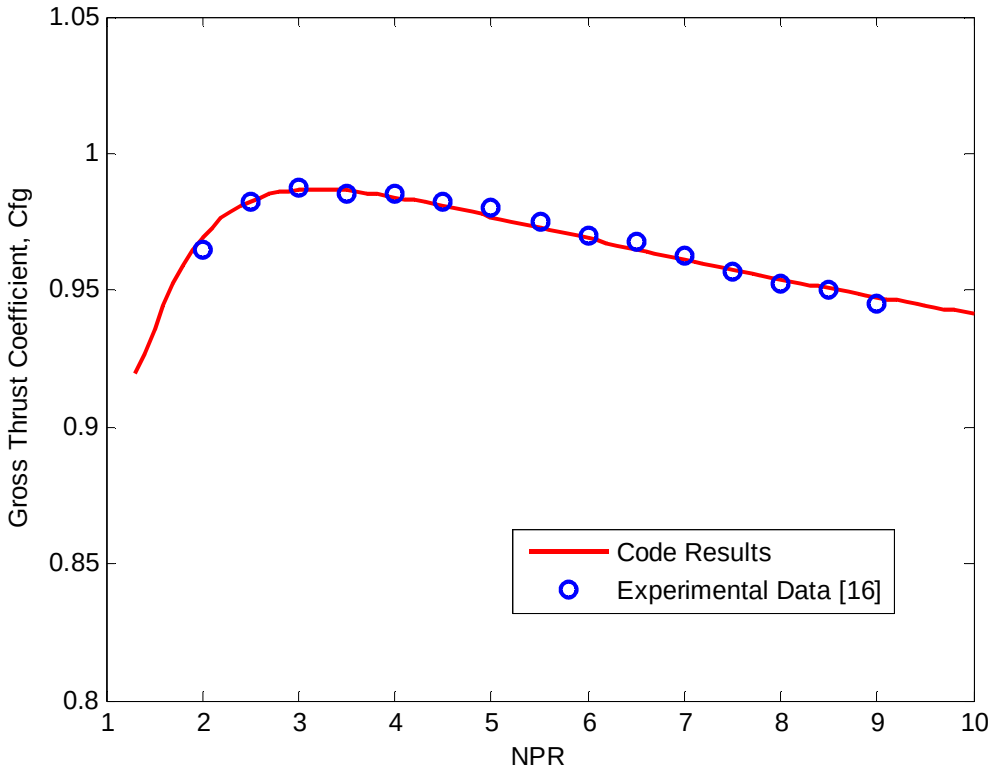

Figure 4.3 Experimental and computational gross thrust coefficient results for nozzle configuration A2.

One can see in Figures 4.2 and 4.3 that the shapes of the computational and experimental curves are identical with the peak of each occurring at a nozzle pressure ratio of 2.97. The nozzle performance code provides an almost exact prediction of the experimental results over the entire nozzle pressure ratio range with a maximum error of 0.3% for nozzle configuration A1 and 0.35% for nozzle configuration A2. As shown, the gross thrust prediction agrees with the experimental data to within the precision of the measurement system (approximately 0.5%).

Mason, Putnam, and Re [16] used the performance prediction code of Cline [21] to provide a comparison to their experimental data. The theory of Cline [21] applies the two-dimensional inviscid Euler equations to the calculation of internal nozzle flow for converging-diverging nozzle geometries. Shock effects are modeled using a procedure, termed "shock smearing", which incorporates an explicit artificial viscosity. Mason, Putnam, and Re [16] used the prediction code of Cline [21] to generate results over a NPR range of 3-9 for each nozzle configuration included in their analysis.

Figure 4.4 provides a comparison of the nozzle performance prediction code results to both the computational results of Cline [21] and the experimental results of Mason, Putnam and Re [16] for nozzle A1. One can see that both the nozzle performance prediction code and Cline's [21] prediction code provide results that compare extremely well with the experimental data over an NPR range of 3-9.

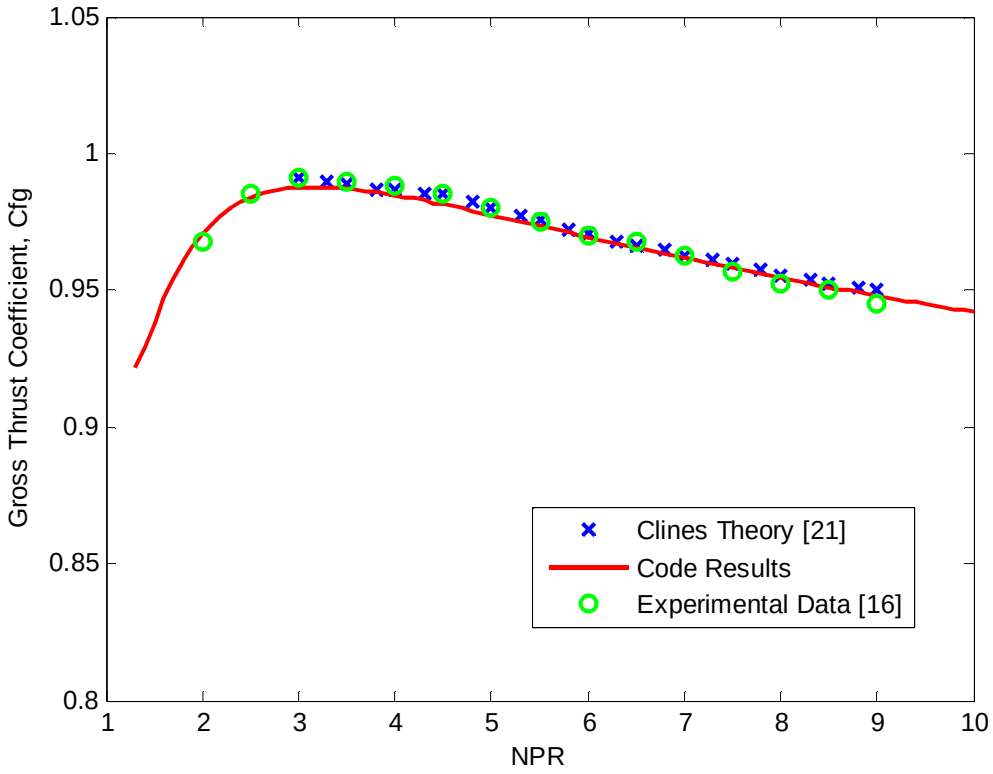

Figure 4.4 Cline's [21] theory comparison for nozzle A1.

Figure 4.5 provides a comparison of the nozzle performance prediction code results to both the computational results of Cline [21] and the experimental results of Mason, Putnam and Re [16] for nozzle A2. One can see that the nozzle performance prediction code provides results that compare extremely well with the experimental data over the entire NPR range while the computational results of Cline [21] continuously overpredict the experimental data over the NPR range of 3-9.

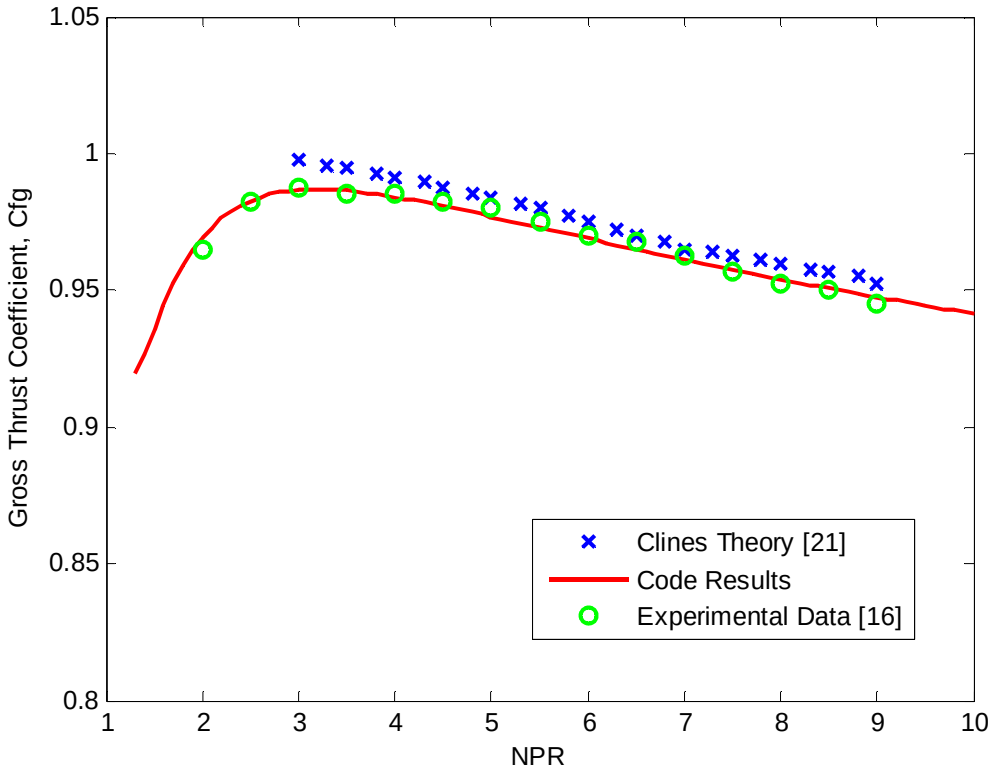

Figure 4.5 Cline's [21] theory comparison for nozzle A2.

For nozzle geometry A1, the program determined the angularity coefficient, C_A, to be 0.9999, the velocity coefficient, C_V, to be 0.9878, and the discharge coefficient, C_d, to be 0.9896.

For nozzle geometry A2, the program determined the angularity coefficient, C_A, to be 0.9999, the velocity coefficient, C_V, to be 0.9869, and the discharge coefficient, C_d, to be 0.9888.

4.1.2 Configurations B1, B2, and B3

The nozzle geometry of B1, B2, and B3 is shown in Figure 4.6. A table listing the design parameters for each configuration is provided in Table 4.2 as well. Note that these geometries differ through their radii of curvature as well as both their primary and secondary nozzle half angles.

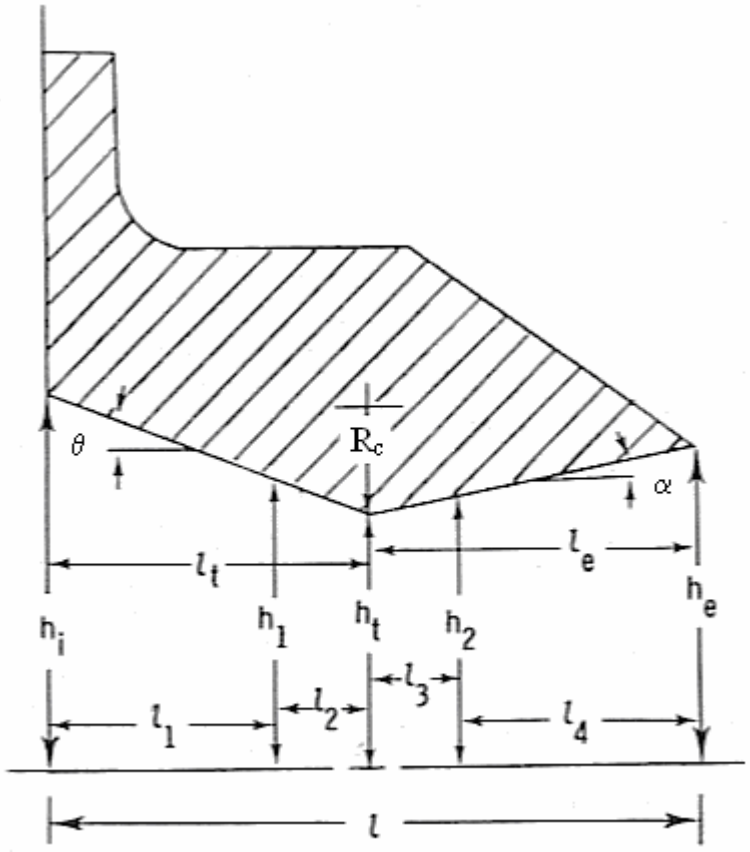

Figure 4.6 Nozzle geometry for configurations B1, B2 and B3 [16].

Table 4.2 Nozzle design parameters for configurations B1, B2, and B3 [16].

Parameter	B1	B2	B3	Parameter	B1	B2	B3
A_e, cm^2	50.06	50.06	50.06	l_t, cm	5.78	5.78	6.27
A_t, cm^2	27.81	27.81	27.81	l_1, cm	5.54	4.74	5.32
A_e/A_t	1.8	1.8	1.8	l_2, cm	0.24	1.04	0.96
h_e, cm	2.46	2.46	2.46	l_3, cm	0.13	0.53	0.52
h_i, cm	3.52	3.52	3.52	l_4, cm	5.65	5.25	5.46
h_t, cm	1.37	1.37	1.37	M_d	2.08	2.08	2.08
h_1, cm	1.41	1.57	1.54	NPR_d	8.81	8.81	8.81
h_2, cm	1.38	1.42	1.42	R_c, cm	0.68	2.74	2.74
l, cm	11.56	11.56	12.25	θ, degrees	20.84	22.33	20.42
l_e, cm	5.78	5.78	5.97	α, degrees	10.85	11.24	10.85

The nozzle internal performance code was used to generate computational results for configurations B1, B2 and B3. Figures 4.7, 4.8, and 4.9 provide a comparison of the computational code results and the experimental results of Mason, Putnam, and Re [16] for configuration B1, B2, and B3, respectively.

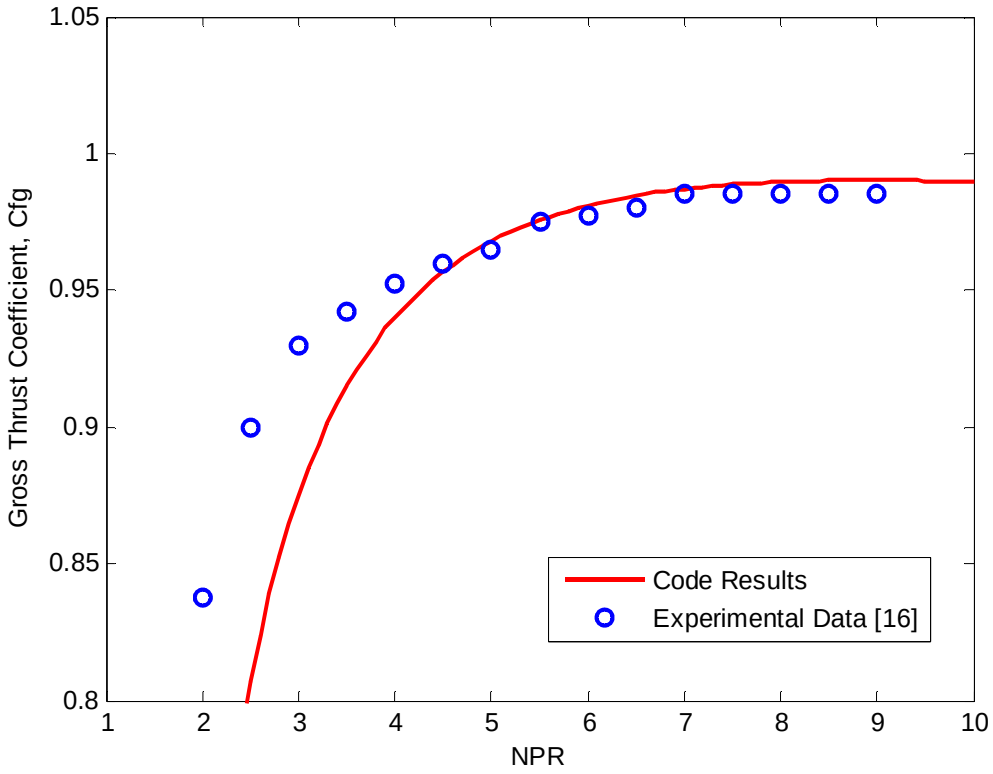

Figure 4.7 Experimental and computational gross thrust coefficient results for nozzle configuration B1.

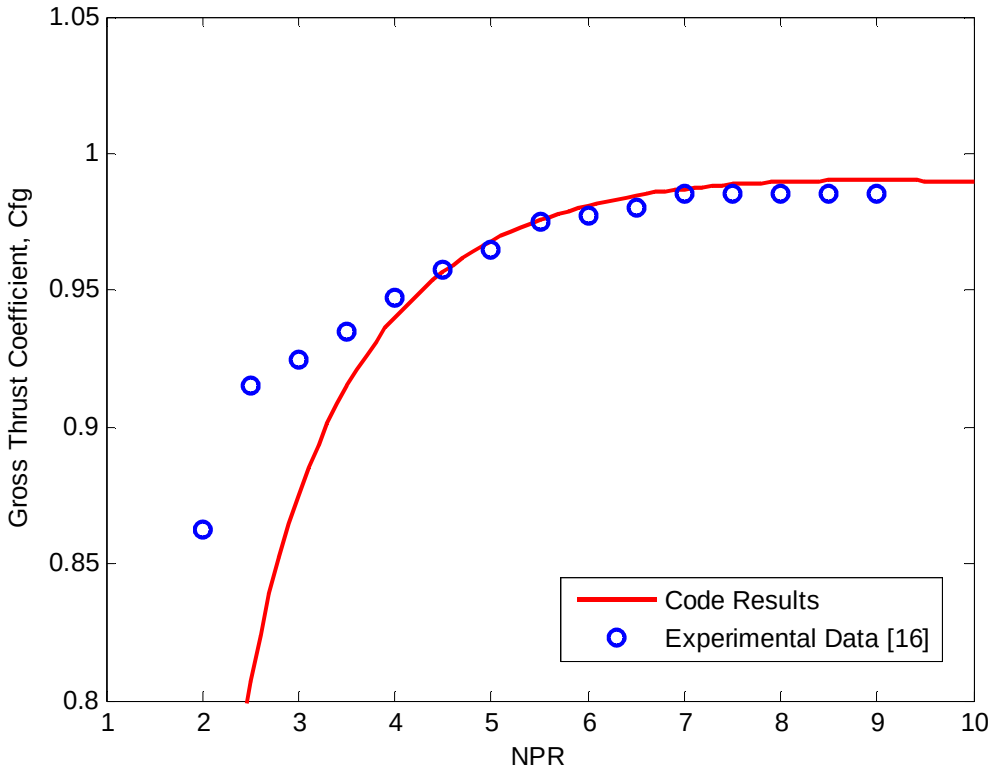

Figure 4.8 Experimental and computational gross thrust coefficient results for nozzle configuration B2.

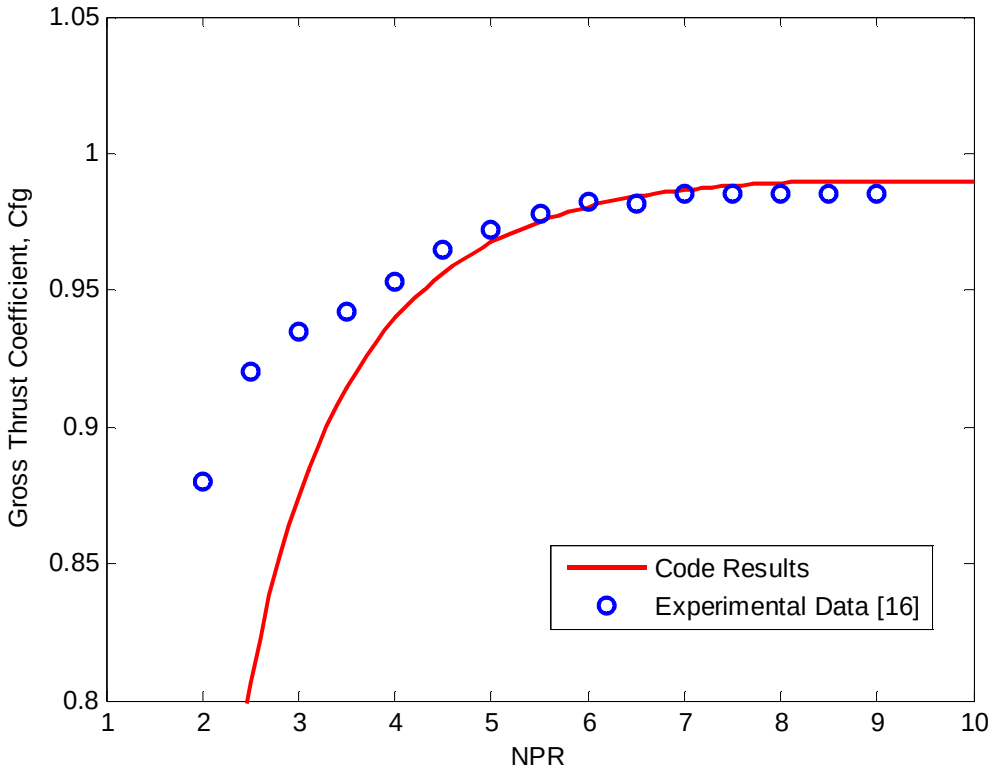

Figure 4.9 Experimental and computational gross thrust coefficient results for nozzle configuration B3.

As can be seen in Figures 4.7, 4.8, and 4.9, the shapes of the computational and experimental curves are identical with the peak of each occurring at a nozzle pressure ratio of 8.81. The code results for nozzle pressure ratios above 4.5 predict the gross thrust coefficient to within 0.42% of the experimental data. At nozzle pressure ratios below 4.5, however, the code underpredicts the experimental results by up to 12%.

In their analysis, Mason, Putnam, and Re [16] state that the internal flow separates at lower nozzle pressure ratios for nozzles with high divergence angles as seen in the geometries of nozzles B1, B2, and B3. This flow separation, a result of overexpansion,

causes an increase in the thrust efficiency as shown by the experimental results for an NPR range of 2-4.5. Overexpansion occurs because the expansion ratio of the nozzle is too large for full expansion to be sustained for a given nozzle pressure ratio. Thus, the nozzle adjusts to a smaller, more suitable expansion ratio causing an increase in thrust efficiency as shown in Figure 4.10. The increase in thrust efficiency, depicted in Figure 4.10, is the result of the natural inclination of an overexpanded fluid to reach a more effective balance between momentum and energy. This results in a more efficient expansion and improved transfer of total pressure and temperature into momentum and thrust.

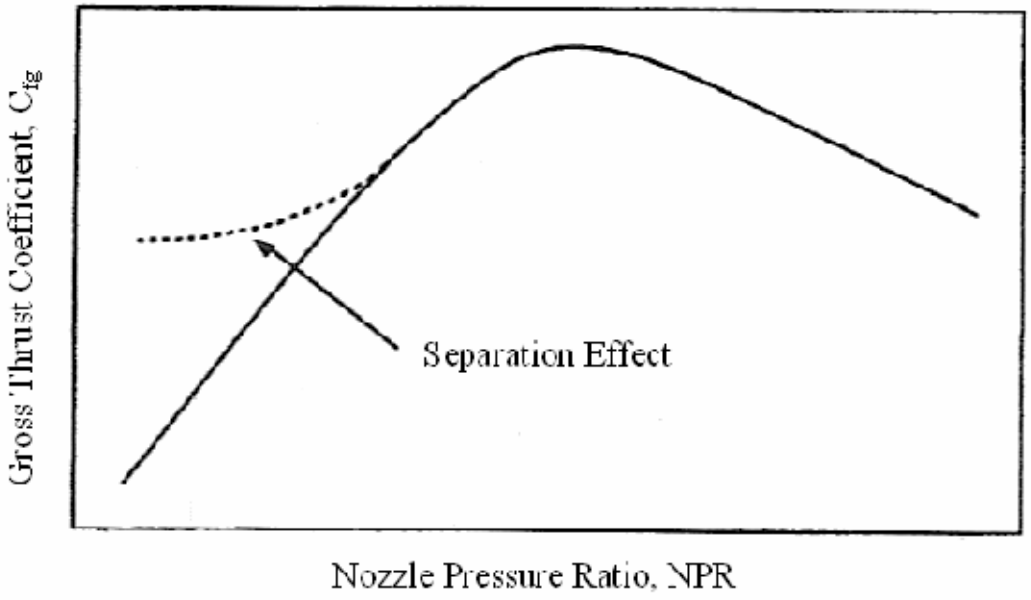

Figure 4.10 The effect of separation on thrust performance [20].

Above a NPR of 4.5, separation does not occur and thus the nozzle was performing as predicted by the nozzle performance code. As shown in Figures 4.7, 4.8, and 4.9, the gross thrust prediction agrees with the experimental data, until the point of separation, to within the precision of the measurement system (approximately 0.5%).

Figure 4.11 provides a comparison of the nozzle performance prediction code results to both the computational results of Cline [21] and the experimental results of Mason, Putnam and Re [16] for nozzle B1. One can see that both the nozzle performance prediction code and Cline's [21] prediction code provide results that compare extremely well with the experimental data until the experimental results show signs of separation at a NPR of 4.5.

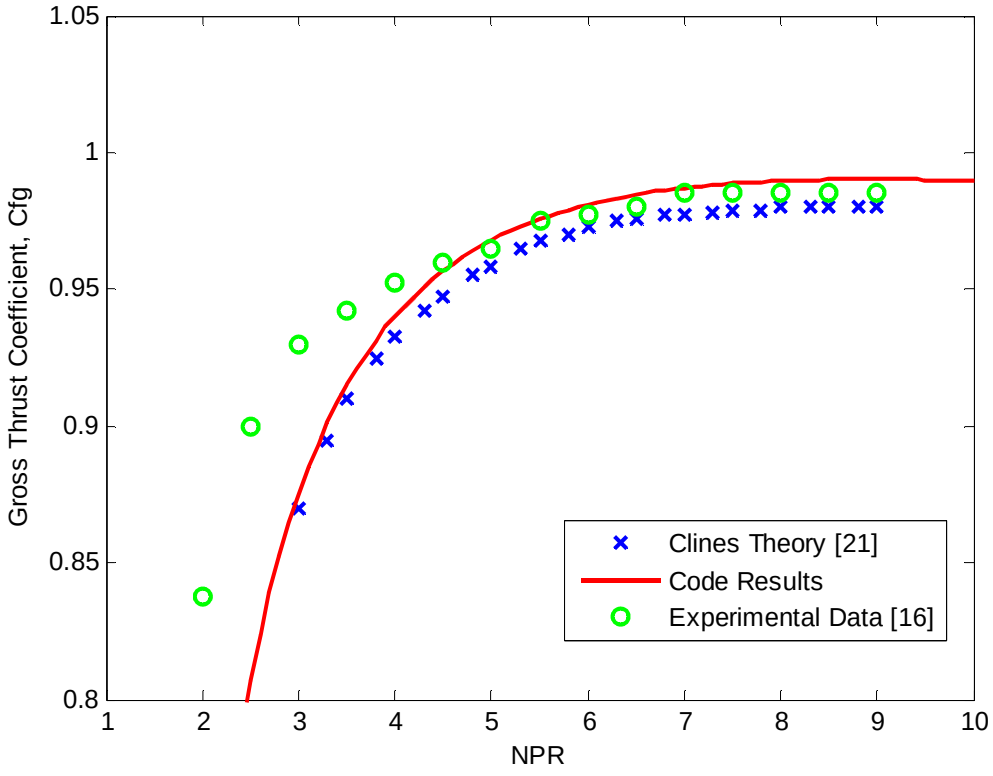

Figure 4.11 Cline's [21] theory comparison for nozzle B1.

Figure 4.12 provides a comparison of the nozzle performance prediction code results to both the computational results of Cline [21] and the experimental results of Mason, Putnam and Re [16] for nozzle B2. One can see that the nozzle performance prediction code provides results that compare extremely well with the experimental data until the experimental results show signs of separation at a NPR of 4.5. The computational results of Cline [21], however, continuously overpredict the experimental data over the NPR range of 4.5-9.

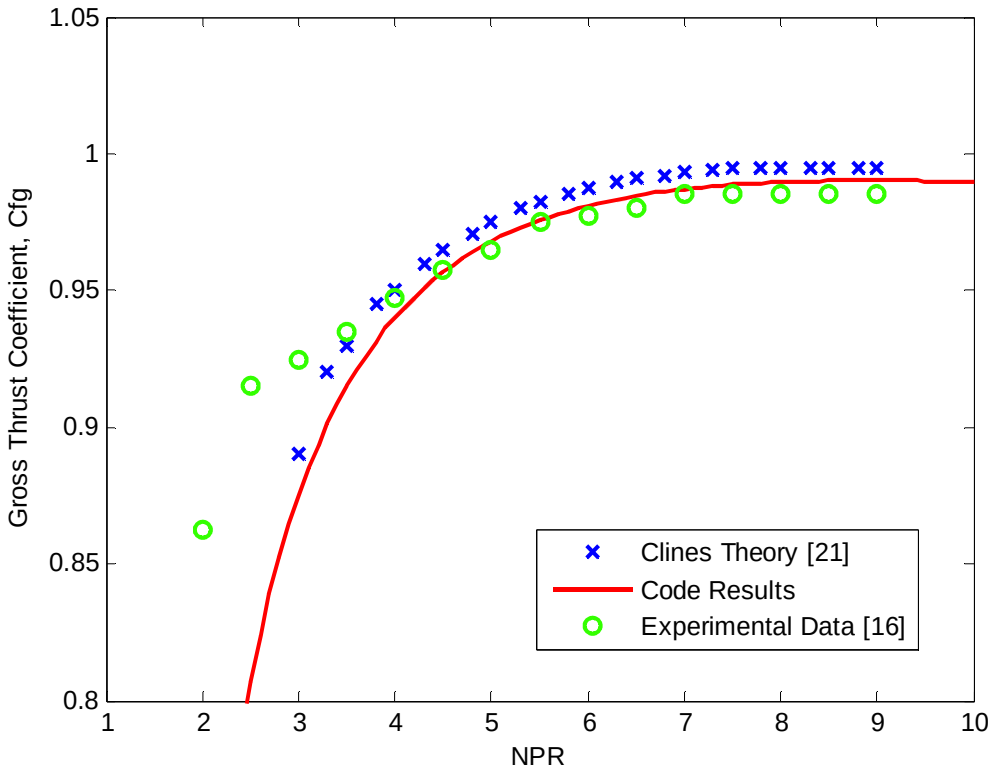

Figure 4.12 Cline's [21] theory comparison for nozzle B2.

Figure 4.13 provides a comparison of the nozzle performance prediction code results to both the computational results of Cline [21] and the experimental results of Mason, Putnam and Re [16] for nozzle B3. One can see that both the nozzle performance prediction code and Cline's [21] prediction code provide results that compare extremely well with the experimental data until the experimental results show signs of separation at a NPR of 4.5.

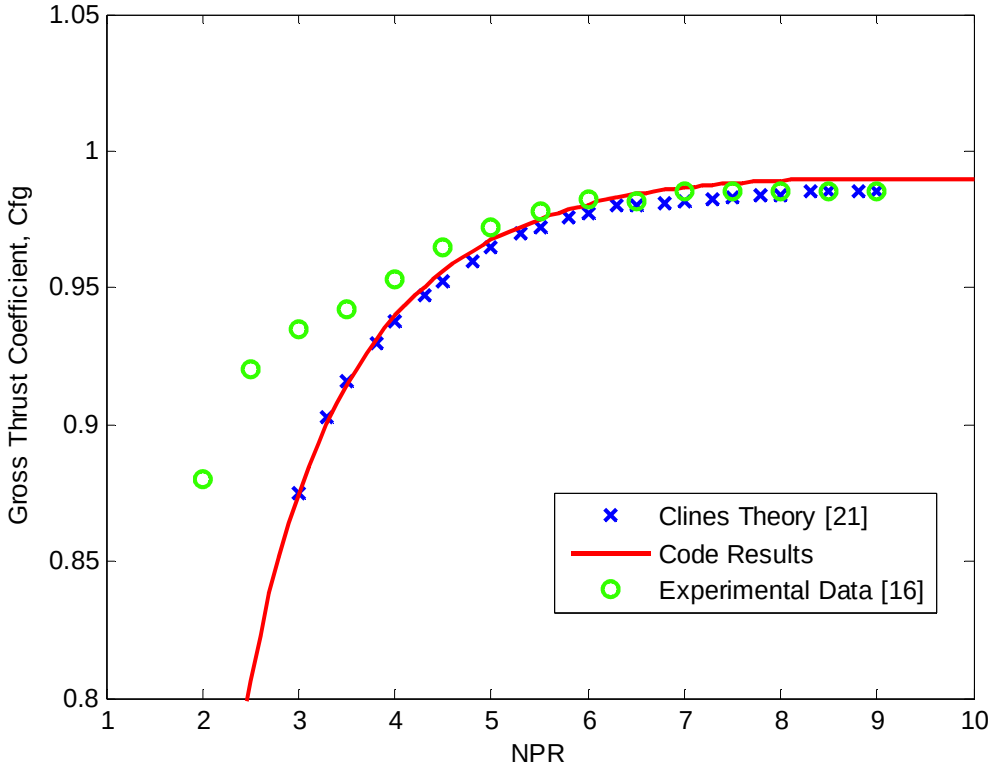

Figure 4.13 Cline's [21] theory comparison for nozzle B3.

For nozzle geometry B1, the program determined the angularity coefficient, C_A, to be 0.9932, the velocity coefficient, C_V, to be 0.997, and the discharge coefficient, C_d, to be 0.9932.

For nozzle geometry B2, the program determined the angularity coefficient, C_A, to be 0.993, the velocity coefficient, C_V, to be 0.9968, and the discharge coefficient, C_d, to be 0.9896.

For nozzle geometry B3, the program determined the angularity coefficient, C_A, to be 0.993, the velocity coefficient, C_V, to be 0.9968, and the discharge coefficient, C_d, to be 0.9896.

4.2 The Experiment of Berrier and Re [17]

Berrier and Re [17] conducted a test program investigating the effects of several geometric parameters on nozzle performance. They examined several non-axisymmetric nozzles including a converging-diverging nozzle, a single ramp expansion nozzle and a wedge nozzle. These three nozzle concepts were tested in the static test facility of the Langley 16 foot transonic tunnel and recorded internal performance data at nozzle pressure ratios up to 10.0.

The geometry of the nonaxisymmetric converging diverging nozzle used in their investigation is provided in Figure 4.14. As shown, this nozzle has a throat area of 4.3262 in^2, an expansion ratio of 1.25, a divergence angle of 5.38°, and a design NPR of 4.22.

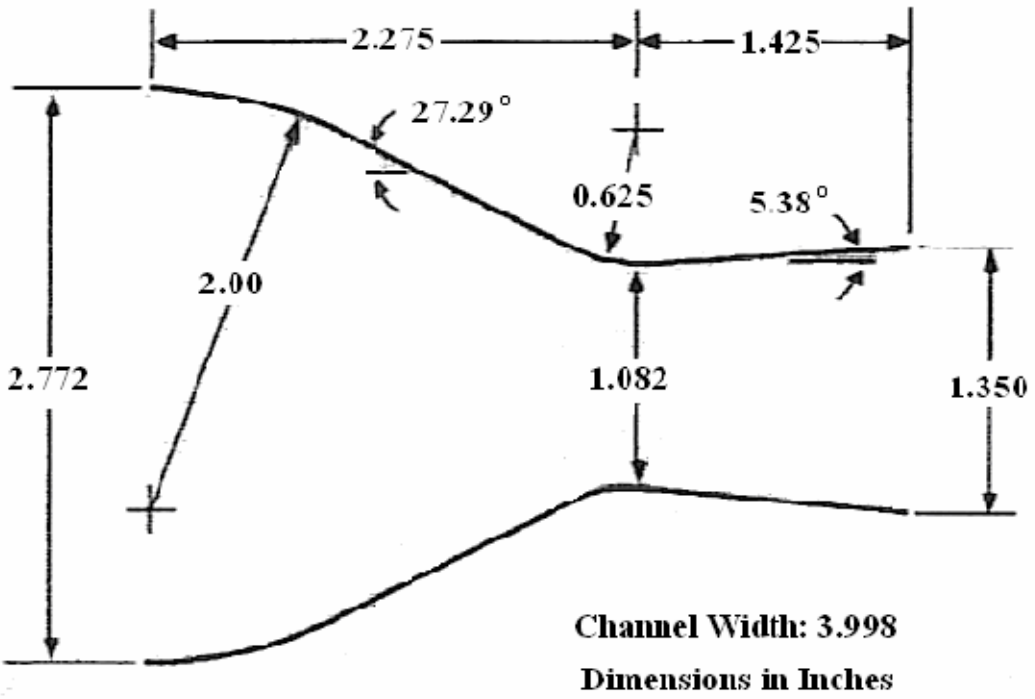

Figure 4.14 Nozzle geometry [20].

The nozzle performance code was used to obtain computational results for this nozzle geometry. Figure 4.15 provides a comparison of the computational code results and the experimental results of Berrier and Re [17] for this nozzle.

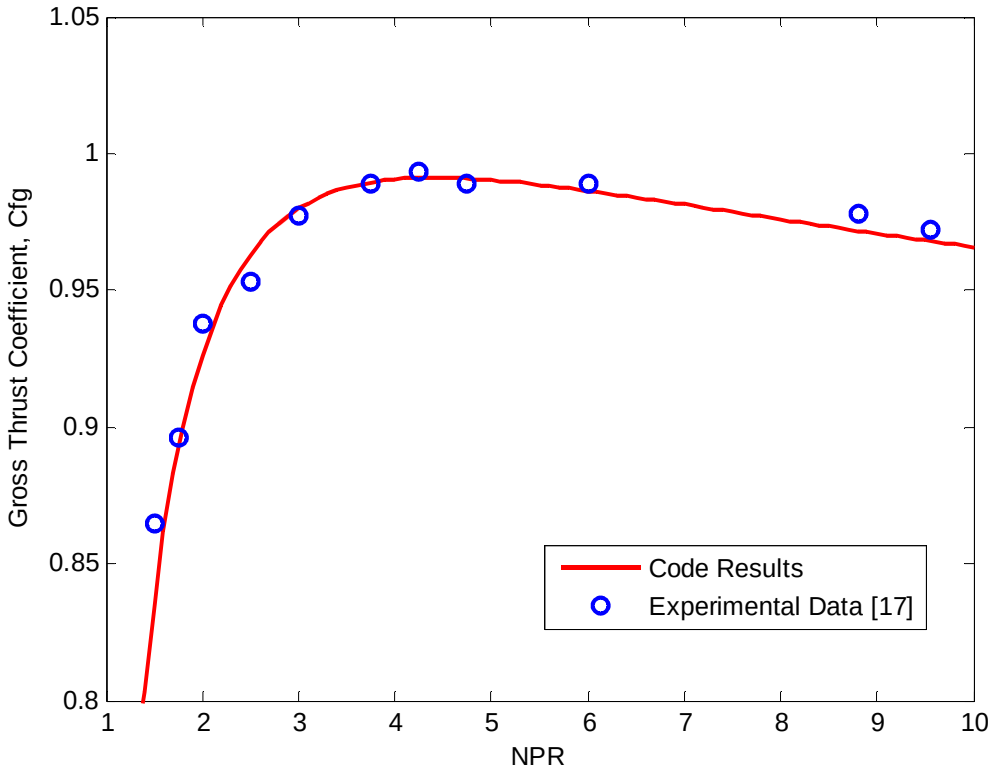

Figure 4.15 Experimental and computational gross thrust coefficient results for the nozzle of Berrier and Re [17].

As can be seen Figure 4.15, the shapes of the computational and experimental curves are identical with the peak of each occurring at a nozzle pressure ratio of 4.25. The code results show excellent agreement with the experimental results of Berrier and Re [17] over the entire nozzle pressure range considered. As shown, the gross thrust prediction agrees with the experimental data to within the precision of the measurement system (approximately 0.5%).

Hunter [20] developed an analytical/numerical method, known as the nozzle performance analysis code (NPAC), to predict the thrust performance of non-

axisymmetric two-dimensional convergent divergent nozzles. The theory of NPAC includes losses due to thermodynamic nozzle performance effects, boundary layer development and skin friction losses, and effects due to angularity. One-dimensional flow theory was used to model the thermodynamic nozzle performance effects due to both overexpansion and underexpansion while an approximate integral momentum method based on the Karman-Polhausen solution was used to calculate boundary layer development and skin friction losses.

Figure 4.16 provides a comparison of the nozzle performance prediction code results to both the computational results of NPAC and the experimental results of Berrier and Re [17]. One can see that both the nozzle performance prediction code and NPAC provide results that compare extremely well with the experimental data over the entire NPR range.

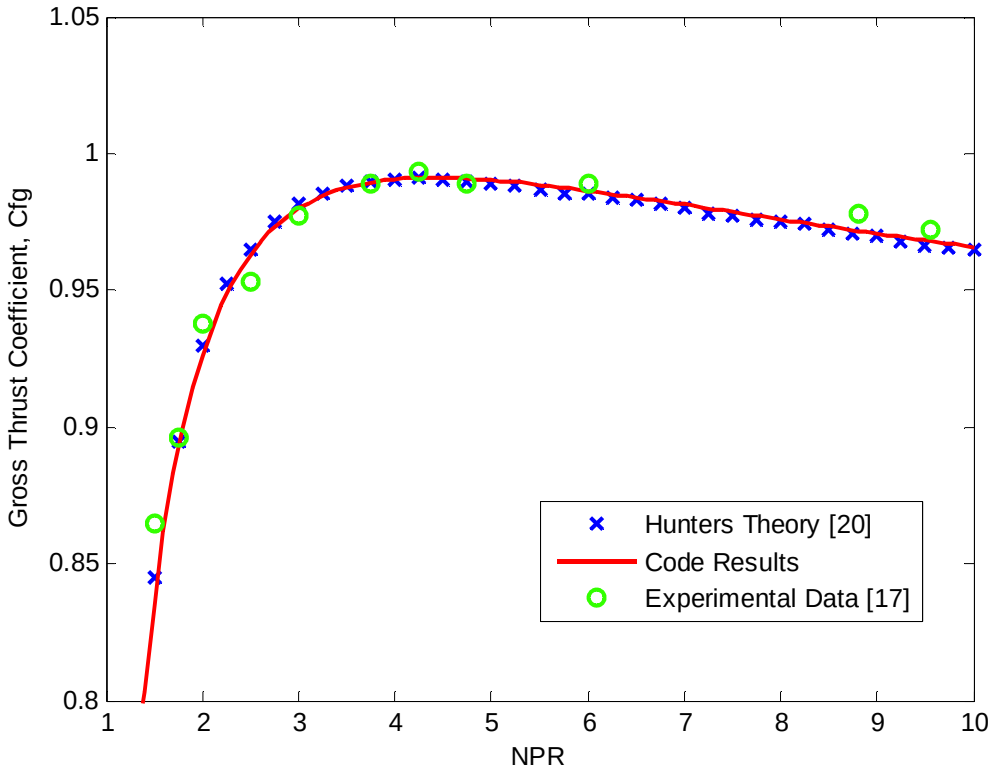

Figure 4.16 Hunter's theory comparison for the nozzle of Berrier and Re [17].

For this nozzle geometry, the program determined the angularity coefficient, C_A, to be 0.9979, the velocity coefficient, C_V, to be 0.9932, and the discharge coefficient, C_d, to be 0.9894.

4.3 The Experiment of Hunter [18]

This nozzle was used as part of a test program investigating passive shock – boundary layer interaction control concepts. The experimental results for this nozzle were generated by Hunter [18]. The nozzle geometry is provided in Figure 4.17. As shown, this nozzle has a throat area of 4.3172 in^2, an expansion ratio of 1.797, a divergence angle of 11.01°, and a design NPR of 8.78.

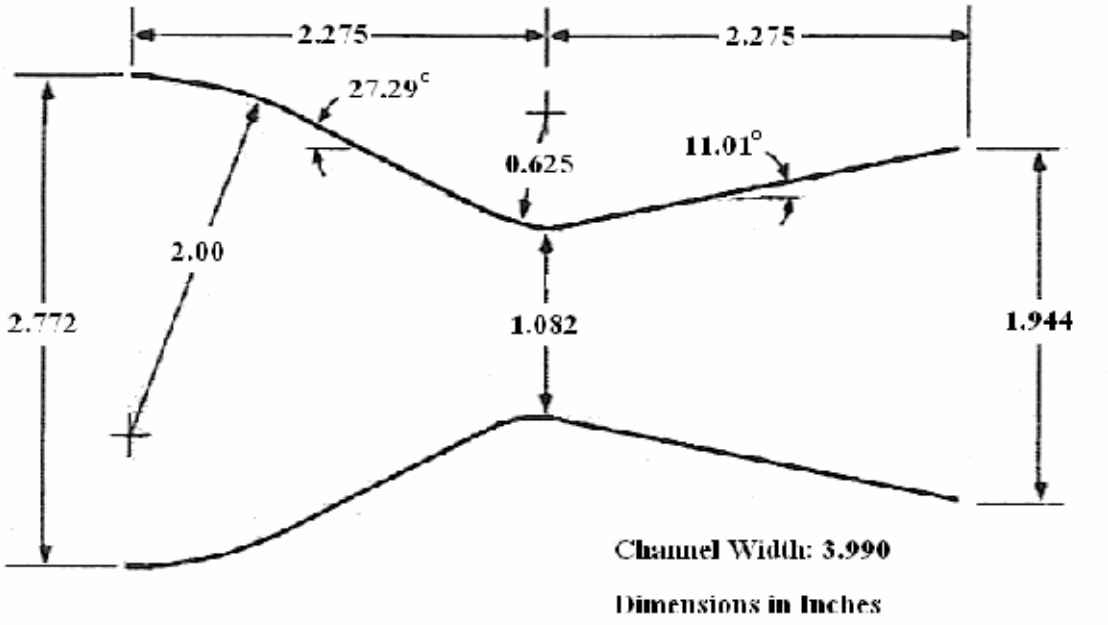

Figure 4.17 Nozzle geometry [20].

The nozzle performance code was used to obtain computational results for this nozzle geometry. Figure 4.18 provides a comparison of the computational code results and the experimental results of Hunter [18].

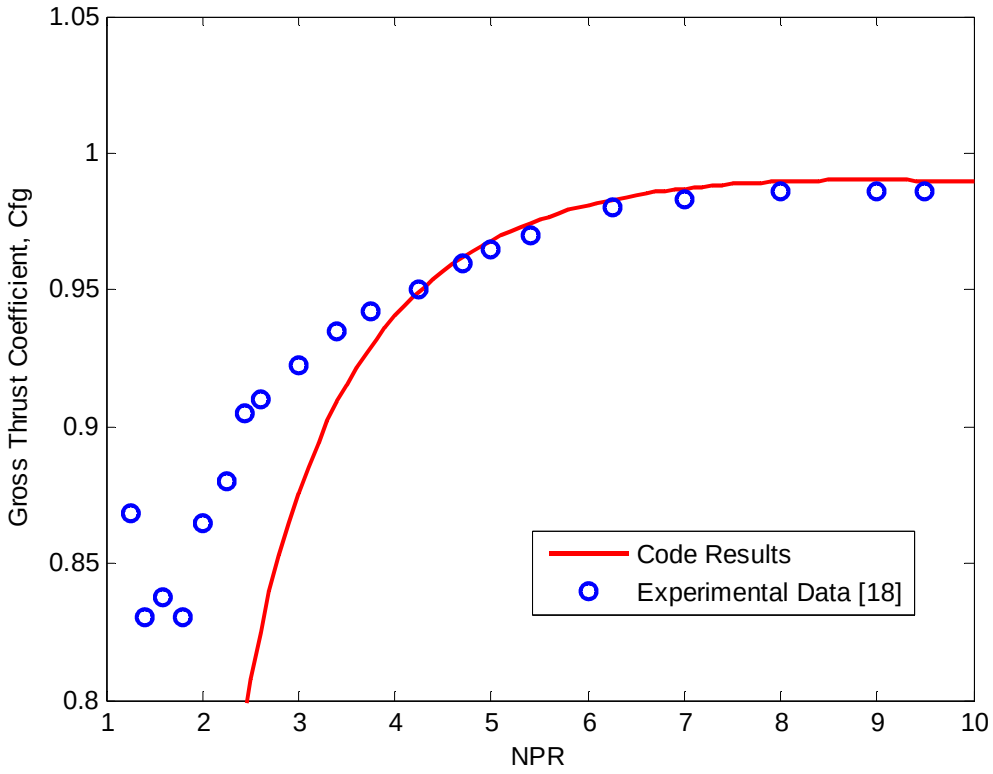

Figure 4.18 Experimental and computational gross thrust coefficient results for the nozzle of Hunter [18].

As can be seen in Figure 4.18, the shapes of the computational and experimental curves are identical with the peak of each occurring at a nozzle pressure ratio of 8.78. The code results for nozzle pressure ratios above 3.75 predict the gross thrust coefficient to within 0.3% of the experimental data. At nozzle pressure ratios below 3.75, however, the code underpredicts the experimental results by up to 20%.

In his analysis, Hunter [18] states that the experimental off-design internal pressure data for this nozzle configuration shows strong evidence of shock induced separation in the divergent section of the nozzle for an NPR range of 1.8 to 5.0. As stated

before in section 4.1.2, this flow separation causes an increase in the thrust efficiency as depicted in Figure 4.18 over the NPR range of 1.25 to 4. This explains the underprediction of the gross thrust coefficient over this NPR range. Above an NPR of 5, the nozzle was shock free, and thus the code successfully predicts its performance. As shown, the gross thrust prediction agrees with the experimental data, until the point of separation, to within the precision of the measurement system (approximately 0.5%).

Figure 4.19 provides a comparison of the nozzle performance prediction code results to both the computational results of NPAC and the experimental results of Hunter [20]. One can see that both the nozzle performance prediction code and NPAC provide results that compare extremely well with the experimental data until the experimental results show signs of separation at a NPR of 4.

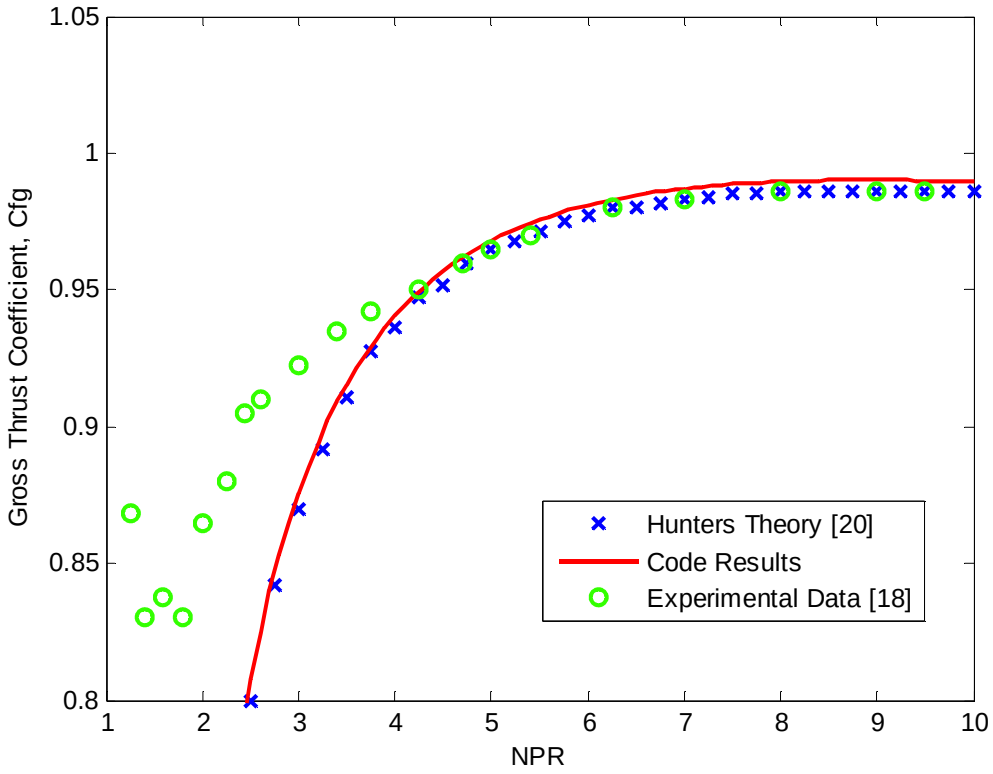

Figure 4.19 Hunter's theory comparison for the nozzle of Hunter [18].

For this nozzle geometry, the program determined the angularity coefficient, C_A, to be 0.9932, the velocity coefficient, C_V, to be 0.9969, and the discharge coefficient, C_d, to be 0.9898.

4.4 The Experiment of Capone and Berrier [19]

This nozzle geometry was tested by Capone and Berrier [19] as part of a wind tunnel experiment on a 1/10 scale, twin engine F-18 prototype aircraft model. The nozzle geometry is provided in Figure 4.20. As shown, this nozzle has a sharp cornered throat[12], a throat area of 2.5 in^2, an expansion ratio of 1.15, a divergence angle of 1.54°, and a design NPR of 3.46.

It should be noted that this nozzle geometry consists of a cutback outside sidewall as well as an extended nozzle inter-fairing on the inside sidewall. Thus, in actuality, this nozzle is not two-dimensional along its entire length. The geometry shown in Figure 4.20 does not depict the sidewall variations.

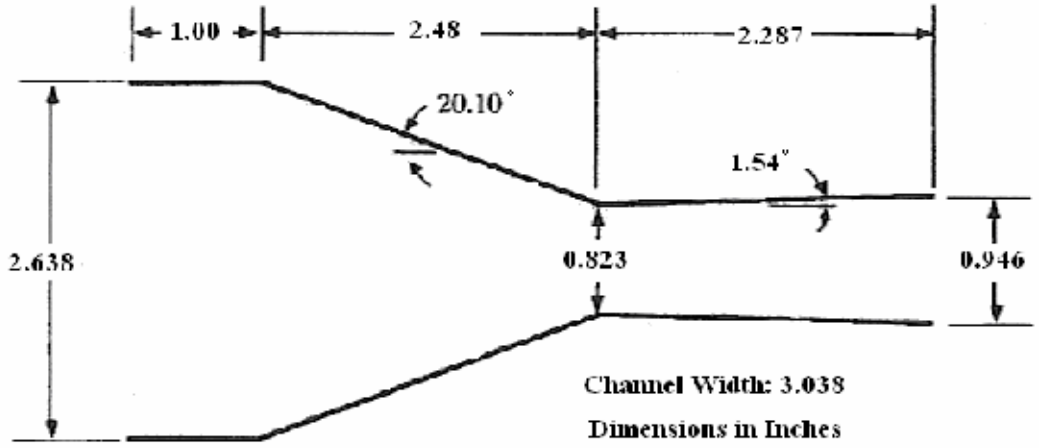

Figure 4.20 Nozzle geometry [20].

[12] For this nozzle geometry, the radius of curvature was entered as 0.00001 inches.

The nozzle performance code was used to obtain computational results for this nozzle geometry. Figure 4.21 provides a comparison of the computational code results and the experimental results of Capone and Berrier [19].

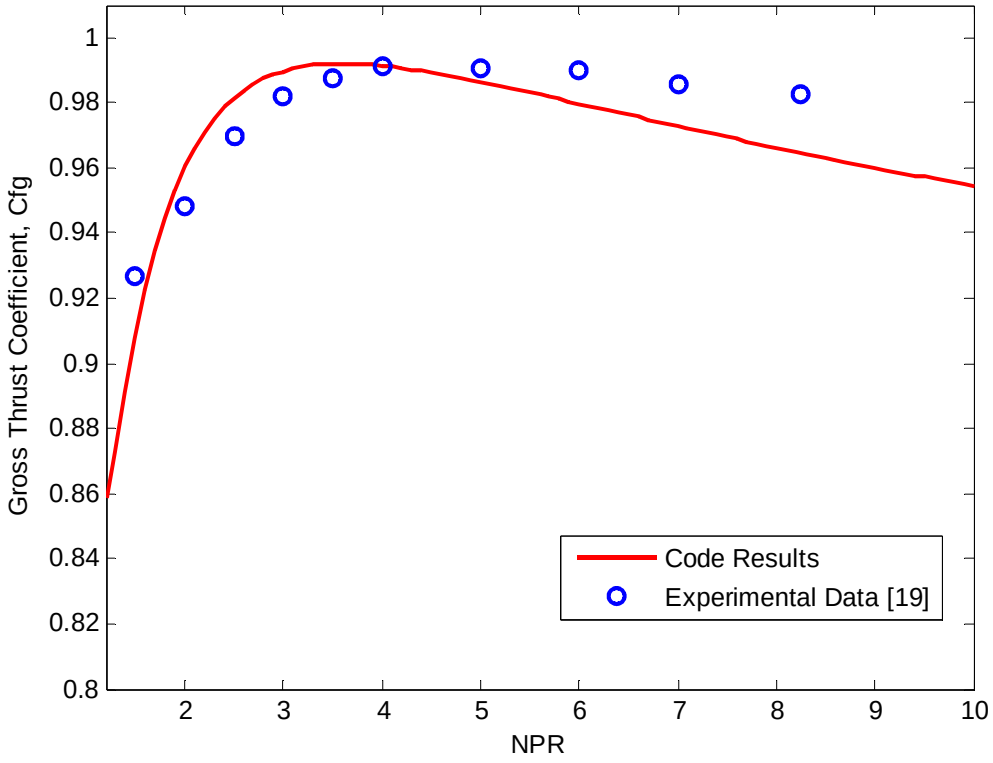

Figure 4.21 Experimental and computational gross thrust coefficient results for the nozzle of Capone and Berrier [19].

As can be seen in Figure 4.21, the shapes of the computational and experimental curves are not identical with peak gross thrust coefficients occurring at different nozzle pressure ratios. The computational curve peaks at an NPR of 3.5 while the experimental curve peaks at an NPR of 4. The code results also overpredict the experimental results up to an NPR of 5 and underpredict the experimental results for NPRs above 5. At nozzle

pressure ratios less than 5.0, the difference between the computational and experimental results is at most 1.2%. For nozzle pressure ratios above 5.0, however, the difference is at most as 1.8%.

Some of the discrepancies existing between the computational and experimental results are believed to be linked to the cutback outside sidewall geometry. The outside sidewall cutback increases the effective nozzle expansion ratio thus causing the experimental peak gross thrust performance to occur at a higher NPR.

Figure 4.22 provides a comparison of the nozzle performance prediction code results to both the computational results of NPAC and the experimental results of Capone and Berrier [19]. One can see that both the nozzle performance prediction code and NPAC provide results that compare well with the experimental data over the lower NPR range of 1-5. At nozzle pressure ratios above 5, both computational methods underpredict the experimental data by up to 1.8%. This is believed to be linked to the cutback outside sidewall geometry causing the nozzle to not be two-dimensional along its entire length

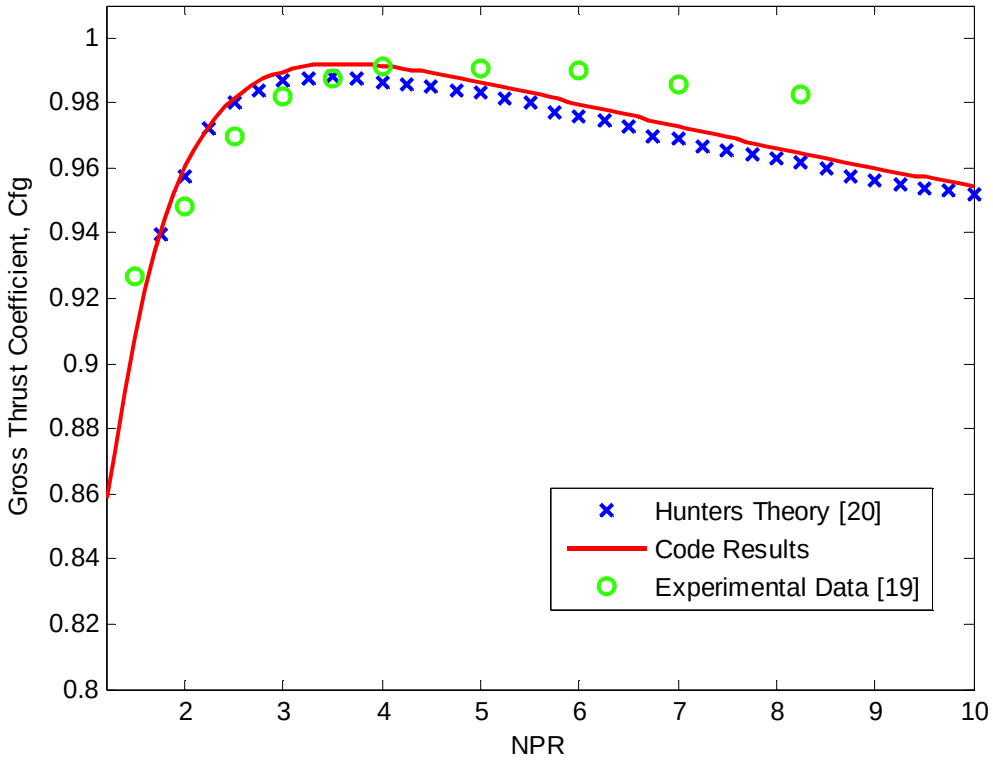

Figure 4.22 Hunter's theory comparison for the nozzle of Capone and Berrier [19].

For this nozzle geometry, the program determined the angularity coefficient, C_A, to be 0.9998, the velocity coefficient, C_V, to be 0.9925, and the discharge coefficient, C_d, to be 0.9914.

For each nozzle considered in this study, the nozzle performance prediction code consistently performs as well as, and in some cases better than, the codes developed by Cline [21] and Hunter [20]. This confirms that this prediction code is a valid and useful tool for predicting the gross thrust performance for non-axisymmetric two dimensional converging diverging exhaust nozzles.

5. Conclusions and Recommendations

This paper describes the creation of a computational code that can be used to predict the thrust performance characteristics of non-axisymmetric two-dimensional convergent-divergent exhaust nozzles. The code includes the effects of friction, angularity, and expansion losses on the overall nozzle efficiency. To demonstrate the validity of the nozzle performance prediction code, the generated computational results were compared to experimental data as well as the computational results of existing performance codes for a number of different nozzle geometries. Important conclusions are as follows:

(1) The nozzle internal performance prediction code showed excellent agreement with experimental data in predicting the peak gross thrust coefficients for basic 2D-CD nozzle geometries (7 out of the 8 cases to within 0.6 percent).

(2) The computational results for low expansion ratio nozzles with shallow divergence angles showed excellent agreement with experimental data over the entire NPR range. Differences between the predicted gross thrust efficiency and experimental data were generally less than 0.6%.

(3) For high expansion ratio nozzles with steep divergence angles, the nozzle internal performance prediction code results matched experimental data almost exactly for higher nozzle pressure ratios. For the lower NPR regime, where the experimental data showed evidence of flow separation, the code results underpredicted the experimental by up to 10%.

(4) The nozzle performance prediction code cannot accurately predict nozzle thrust performance for nozzles that are not truly two-dimensional along their entire length because of cutback outside sidewalls.

A few important points can be derived from these conclusions. For one, this nozzle performance prediction model accurately predicts the gross thrust performance of non-axisymmetric two-dimensional converging diverging nozzles. Secondly, while this model cannot account for separation effects, it is still applicable for underexpanded, externally overexpanded, and design NPR's. This prediction model can become invaluable when used to interpret experimental data, to understand the fluid mechanics and loss effects represented in the prediction code, to provide insight into the fundamentals of nozzle thrust performance, or just to understand why a particular nozzle operates as it does.

A couple of recommendations can be made as based on these conclusions. For one, the current model cannot account for separation effects. As such, it would be invaluable if a flow separation model could be added to the current code. Secondly, this prediction model could easily be expanded to include other nozzle geometries, particularly axisymmetric converging diverging nozzles which are of interest to the Air Force Research Laboratory. Expansion of this prediction model to include axisymmetric converging diverging nozzles would only require modification to the current method of characteristics subroutine (from two dimensions to three dimensions).

Appendix A: Preliminary Results

A number of researchers – Mason, Putnam, and Re [16], Berrier and Re [17], Hunter [18], and Cappone and Berrier [19] - have conducted experiments on a variety of nozzle geometries to understand the effect of various parameters on nozzle gross thrust coefficient. The experimental results of these researchers are used to validate the theory of the nozzle internal performance code.

1.0 The Experiment of Mason, Putnam, and Re [16]

Mason, Putnam, and Re [16] conducted an experiment to determine the effect of throat contouring on nozzle internal performance. They tested five non-axisymmetric converging-diverging nozzles in the static test facility of the Langley 16 foot transonic tunnel and recorded internal performance data at nozzle pressure ratios up to 9.0.

For their experiment, two CD nozzles, A1 and B1, were used as baseline nozzle geometries. These baseline geometries were modified by increasing the throat radius of curvature while holding all other geometric parameters constant except for the primary nozzle half angle, θ, and the secondary nozzle half angle, ε. The modified nozzle geometries are labeled as A2, B2, and B3. The two baseline geometries as well as the modified geometries were tested and the data from each recorded.

1.1 Configuration A1 and A2

The nozzle geometry of A1 and A2 is shown in Figure A1. A table listing the design parameters for each configuration is provided in Table A1 as well. Note that these two geometries differ through their radii of curvature and primary nozzle half angles.

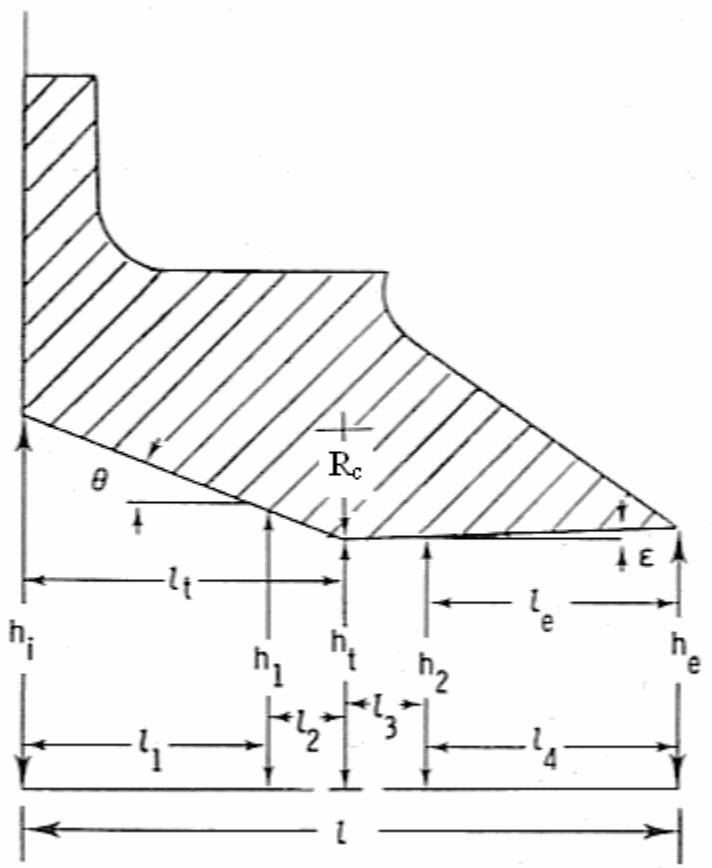

Figure A1 Nozzle geometry for configurations A1 and A2 [16].

Table A1 Nozzle design parameters for configurations A1 and A2 [16].

Parameter	A1	A2	Parameter	A1	A2
A_e, cm^2	30.29	30.29	l_t, cm	5.78	5.78
A_t, cm^2	27.81	27.81	l_1, cm	5.54	4.74
A_e/A_t	1.09	1.09	l_2, cm	0.24	1.04
h_e, cm	1.49	1.49	l_3, cm	0.01	0.06
h_i, cm	3.52	3.52	l_4, cm	5.76	5.72
h_t, cm	1.37	1.37	M_d	1.35	1.35
h_1, cm	1.41	1.57	NPR_d	2.97	2.97
h_2, cm	1.37	1.37	R_c, cm	0.68	2.74
l, cm	11.56	11.56	θ, degrees	20.84	22.33
l_e, cm	5.78	5.78	ε, degrees	1.21	1.21

The nozzle performance code was used to generate computational results for both configuration A1 and A2. Figures A2 and A3 provide a comparison of the computational code results and the experimental results of Mason, Putnam, and Re [16] for configuration A1 and A2, respectively.

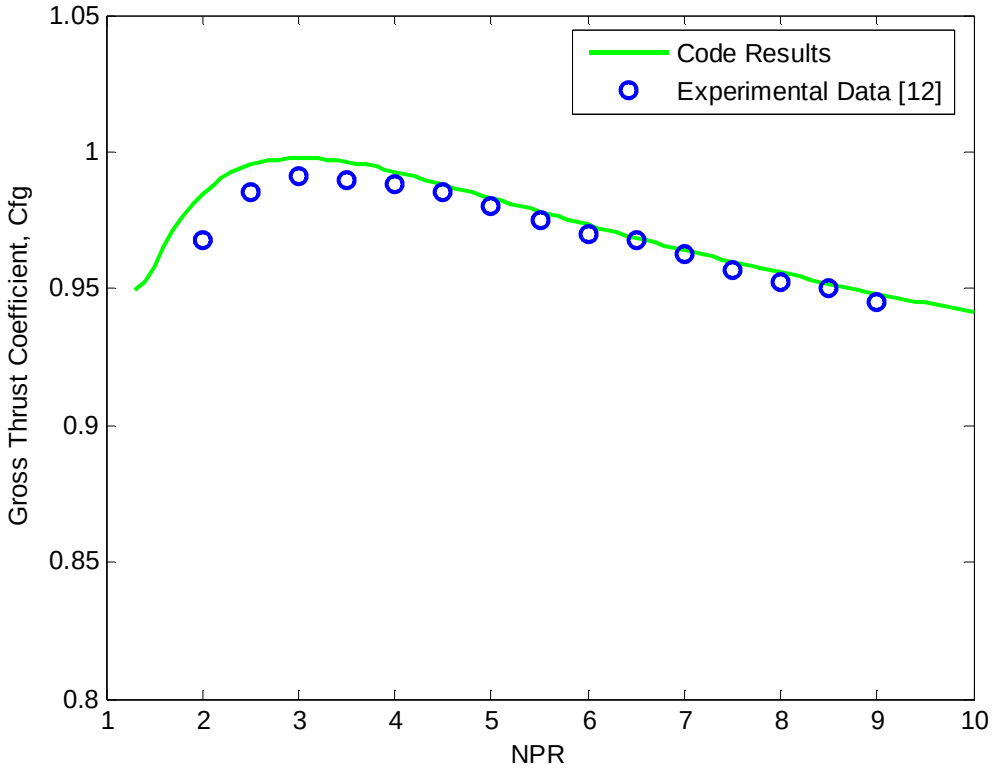

Figure A2 Experimental and computational gross thrust coefficient results for nozzle configuration A1.

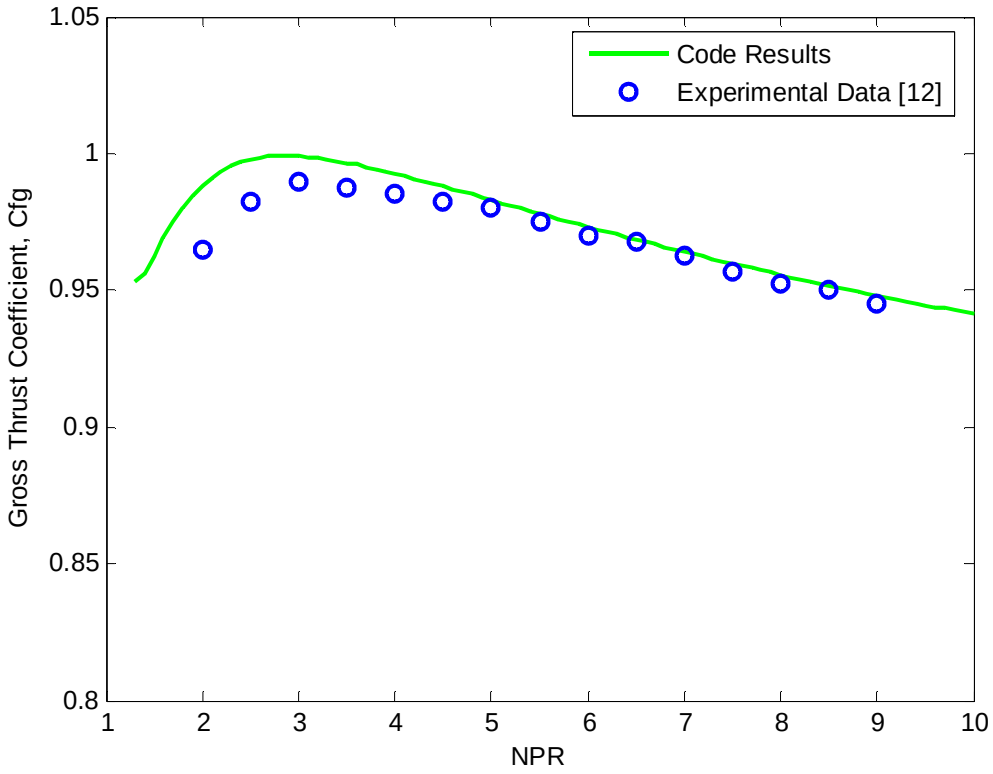

Figure A3 Experimental and computational gross thrust coefficient results for nozzle configuration A2.

One can see in each Figures A2 and A3 that the shapes of the computational and experimental curves are identical with the peak of each occurring at a nozzle pressure ratio of 2.97. At nozzle pressure ratios above 2.97, the theory provides an almost exact prediction of the experimental results while at lower pressure ratios, the code overpredicts the experimental data by approximately 1% for A1 and 1.6% for A2.

1.2 Configurations B1, B2, and B3

The nozzle geometry of B1, B2, and B3 is shown in Figure A4. A table listing the design parameters for each configuration is provided in Table A2 as well. Note that these geometries differ through their radii of curvature as well as both their primary and secondary nozzle half angles.

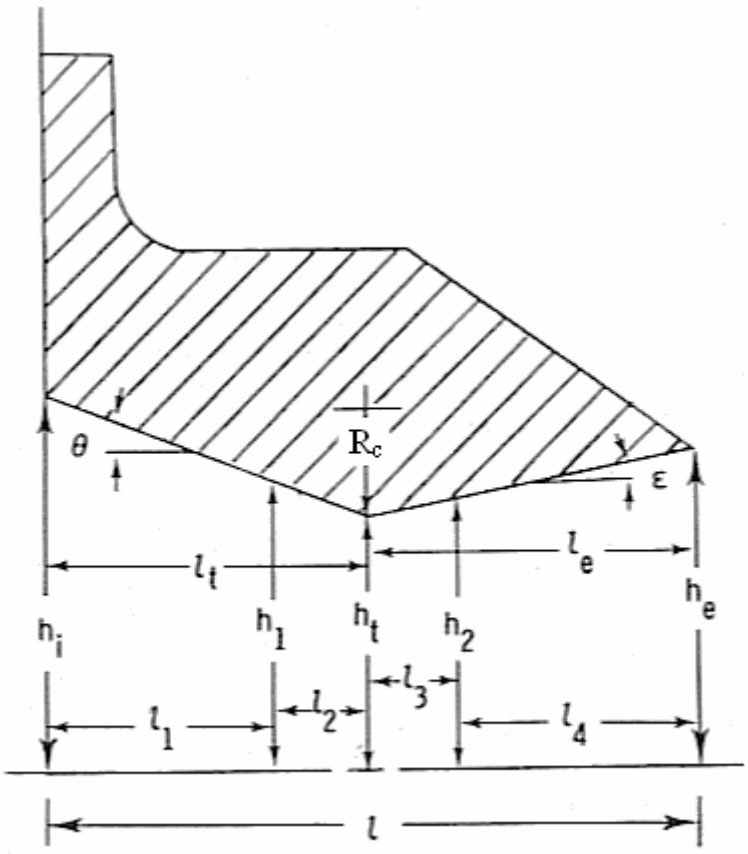

Figure A4 Nozzle geometry for configurations B1, B2 and B3 [16].

Table A2 Nozzle design parameters for configurations B1, B2, and B3 [16].

Parameter	B1	B2	B3	Parameter	B1	B2	B3
A_e, cm^2	50.06	50.06	50.06	l_t, cm	5.78	5.78	6.27
A_t, cm^2	27.81	27.81	27.81	l_1, cm	5.54	4.74	5.32
A_e/A_t	1.8	1.8	1.8	l_2, cm	0.24	1.04	0.96
h_e, cm	2.46	2.46	2.46	l_3, cm	0.13	0.53	0.52
h_i, cm	3.52	3.52	3.52	l_4, cm	5.65	5.25	5.46
h_t, cm	1.37	1.37	1.37	M_d	2.08	2.08	2.08
h_1, cm	1.41	1.57	1.54	NPR_d	8.81	8.81	8.81
h_2, cm	1.38	1.42	1.42	R_c, cm	0.68	2.74	2.74
l, cm	11.56	11.56	12.25	θ, degrees	20.84	22.33	20.42
l_e, cm	5.78	5.78	5.97	ε, degrees	10.85	11.24	10.85

The nozzle internal performance code was used to generate computational results for configurations B1, B2 and B3. Figures A5, A6, and A7 provide a comparison of the computational code results and the experimental results of Mason, Putnam, and Re [16] for configuration B1, B2, and B3, respectively.

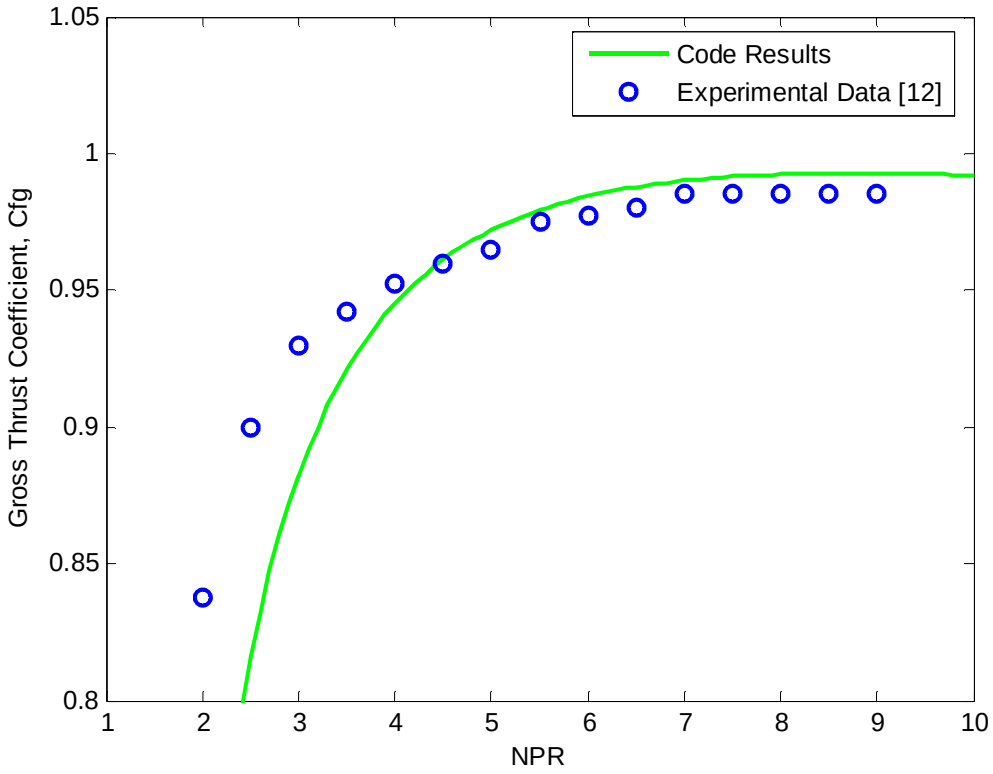

Figure A5 Experimental and computational gross thrust coefficient results for nozzle configuration B1.

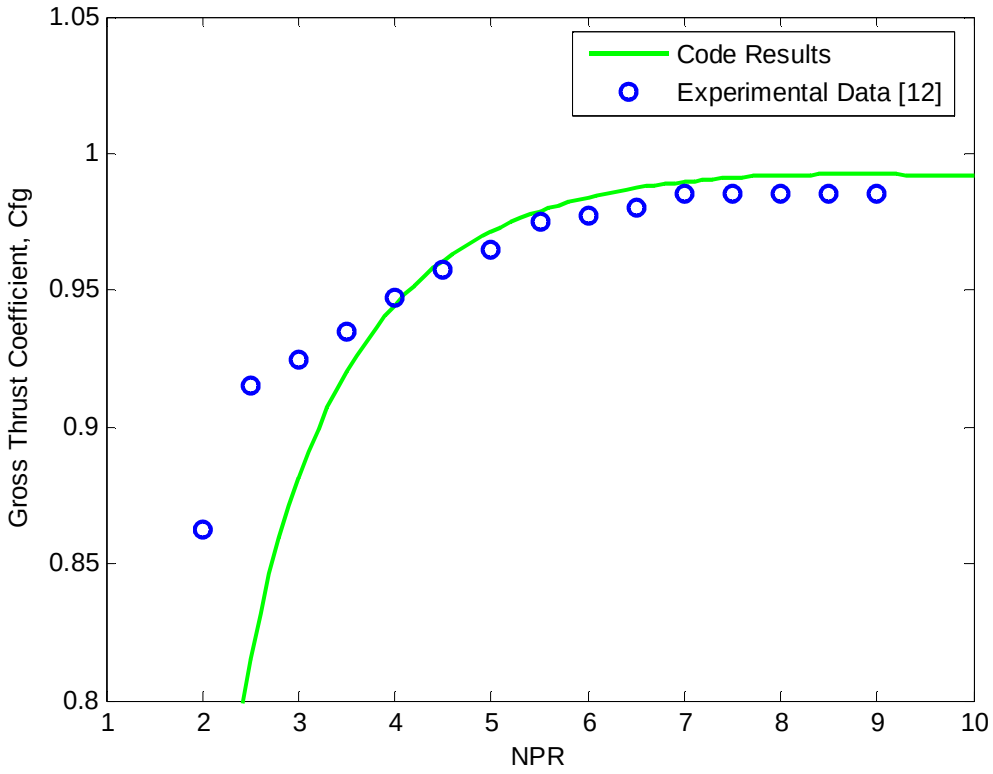

Figure A6 Experimental and computational gross thrust coefficient results for nozzle configuration B2.

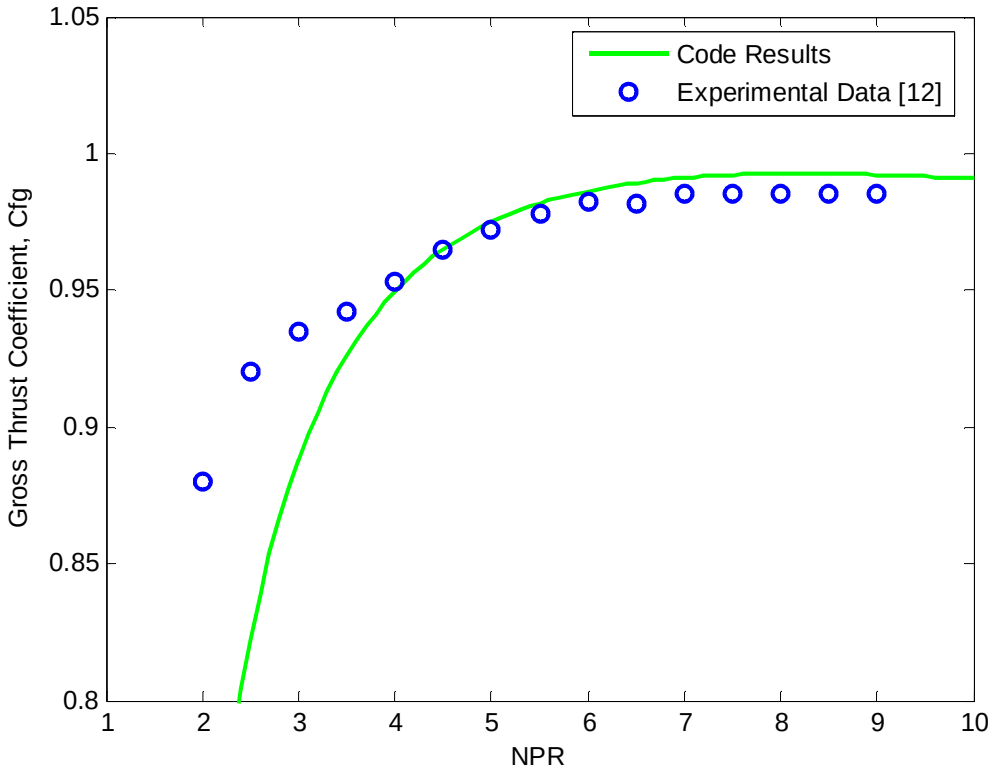

Figure A7 Experimental and computational gross thrust coefficient results for nozzle configuration B3.

As can be seen in each figure, the shapes of the computational and experimental curves are identical with the peak of each occurring at a nozzle pressure ratio of 8.81. The code results for nozzle pressure ratios above 4.0 predict the gross thrust coefficient to within 0.8% of the experimental data. At nozzle pressure ratios below 4.0, however, the code underpredicts the experimental results by up to 10%.

In their analysis, Mason, Putnam, and Re [16] state that the internal flow separates at lower nozzle pressure ratios for nozzles with high divergence angles as seen in the geometries of nozzles B1, B2, and B3. This flow separation, a result of

overexpansion, causes an increase in the thrust efficiency as shown by the experimental results for an NPR range of 2-4. Above a NPR of 4, separation does not occur and thus the nozzle was performing as predicted by the nozzle performance code.

2.0 The Experiment of Berrier and Re [17]

Berrier and Re [17] conducted a test program investigating the effects of several geometric parameters on nozzle performance. They examined several non-axisymmetric nozzles including a converging-diverging nozzle, a single ramp expansion nozzle and a wedge nozzle. These three nozzle concepts were tested in the static test facility of the Langley 16 foot transonic tunnel and recorded internal performance data at nozzle pressure ratios up to 10.0.

The geometry of the nonaxisymmetric converging diverging used in their investigation is provided in Figure A8. As shown, this nozzle has a throat area of 4.3262 in^2, an expansion ratio of 1.25, a divergence angle of 5.38°, and a design NPR of 4.22.

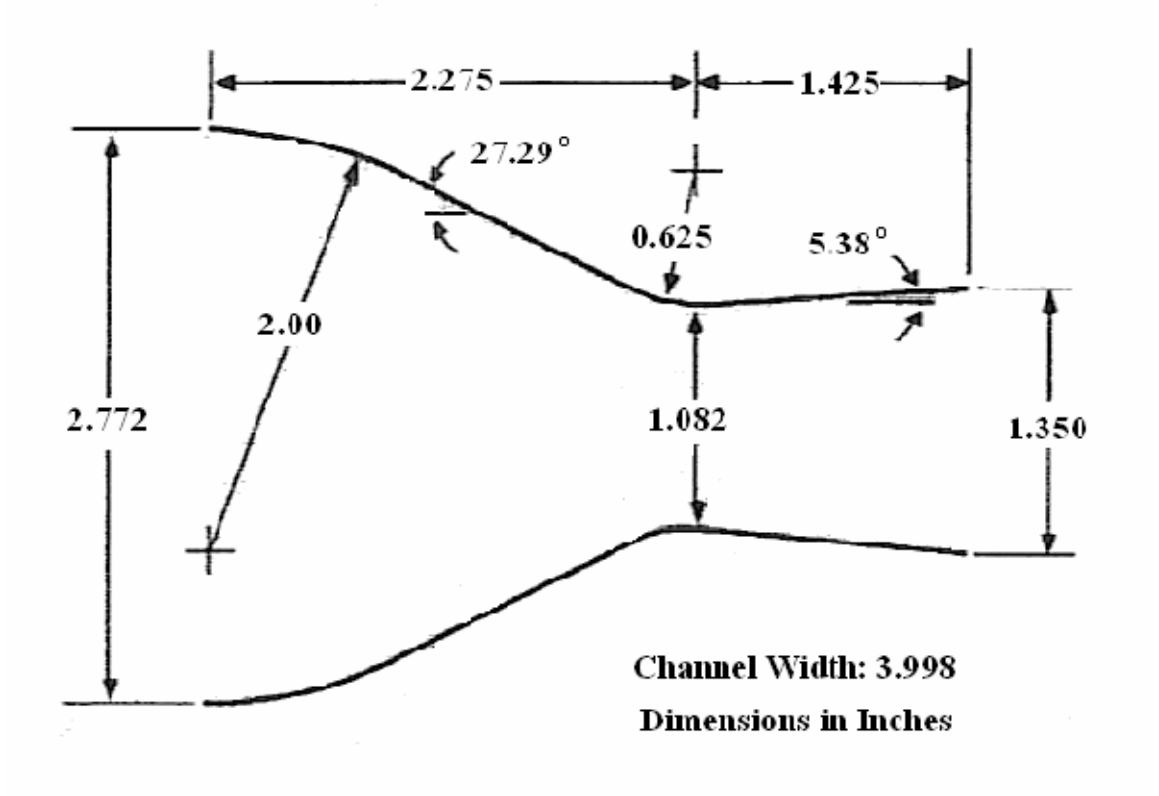

Figure A8: Nozzle geometry [20].

The nozzle performance code was used to obtain computational results for this nozzle geometry. Figure A9 provides a comparison of the computational code results and the experimental results of Berrier and Re [17] for this nozzle.

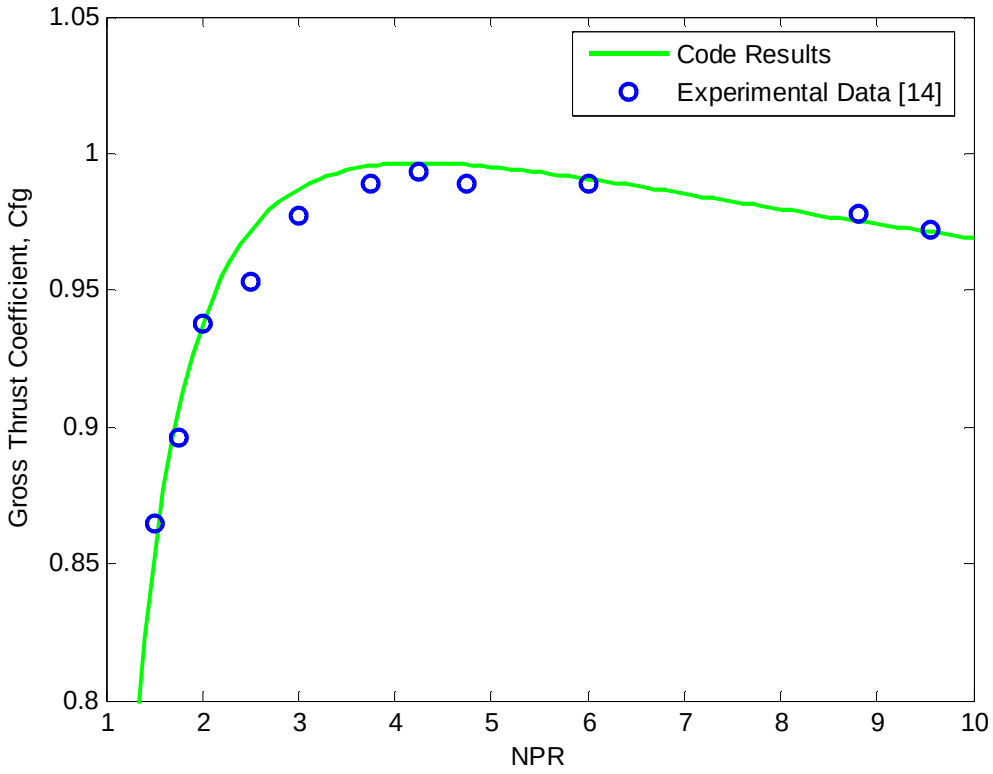

Figure A9 Experimental and computational gross thrust coefficient results for the nozzle of Berrier and Re [17].

As can be seen Figure A9, the shapes of the computational and experimental curves are identical with the peak of each occurring at a nozzle pressure ratio of 4.25. The code results show excellent agreement with the experimental results of Berrier and Re [17] over the entire nozzle pressure range shown.

3.0 The Experiment of Hunter [18]

This nozzle was used as part of a test program investigating passive shock – boundary layer interaction control concepts. The experimental results for this nozzle were generated by Hunter [18]. The nozzle geometry is provided in Figure A10. As shown, this nozzle has a throat area of 4.3172 in^2, an expansion ratio of 1.797, a divergence angle of 11.01°, and a design NPR of 8.78.

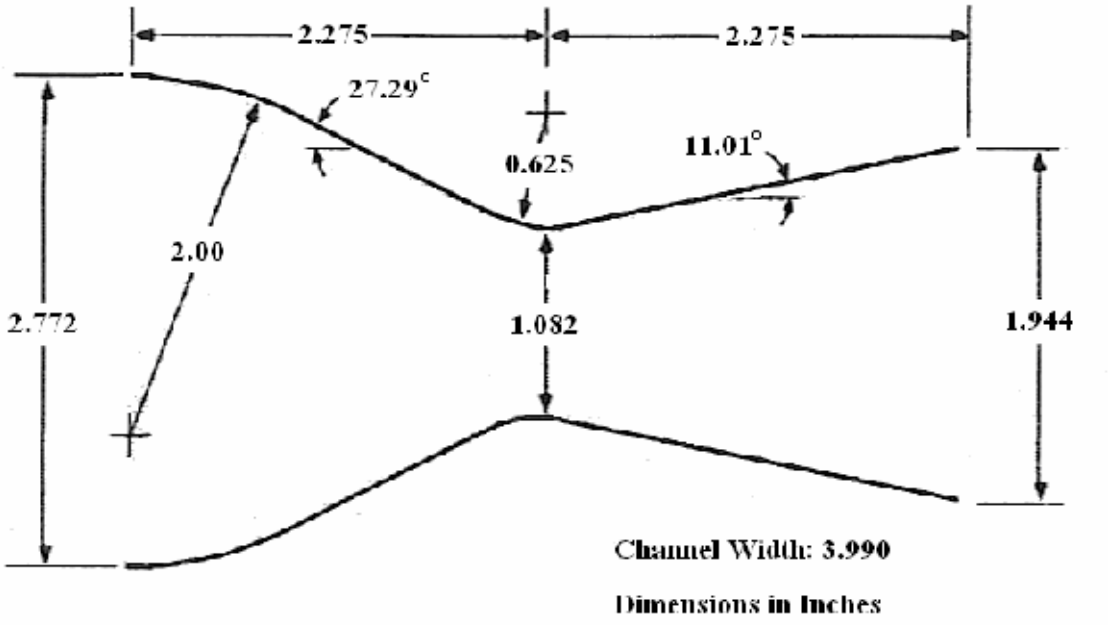

Figure A10 Nozzle geometry [20].

The nozzle performance code was used to obtain computational results for this nozzle geometry. Figure A11 provides a comparison of the computational code results and the experimental results of Hunter [18].

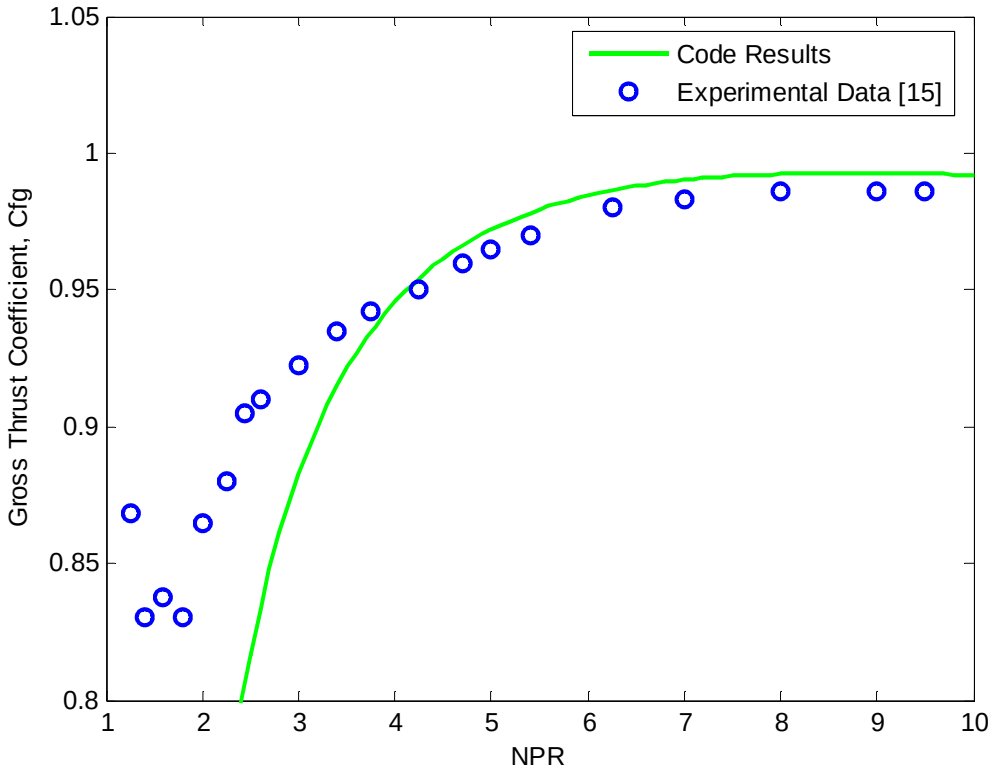

Figure A11 Experimental and computational gross thrust coefficient results for the nozzle of Hunter [18].

As can be seen in Figure A11, the shapes of the computational and experimental curves are identical with the peak of each occurring at a nozzle pressure ratio of 8.78. The code results for nozzle pressure ratios above 3.75 predict the gross thrust coefficient to within 0.8% of the experimental data. At nozzle pressure ratios below 3.75, however, the code underpredicts the experimental results by up to 10%.

In his analysis, Hunter [20] states that the experimental off-design internal pressure data for this nozzle configuration shows strong evidence of shock induced separation in the divergent section of the nozzle for an NPR range of 1.8 to 5.0. As stated

before, this flow separation causes an increase in the thrust efficiency as depicted in Figure A11 over the NPR range of 1.25 to 4. This explains the underprediction of the gross thrust coefficient over this NPR range. Above an NPR of 5, the nozzle was shock free, and thus the code successfully predicts its performance.

4.0 The Experiment of Capone and Berrier [19]

This nozzle geometry was tested by Capone and Berrier [19] as part of a wind tunnel experiment on a 1/10 scale, twin engine F-18 prototype aircraft model. The nozzle geometry is provided in Figure A12. As shown, this nozzle has a throat area of 2.5 in^2, an expansion ratio of 1.15, a divergence angle of 1.54°, and a design NPR of 3.46.

It should be noted that this nozzle geometry consists of a cutback outside sidewall as well as an extended nozzle inter-fairing on the inside sidewall. Thus, in actuality, this nozzle is not two-dimensional along its entire length. The geometry shown in Figure A12 does not depict the sidewall variations.

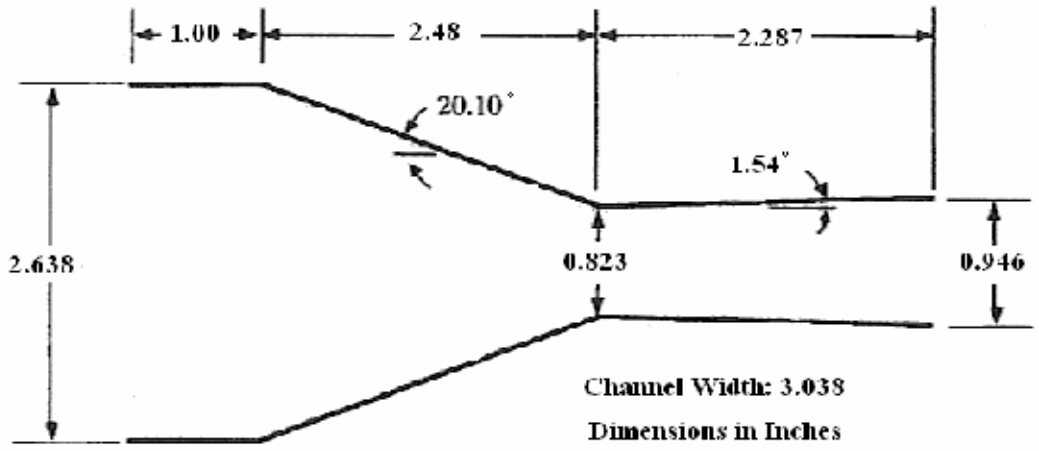

Figure A12 Nozzle geometry [20].

The nozzle performance code was used to obtain computational results for this nozzle geometry. Figure A13 provides a comparison of the computational code results and the experimental results of Capone and Berrier [19].

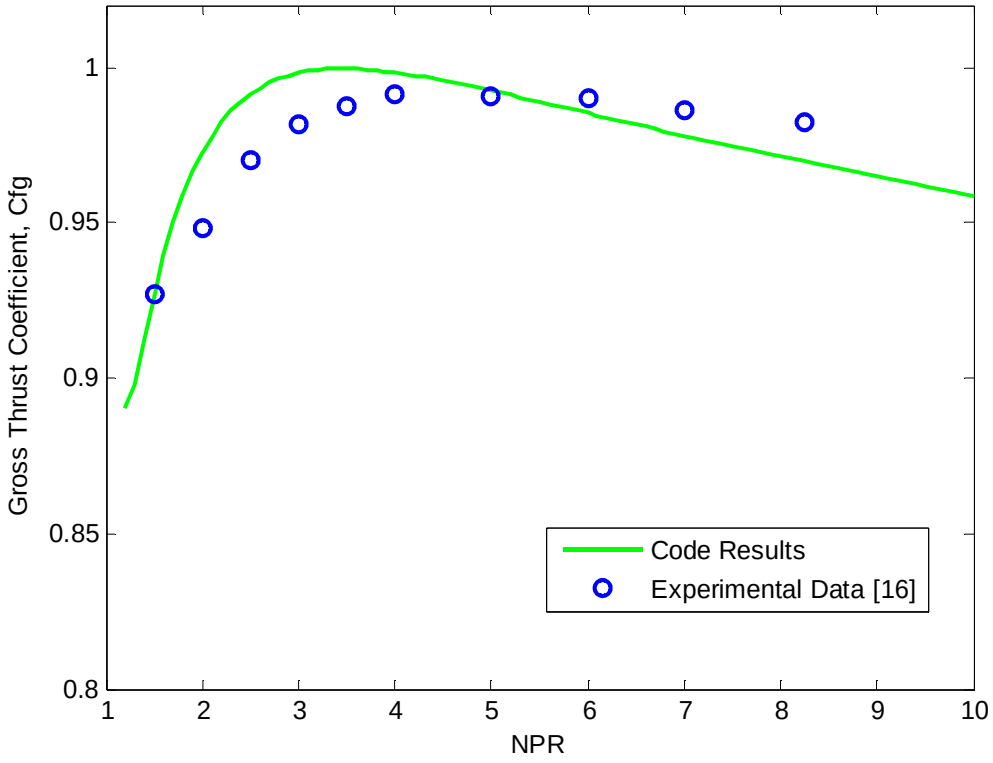

Figure A13 Experimental and computational gross thrust coefficient results for the nozzle of Capone and Berrier [19].

As can be seen in Figure A13, the shapes of the computational and experimental curves are not identical with peak gross thrust coefficients occurring at different nozzle pressure ratios. The computational curve peaks at an NPR of 3.5 while the experimental curve peaks at an NPR of 4. The code results also overpredict the experimental results up to an NPR of 5 and underpredict the experimental results for NPRs above 5. At nozzle

pressure ratios less than 5.0, the difference between the computational and experimental results is at most 2.6%. For nozzle pressure ratios above 5.0, however, the difference is at most as 1.3%.

Some of the discrepancies existing between the computational and experimental results are believed to be linked to the cutback outside sidewall geometry. The outside sidewall cutback increases the effective nozzle expansion ratio thus causing the experimental peak gross thrust performance to occur at a higher NPR.

5.0 Code Adjustments

As mentioned before, this code was designed for the Air Force Research Laboratory Propulsion Directorate for the purpose of modeling the nozzle performance of aircraft engines. As such, it is imperative that the code results match the experimental results as well as possible for lower the NPR regime. One can see in the figures of sections 1.0 - 4.0, that the code continuously overpredicts the nozzle performance.

It was believed that the performance overprediction was due to the omission of the inviscid discharge coefficient from the analysis. In theory, including an inviscid discharge coefficient in the determination of the overall discharge coefficient will lower the performance results over the entire NPR range. As mentioned before, Hall's [6] relation for the inviscid discharge coefficient given in Equation (3.10) was not used because the expression diverges for nozzle radius ratios, $\Omega = \frac{R_t}{R_c}$, greater than unity and many of the nozzles considered in this study have nozzle radius ratios greater than one.

To solve this problem, inviscid discharge coefficient data was generated for nozzle radius ratios of 0.05 to 0.95. The median value of 0.9915 was selected for the

inviscid discharge coefficient and inserted into the nozzle performance code as a constant for any radius ratio value. Following the adjustments made to the nozzle performance code, new computational results were generated for each nozzle considered in this study. The results are provided in Figures A14 –A21.

Figures A14 and A15 provide the computational results, before and after the code adjustments, for nozzles A1 and A2 respectively. One can see that the computational code results with the inviscid discharge coefficient approximation predict the experimental results with error less than 0.3% over the entire NPR range for both nozzles. The lower NPR range computational results offer a much better comparison to the experimental data when the code includes the inviscid discharge coefficient correction.

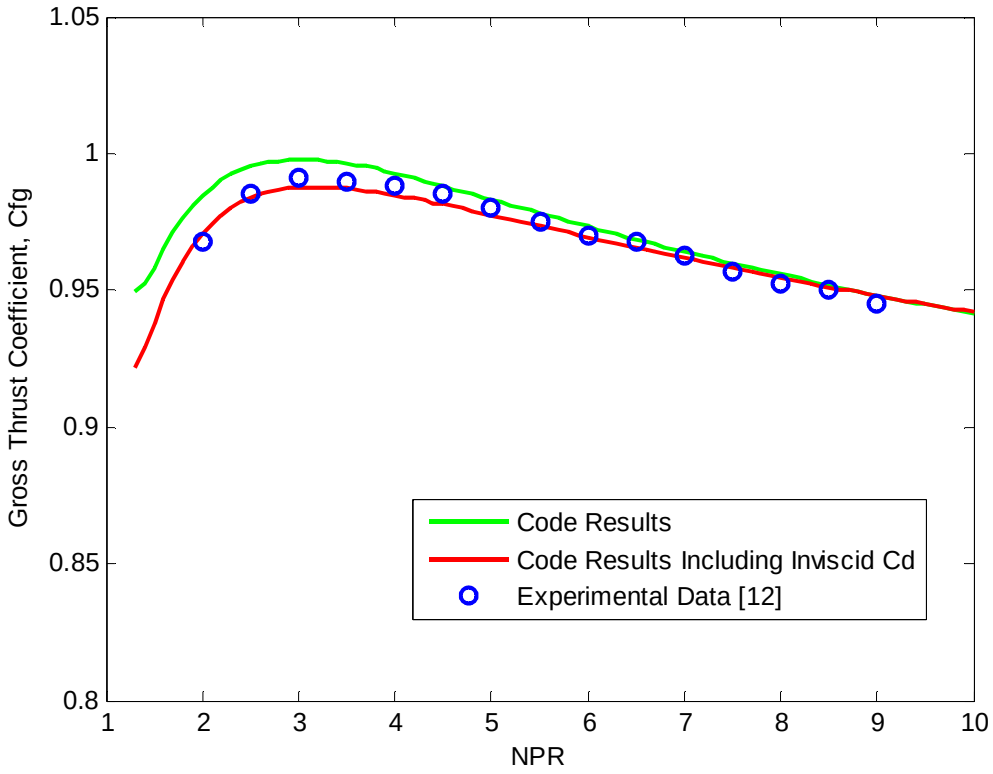

Figure A14 Experimental and adjusted computational gross thrust coefficient results for nozzle configuration A1.

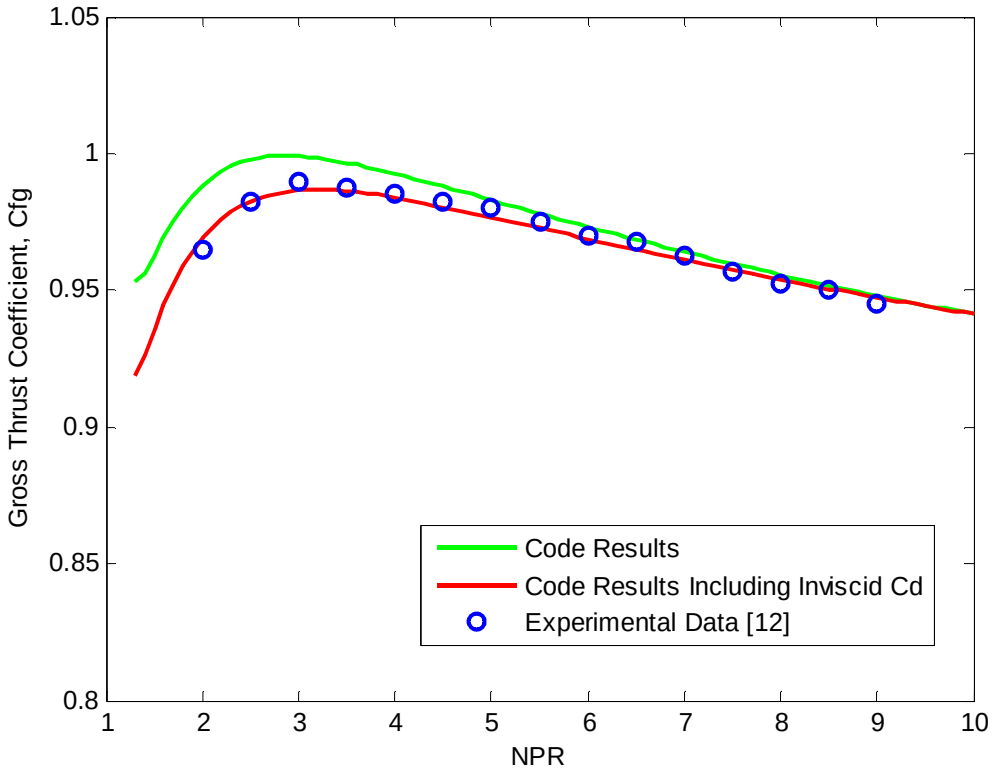

Figure A15 Experimental and adjusted computational gross thrust coefficient results for nozzle configuration A2.

Figures A16, A17 and A18 provide the computational results, before and after the code adjustments, for nozzles B1, B2 and B3 respectively. One can see that the computational code results with the inviscid discharge coefficient approximation predict the experimental results with error less than 0.4% over the higher NPR range for each nozzle. At nozzle pressure ratios below 4.0, however, the code still underpredicts the experimental results by up to 10%. This is due to the separation effects seen in the experimental data at lower nozzle pressure ratios.

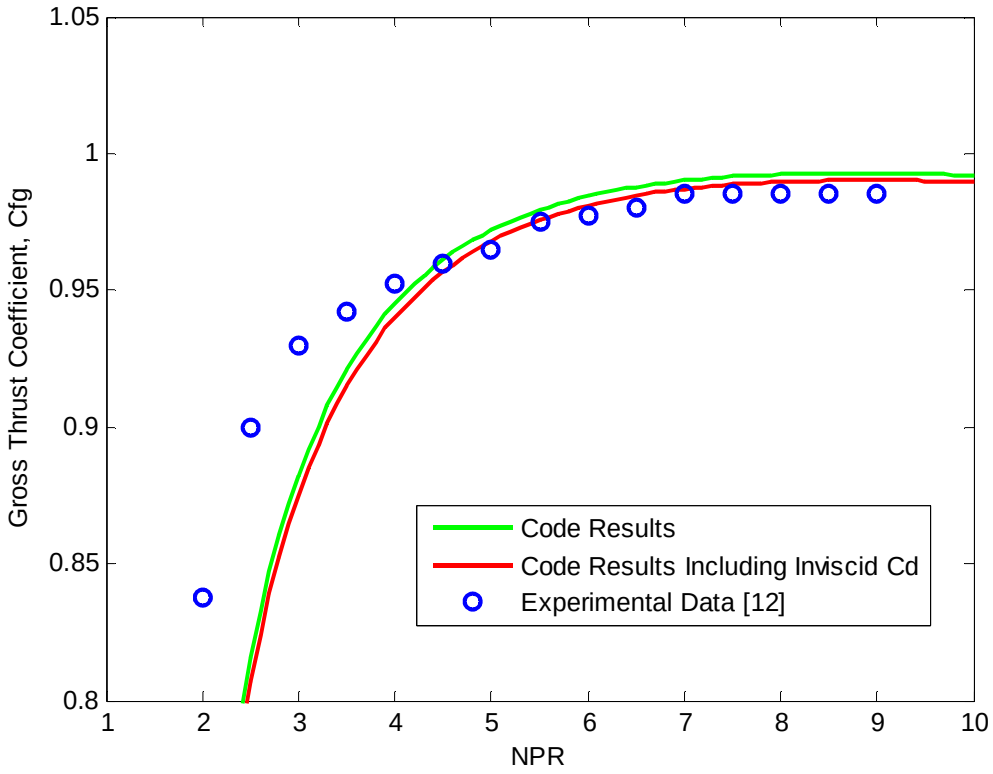

Figure A16 Experimental and adjusted computational gross thrust coefficient results for nozzle configuration B1.

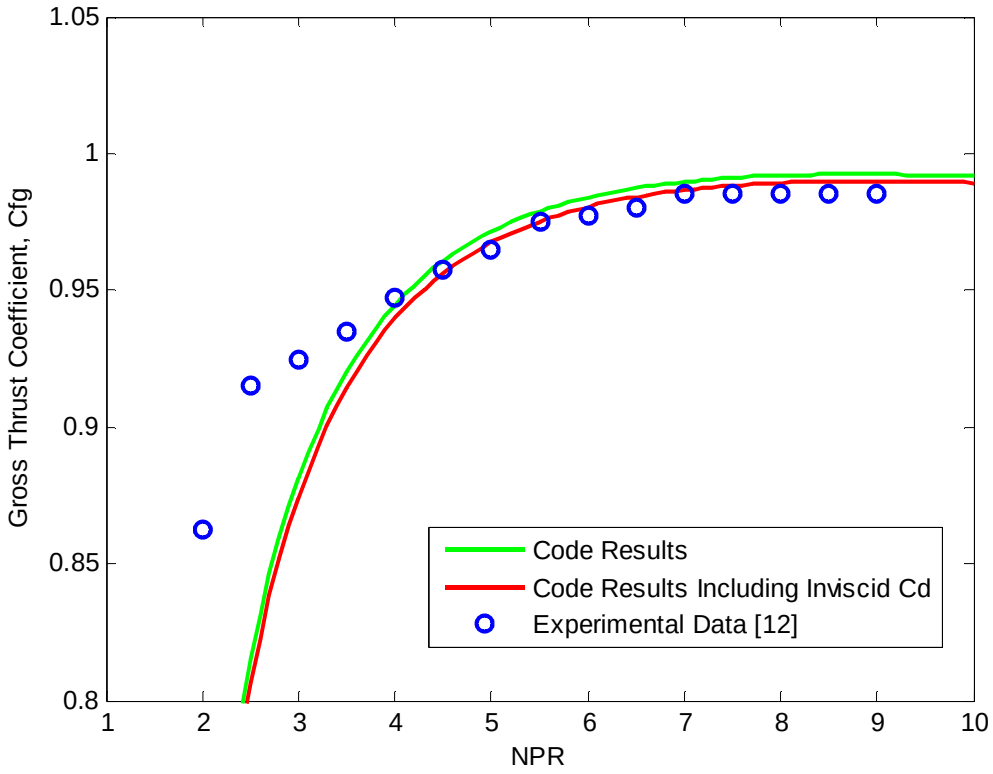

Figure A17 Experimental and adjusted computational gross thrust coefficient results for nozzle configuration B2.

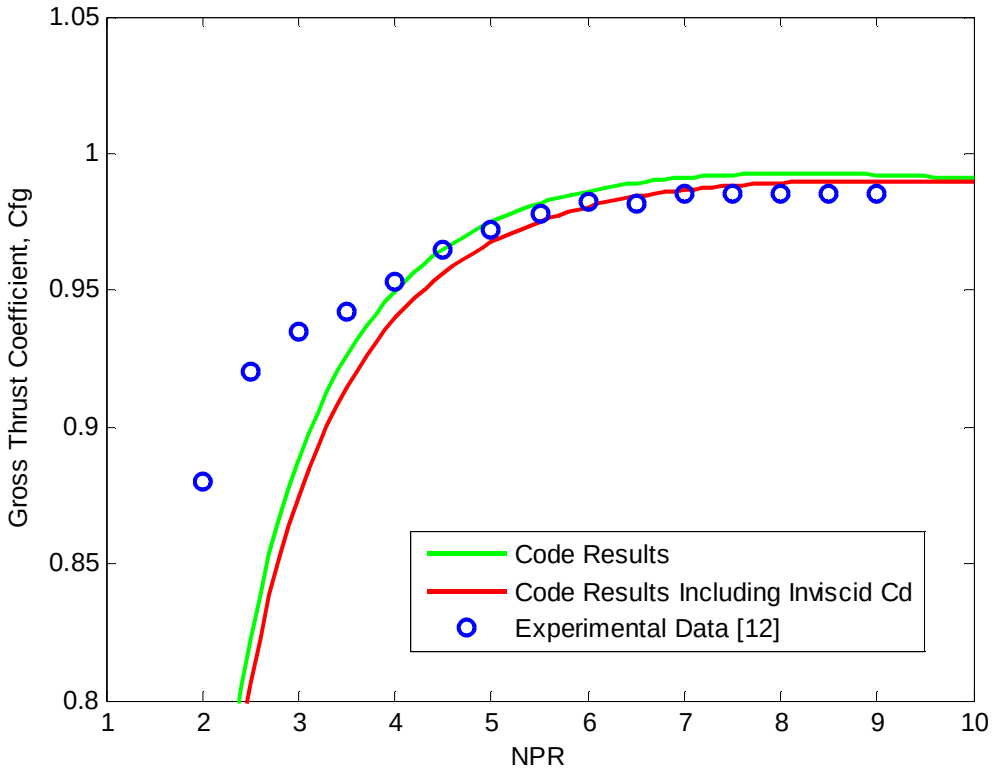

Figure A18 Experimental and adjusted computational gross thrust coefficient results for nozzle configuration B3.

Figure A19 provides the computational results, before and after the code adjustments, for the nozzle geometry of Berrier and Re [17]. One can see that the computational code results with the inviscid discharge coefficient approximation predict the experimental results with error less than 0.4% over the entire NPR range. The lower NPR range computational results offer a much better comparison to the experimental data when the code includes the inviscid discharge coefficient correction.

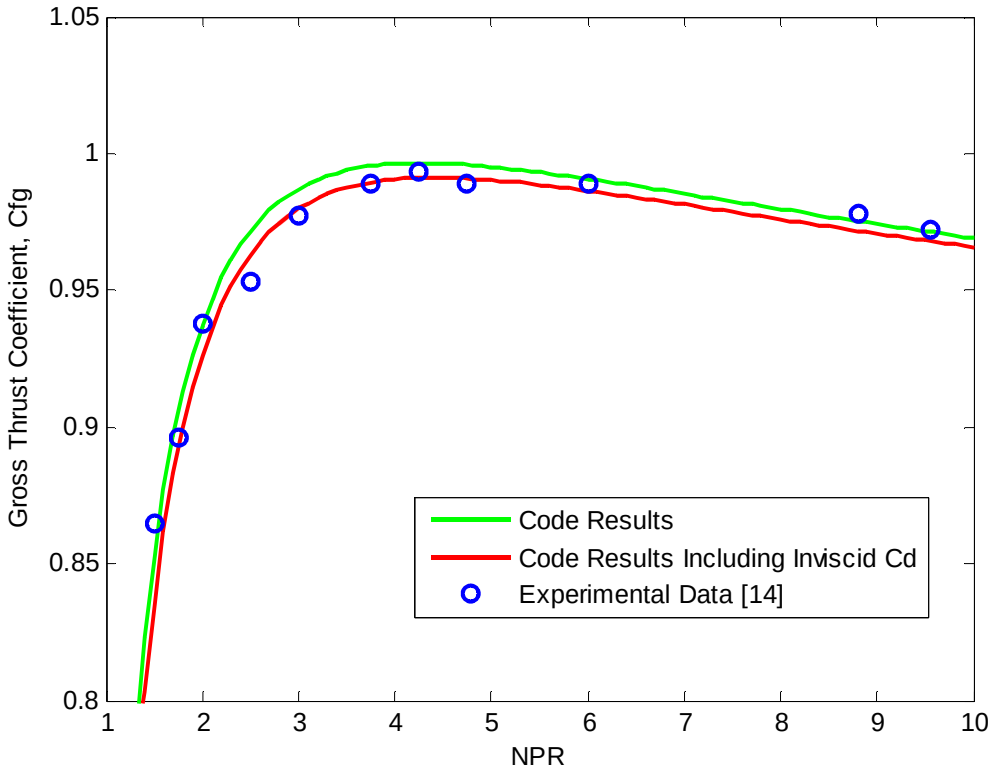

Figure A19 Experimental and adjusted computational gross thrust coefficient results for the nozzle of Berrier and Re [17].

Figure A20 provides the computational results, before and after the code adjustments, for the nozzle geometry of Hunter [18]. One can see that the computational code results with the inviscid discharge coefficient approximation predict the experimental results with error less than 0.4% over the higher NPR range. At nozzle pressure ratios below 4.0, however, the code still underpredicts the experimental results by up to 10%. This is due to the separation effects seen in the experimental data at lower nozzle pressure ratios.

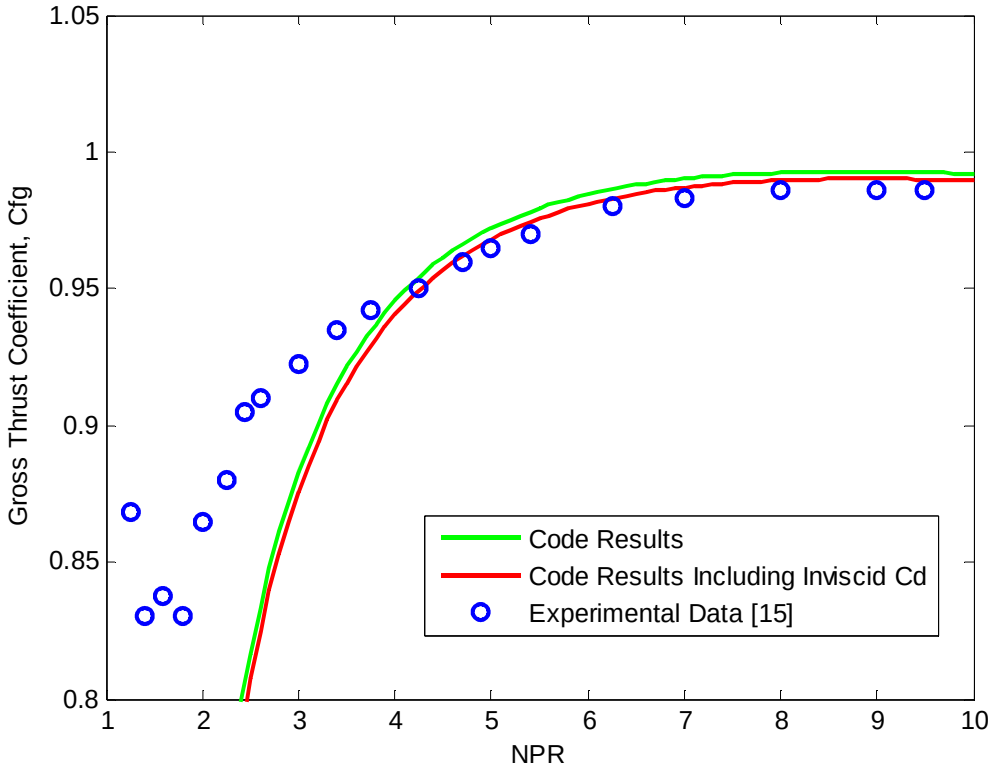

Figure A20 Experimental and adjusted computational gross thrust coefficient results for the nozzle of Hunter [18].

Figure A21 provides the computational results, before and after the code adjustments, for the nozzle geometry of Capone and Berrier [19]. One can see that the computational code results with the inviscid discharge coefficient approximation predict the experimental results with error less than 1.3% for a nozzle pressure ratio range of 1-5. and less than 2% for nozzle pressure ratios above 5.0. The lower NPR range computational results offer a much better comparison to the experimental data when the code includes the inviscid discharge coefficient correction.

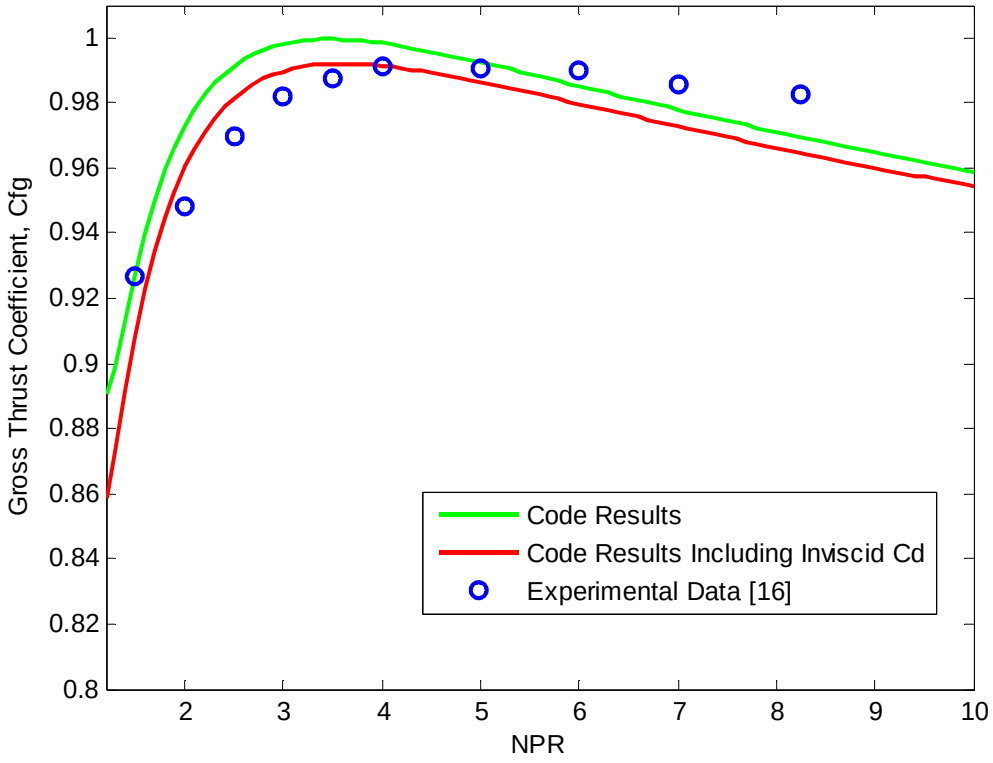

Figure A21 Experimental and adjusted computational gross thrust coefficient results for the nozzle of Capone and Berrier [19].

As one can see in each of the figures of this section, the inclusion of a constant inviscid discharge coefficient improves the computational results for each of the nozzles considered in this analysis. The most important result of this modification is the improvement of the computational results for the lower NPR regime. The performance prediction was improved over the lower NPR range for each case except for those where the experimental data shows signs of separation effects in the nozzle.

It is very important to point out that the assumption of a constant inviscid discharge coefficient of 0.9915 provided improved results for a wide range of nozzle radius ratios. Table A3 provides the radius ratio for each of the nozzle configurations considered in this study. As can be seen in Table A3, the radius ratio varies from values less than one to values much greater than one. Whereas Hall's [6] representation for inviscid discharge coefficient was only valid for radius ratios less than one, the assumption of a constant inviscid discharge coefficient equal to 0.9915 provided valid results for all radius ratios considered.

Table A3 Radius ratio data for each nozzle configuration.

Nozzle Configuration	Radius Ratio R_t/R_c
A1	2.831
A2	0.7026
B1	2.831
B2	0.7026
B3	0.7026
Hunter Case 2	1.2158
Hunter Case 3	1.216
Hunter Case 4	14680

Appendix B: Method of Characteristics Comparison

Gas Dynamics [15] example 15.1 – Uniform radial flow at Mach 2.0 enters a two-dimensional diverging channel with straight walls. Compute the variation of Mach number in this radial flow field, assuming isentropic, steady flow. The walls are inclined at a total angle of 12°.

Table B1 provides the results of the nozzle performance prediction code's MOC subroutine and Table B2 provides the results given in *Gas Dynamics* [15].

Table B1 MOC subroutine output.

Number	Mach Number, M	μ degrees	ν degrees	θ degrees	C1	C2	$\theta+\mu$ degrees	$\theta-\mu$ degrees
1	2.000	30.000	26.380	6	32.380	20.380	36.000	-24.000
2	2.000	30.000	26.380	4	30.380	22.380	34.000	-26.000
3	2.000	30.000	26.380	2	28.380	24.380	32.000	-28.000
4	2.000	30.000	26.380	0	26.380	26.380	30.000	-30.000
5	2.036	29.409	27.380	5	32.380	22.380	34.409	-24.409
6	2.036	29.409	27.380	3	30.380	24.380	32.409	-26.409
7	2.036	29.409	27.380	1	28.380	26.380	30.409	-28.409
8	2.073	28.837	28.380	6	34.380	22.380	34.837	-22.837
9	2.073	28.837	28.380	4	32.380	24.380	32.837	-24.837
10	2.073	28.837	28.380	2	30.380	26.380	30.837	-26.837
11	2.073	28.837	28.380	0	28.380	28.380	28.837	-28.837
12	2.111	28.282	29.380	5	34.380	24.380	33.282	-23.282
13	2.111	28.282	29.380	3	32.380	26.380	31.282	-25.282
14	2.111	28.282	29.380	1	30.380	28.380	29.282	-27.282
15	2.148	27.742	30.380	6	36.380	24.380	33.742	-21.742
16	2.148	27.742	30.380	4	34.380	26.380	31.742	-23.742
17	2.148	27.742	30.380	2	32.380	28.380	29.742	-25.742
18	2.148	27.742	30.380	0	30.380	30.380	27.742	-27.742
19	2.186	27.217	31.380	5	36.380	26.380	32.217	-22.217
20	2.186	27.217	31.380	3	34.380	28.380	30.217	-24.217
21	2.186	27.217	31.380	1	32.380	30.380	28.217	-26.217
22	2.225	26.707	32.380	6	38.380	26.380	32.707	-20.707
23	2.225	26.707	32.380	4	36.380	28.380	30.707	-22.707
24	2.225	26.707	32.380	2	34.380	30.380	28.707	-24.707
25	2.225	26.707	32.380	0	32.380	32.380	26.707	-26.707
26	2.264	26.210	33.380	5	38.380	28.380	31.210	-21.210
27	2.264	26.210	33.380	3	36.380	30.380	29.210	-23.210
28	2.264	26.210	33.380	1	34.380	32.380	27.210	-25.210
29	2.304	25.725	34.380	6	40.380	28.380	31.725	-19.725
30	2.304	25.725	34.380	4	38.380	30.380	29.725	-21.725
31	2.304	25.725	34.380	2	36.380	32.380	27.725	-23.725
32	2.304	25.725	34.380	0	34.380	34.380	25.725	-25.725

Table B2 *Gas Dynamics* MOC textbook results [15].

Number	Mach Number, M	μ degrees	ν degrees	θ degrees	C1	C2	θ+μ degrees	θ-μ degrees
1	2.000	30.000	26.380	6	32.380	20.380	36.000	-24.000
2	2.000	30.000	26.380	4	30.380	22.380	34.000	-26.000
3	2.000	30.000	26.380	2	28.380	24.380	32.000	-28.000
4	2.000	30.000	26.380	0	26.380	26.380	30.000	-30.000
5	2.040	29.350	27.380	5	32.380	22.380	34.350	-24.350
6	2.040	29.350	27.380	3	30.380	24.380	32.350	-26.350
7	2.040	29.350	27.380	1	28.380	26.380	30.350	-28.350
8	2.070	28.890	28.380	6	34.380	22.380	34.890	-22.890
9	2.070	28.890	28.380	4	32.380	24.380	32.890	-24.890
10	2.070	28.890	28.380	2	30.380	26.380	30.890	-26.890
11	2.070	28.890	28.380	0	28.380	28.380	28.890	-28.890
12	2.110	28.290	29.380	5	34.380	24.380	33.290	-23.290
13	2.110	28.290	29.380	3	32.380	26.380	31.290	-25.290
14	2.110	28.290	29.380	1	30.380	28.380	29.290	-27.290
15	2.150	27.720	30.380	6	36.380	24.380	33.720	-21.720
16	2.150	27.720	30.380	4	34.380	26.380	31.720	-23.720
17	2.150	27.720	30.380	2	32.380	28.380	29.720	-25.720
18	2.150	27.720	30.380	0	30.380	30.380	27.720	-27.720
19	2.190	27.170	31.380	5	36.380	26.380	32.170	-22.170
20	2.190	27.170	31.380	3	34.380	28.380	30.170	-24.170
21	2.190	27.170	31.380	1	32.380	30.380	28.170	-26.170
22	2.230	26.640	32.380	6	38.380	26.380	32.640	-20.640
23	2.230	26.640	32.380	4	36.380	28.380	30.640	-22.640
24	2.230	26.640	32.380	2	34.380	30.380	28.640	-24.640
25	2.230	26.640	32.380	0	32.380	32.380	26.640	-26.640
26	2.260	26.260	33.380	5	38.380	28.380	31.260	-21.260
27	2.260	26.260	33.380	3	36.380	30.380	29.260	-23.260
28	2.260	26.260	33.380	1	34.380	32.380	27.260	-25.260
29	2.300	25.770	34.380	6	40.380	28.380	31.770	-19.770
30	2.300	25.770	34.380	4	38.380	30.380	29.770	-21.770
31	2.300	25.770	34.380	2	36.380	32.380	27.770	-23.770
32	2.300	25.770	34.380	0	34.380	24.380	25.770	-25.770

One can see, from a comparison of Table B1 with Table B2 that the method of characteristics subroutine results compare extremely well with those results provided in *Gas Dynamics* [15].

Appendix C: Program User's Guide

An analytical prediction code has been developed to determine the thrust performance of non-axisymmetric two-dimensional converging diverging nozzles. The program calculates nozzle losses due to viscous effects, expansion, and angularity based on a number of user defined parameters.

1. User Inputs

To begin, the user is given the option of defining the nozzle by (1) its lengths - primary nozzle length and secondary nozzle length - secondary nozzle half angle, and radius of curvature or (2) defining the nozzle contour for various streamwise locations[13]. The second option is chosen if the nozzle can not be defined by a constant secondary nozzle half angle because of angle variance due to the contour of the secondary nozzle.

1.1 Nozzle Geometry

This program was designed to analyze nozzles characterized by either sharp cornered or smooth contoured throats. Figure C1 depicts the nozzle geometry for which this analysis is valid. In this illustration, station 7 represents the nozzle entrance, station 8 the nozzle throat, and station 9 the nozzle exit. Important geometrical inputs are the nozzle throat and exit areas, primary and secondary nozzle lengths, radius of curvature, and secondary nozzle half angle or nozzle contour (for angle variance).

[13] This routine works best when the user inputs points that are equally spaced, along the streamwise direction, from the nozzle entrance to the nozzle exit. The user must enter at least 11 points, but may enter more if he/she chooses.

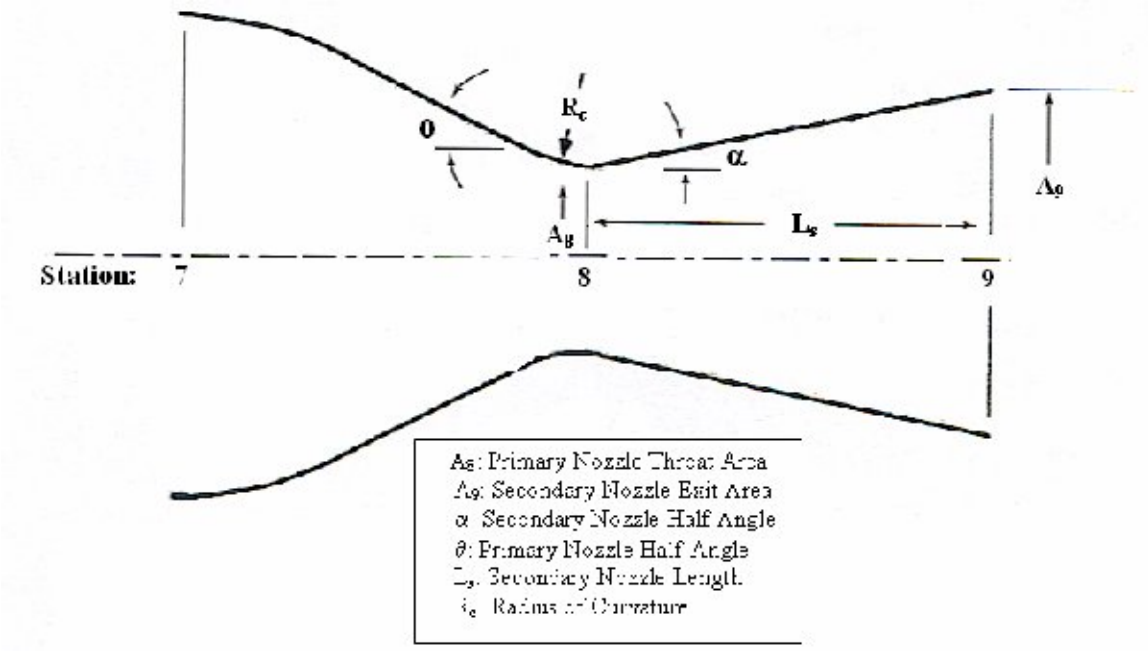

Figure C1 Non-axisymmetric two-dimensional converging diverging nozzle geometry

Nozzle Cross Section

As stated before, this program is used to analyze the gross thrust performance of non-axisymmetric two-dimensional converging diverging nozzles. As such, the user has the option of defining a nozzle of rectangular or square cross section. If the rectangular option is selected, the user must define the length of the rectangular cross section.

Radius of Curvature

If the user chooses nozzle geometry definition (1), they have the option of defining the radius of curvature, if it is known. If the user chooses to analyze a nozzle with a sharp cornered throat, the radius of curvature is simply defined to be virtually zero (~0.00001). If the user does not know the radius of curvature, they can use a subprogram

that will determine the radius of curvature for them. To use this routine, the user must enter the nozzle contour at various streamwise locations[14]. The program fits a polynomial, $y = f(x)$, to these points and calculates the curvature using Equation (1).

$$\kappa(x) = \frac{\left|f''(x)\right|}{\left[1 + (f'(x))^2\right]^{3/2}} \tag{1}$$

where κ is the curvature, f'(x) is the first derivative of the polynomial, f''(x) is the second derivative of the polynomial, and x is the streamwise location of the nozzle throat. The radius of curvature is then determined using the Equation (2).

$$R_c = \frac{1}{|\kappa|} \tag{2}$$

where R_c is the radius of curvature and κ is the curvature.

If the user chooses nozzle geometry definition (2), the program will automatically calculate the radius of curvature using the same method as the radius of curvature subroutine for nozzle geometry definition (1).

1.2 Gas Properties

After the nozzle geometry has been defined, the program user is asked to describe the gas at various locations throughout the nozzle. Specifically, the user is asked for the molecular weight of the gas as well as the atmospheric temperature and pressure. A file has been set up entitled gas_description_Kelvin.m or gas_description_Rankine.m depending on the type of units being used. This file includes a temperature range, corresponding specific heat ratios (gammas), and corresponding dynamic viscosities for

[14] This routine works best when the user inputs points that are equally spaced, along the streamwise direction, from the nozzle entrance to the nozzle exit. The user must enter at least 11 points, but may enter more if he/she chooses.

the gas in question. The current file is set up for air. The user can modify this file if the gas in question is not air.

1.3 Number of Nodes for MOC

Here the user enters the number of equally spaced nodes to be used for the method of characteristics. Numbers from 2 and up can be chosen, but as the number gets larger than 20, the computation time increases drastically. I have typically used a 10 node analysis.

1.4 Throat Mach Number

The user is also prompted to enter the Mach number at the nozzle throat. If the Mach number at the throat is unity, it should be entered as 1.01. This is because the program uses the method of characteristics, which is based on supersonic flow, to determine the exit angle variance.

References

[1] Hill, Philip, and Peterson, Carl, *Mechanics and Thermodynamics of Propulsion.* Addison-Wesley Publishing Company, Inc., 1992.

[2] Oates, Gordon C., "Variable Convergent-Divergent Exhaust Nozzle Aerodynamics", *The Aerodynamics of Aircraft Gas Turbine Engines.* Chapter14.

[3] Mattingly, Jack D., Heiser, William H., and Pratt, David T., *Aircraft Engine Design.* American Institute of Aeronautics and Astronautics Inc., 2002.

[4] Stratford, B.S., "The Calculation of the Discharge Coefficient of Profiled Choked Nozzles and the Optimum Profile for Absolute Air Flow Measurement". *Journal of the Royal Aeronautical Society,* Volume 68, Number 640, April 1964.

[5] Masure, B., "Study of the Precision of Measurement of Gas Flow Rates by the Sonic Nozzle Method". *National Aeronautics and Space Administration N69-29669*, June 1969.

[6] Hall, I.M., "Transonic Flow in Two-Dimensional and Axially Symmetric Nozzles". *Quarterly Journal of Mechanics and Applied Mathematics*, Volume XV, Part 4, pages 487-508, 1962.

[7] Tang, S.P., and Fenn, J.B., "Experimental Determination of the Discharge Coefficients for Critical Flow through an Axisymmetric Nozzle". *AIAA Journal*, Volume 16, Number 1, January 1978.

[8] Geropp, D., "Laminare Grenzschichten In Ebenen Und Rotationssymmetrischen Lavalduesen". *Deutsche Luft-Und Raumfart, Forschungsbericht*, pages 71-90, 1971.

[9] Johnson, Aaron N., "Numerical Characterization of the Discharge Coefficient in Critical Nozzles". *PhD Dissertation.* The Pennsylvania State University, 2000.

[10] Kuluva, N.M., and Hosack, G.A., "Supersonic Nozzle Discharge Coefficients at Low Reynolds Numbers". *AIAA Journal*, Volume 9, 1971, pages 1876-1879.

[11] Jones, O.C., "An Improvement in the Calculation of Turbulent Friction in Rectangular Ducts". *Journal of Fluids Engineering*, Volume 98, 1976, pages 173-181.

[12] Jones, O.C., and Leung, J.C.M., "An Improvement in the Calculation of Turbulent Friction in Smooth Concentric Annuli". *Journal of Fluids Engineering*, Volume 103, 1981, pages 615-623.

[13] White, Frank M., *Viscous Fluid Flow.* McGraw-Hill Inc., 1991.

[14] Berker, A.R., "Integration des Equations du Movement d'un Fluide Visqueux Incompressible", *Encyclopedia of Physics*, Volume 8, Part 2, pages 1-384. Springer, Berlin.

[15] John, James E.A., *Gas Dynamics.* Allyn and Bacon Inc., 1984.

[16] Mason, Mary L., Putnam, Lawrence E., and Re, Richard J., "The Effect of Throat Contouring on Two-Dimensional Converging-Diverging Nozzles at Static Conditions". *NASA Technical Paper 1704*, August 1980.

[17] Berrier, B.L., and Re, R.J., "Effects of Several Geometric Parameters on the Static Internal Performance of Three Nonaxisymmetric Nozzle Concepts". *NASA Technical Paper 1468*, July 1979.

[18] Hunter, C.A., "An Experimental Analysis of Passive Shock – Boundary Layer Interaction Control for Improving the Off-Design Performance of Jet Exhaust Nozzles". *M.S. Thesis*, George Washington University, September 1993.

[19] Capone, F.J., and Berrier, B.L., "Investigation of Axisymmetric and Nonaxisymmetric Nozzles Installed on a 0.10 – Scale F-18 Prototype Airplane Model". *NASA Technical Paper 1638*, June 1980.

[20] Hunter, Craig A., "An Approximate Computational Method for Modeling the Static Thrust Performance of Non-Axisymmetric Two-Dimensional Convergent-Divergent Nozzles". *NASA Contractor Report 195050,* March 1995.

[21] Cline, Michael C., "A Computer Program for the Computation of Two-Dimensional, Time-Dependent, Inviscid Nozzle Flow". *LA-5984 (Contract W-7405-ENG)*, Los Alamos Science Laboratory, University of California, January 1977.

Vita

Angela M. Geatz graduated from Bishop Walsh Catholic High School in Cumberland, Maryland. She entered undergraduate studies at West Virginia University in Morgantown, West Virginia where she received dual Bachelor of Science degrees in Mechanical and Aerospace Engineering in August 2002. In October 2003, she entered the Graduate School of Engineering and Management at the Air Force Institute of Technology to pursue a Master of Science degree in Aeronautical Engineering. Upon graduation, she will begin employment with Lockheed Martin in Dallas, Texas as a Systems Engineer for their Missiles and Fire Control Branch.

REPORT DOCUMENTATION PAGE

Form Approved
OMB No. 074-0188

The public reporting burden for this collection of information is estimated to average 1 hour per response, including the time for reviewing instructions, searching existing data sources, gathering and maintaining the data needed, and completing and reviewing the collection of information. Send comments regarding this burden estimate or any other aspect of the collection of information, including suggestions for reducing this burden to Department of Defense, Washington Headquarters Services, Directorate for Information Operations and Reports (0704-0188), 1215 Jefferson Davis Highway, Suite 1204, Arlington, VA 22202-4302. Respondents should be aware that notwithstanding any other provision of law, no person shall be subject to an penalty for failing to comply with a collection of information if it does not display a currently valid OMB control number.
PLEASE DO NOT RETURN YOUR FORM TO THE ABOVE ADDRESS.

1. REPORT DATE *(DD-MM-YYYY)*	**2. REPORT TYPE**	**3. DATES COVERED** *(From – To)*
12-22-2005	**Master's Thesis**	Jun 2004 – Dec 2005

4. TITLE AND SUBTITLE

A Prediction Code for the Thrust Performance of Two-Dimensional, Non-Axisymmetric, Converging-Diverging Nozzles

5a. CONTRACT NUMBER

5b. GRANT NUMBER

5c. PROGRAM ELEMENT NUMBER

6. AUTHOR(S)

Geatz, Angela M.

5d. PROJECT NUMBER

5e. TASK NUMBER

5f. WORK UNIT NUMBER

7. PERFORMING ORGANIZATION NAMES(S) AND ADDRESS(S)

Air Force Institute of Technology
Graduate School of Engineering and Management (AFIT/EN)
2950 Hobson Way
WPAFB OH 45433-7765

8. PERFORMING ORGANIZATION REPORT NUMBER

AFIT/GAE/ENY/06-03

9. SPONSORING/MONITORING AGENCY NAME(S) AND ADDRESS(ES)

AFRL/PRTA
Attn: Mr. Alex Giese
1950 Fifth Street
WPAFB OH 45433-7765

10. SPONSOR/MONITOR'S ACRONYM(S)

11. SPONSOR/MONITOR'S REPORT NUMBER(S)

12. DISTRIBUTION/AVAILABILITY STATEMENT

APPROVED FOR PUBLIC RELEASE; DISTRIBUTION UNLIMITED.

13. SUPPLEMENTARY NOTES

14. ABSTRACT

The objective of this research is to develop a prediction code for the Air Force Research Laboratory Propulsion Directorate that can accurately determine the gross thrust coefficient for a user defined non-axisymmetric two-dimensional converging diverging nozzle. The code includes the effects of friction, angularity, and expansion losses on nozzle efficiency. To demonstrate the prediction method, the generated computational results were compared to experimental data, as well as computational results from other existing nozzle performance codes, for a number of different nozzle geometries. The nozzle internal performance prediction code showed excellent agreement with experimental data in predicting the gross thrust performance for all nozzle geometries considered. It was shown, however, that when the experimental data showed evidence of flow separation, a flow phenomenon this code is unable to predict, the code results underpredicted the experimental by up to 10%.

15. SUBJECT TERMS

Gross Thrust Coefficient, Converging- Diverging Nozzles, Nozzle Performance, Nozzle Efficiency

16. SECURITY CLASSIFICATION OF:			**17. LIMITATION OF ABSTRACT**	**18. NUMBER OF PAGES**	**19a. NAME OF RESPONSIBLE PERSON**
REPORT	**ABSTRACT**	**c. THIS PAGE**			Dr. Paul King
U	**U**	**U**	**UU**	119	**19b. TELEPHONE NUMBER** *(Include area code)* (937) 255-3636, ext 4628; e-mail: Paul.King@afit.edu

Standard Form 298 (Rev: 8-98)
Prescribed by ANSI Std. Z39-18